This is to certify that the

dissertation entitled

EFFECTS OF 2-D AND 3-D FORCING ON
MOLECULAR MIXING IN A TWO-STREAM
SHEAR LAYER

presented by

Colin G. MacKinnon

has been accepted towards fulfillment
of the requirements for

PhD degree in Mechanical Engineering

M. M. Koochesfahani
Major professor

Date 12/15/1998

EFFECTS OF 2-D AND 3-D FORCING ON MOLECULAR MIXING IN A TWO-STREAM SHEAR LAYER

By

Colin G. M^{ac}Kinnon

A DISSERTATION

Submitted to
Michigan State University
in partial fulfillment of the requirements
for the degree of

DOCTOR OF PHILOSOPHY

Department of Mechanical Engineering

1998

ABSTRACT

EFFECTS OF 2-D AND 3-D FORCING ON MOLECULAR MIXING IN A TWO-STREAM SHEAR LAYER

By

Colin G. M^{ac}Kinnon

It is well known that external 2-D perturbations at frequencies low compared to the natural roll-up frequency lead to enhanced growth rates in a two-stream shear layer. The purpose of the present study was to quantify various aspects of the molecular mixing taking place in such flows. Experimental measurements were obtained for the amount of molecular mixing and the mixture composition in a chemically reacting turbulent shear layer subjected to 2-D perturbations, over a range of frequencies and amplitudes. In addition, the effect of 3-D forcing and combined 2-D/3-D forcing on the mixing field were studied. The results show that the fraction of the shear layer width filled with mixed fluid initially decreases and then increases with forcing frequency. Somewhat surprisingly, even though the addition of 3-D perturbations did cause spanwise undulations in the mixed fluid amount, the layer width and the average mixed-fluid concentration, it did not change the trend in the mixed-fluid fraction found for purely 2-D forcing. This indicates that streamwise vorticity injection does not necessarily lead to further increases of the mixing enhancement in this study in a liquid phase, high Schmidt number shear layer.

In a work independent from the above, the need for both mixing and kinematic data has led to the development of a technique to simultaneously measure velocity and concentration in a mixing layer. Although the technique is still in an evolutionary stage, the potential of this approach is demonstrated.

This thesis is dedicated to my parents Norman and Margaret M^{ac}Kinnon.

ACKNOWLEDGEMENTS

Thanks are due to many people for the completion of this thesis. I am indebted to my advisor, Dr. Manooch Koochesfahani, for advice and guidance over the last few years. I am grateful to the other 'inmates' - past and present - for helpful discussions and assistance! In particular Mr. Richard Cohn has served above the call of duty with unceasing patience to all my questions. Finally, a warm thank-you to all my friends and family everywhere for your tremendous support.

TABLE OF CONTENTS

Chapter 4

Chapter 5

LIST OF FIGURES

LIST OF SYMBOLS

Symbol	Description
C_d	dye concentration
C_{d_0}	low-speed free-stream dye concentration
C_p	product concentration
$(C_p)_{max}$	product concentration at fluorescence turn-on threshold
$\overline{C_p}$	average product concentration
D	peg diameter
E	entrainment ratio
f	forcing frequency
f_o	initial roll-up frequency
H	peg height
I	pixel intensity
I_f	fluorescence intensity
$(I_f)_{max}$	intensity at fluorescence turn on threshold
I_{fo}	intensity corresponding to free stream dye concentration
M	molar concentration
n	number of absorbing dye molecules at time t
n_0	number of absorbing dye molecules at time t=0
n_A	number of moles in acid

r	velocity ratio, U_2/U_1
λ	growth rate parameter, $(U_1 - U_2)/(U_1 + U_2)$
Re_{δ_1}	Reynolds number, $\Delta U\ \delta_1/\nu$
Re_θ	Reynolds number based on momentum thickness at splitter plate tip, $U\theta_o/\nu$
t	time
Δt	time delay
T	total length of time record
U_1	high-speed free-stream velocity
U_2	low-speed free-stream velocity
U_c	convection speed of large structures
$\bar{u}(y)$	mean streamwise velocity at y
υ_1	volume of low-speed fluid
υ_2	volume of high-speed fluid
υ_A	acid volume
υ_B	base volume
$\upsilon_{1,2}$	volume of high-speed, low-speed fluid
x	streamwise coordinate
x^*	dimension-less variable, $\lambda x f / U_c$
y	transverse coordinate
z	spanwise coordinate
α	dye absorption coefficient
γ	consecutive rows below free stream intensity for image filtering

δ_1	shear layer 1% thickness
$\overline{\delta_1}$	span-averaged layer 1% thickness
δ_m	mixed-fluid thickness
$\overline{\delta_m}$	span-averaged mixed-fluid thickness
$\delta_{P1,P2}$	product thicknesses
δ_ω	vorticity thickness
δ_{vis}	shear layer visual thickness
ϵ	small number
ε_0	dye molar absorption coefficient
θ	layer momentum thickness
θ_o	initial layer momentum thickness
λ_D	smallest scalar diffusion scale
λ_K	Kolmogorov scale
ν	kinematic viscosity
ξ	high-speed fluid volume fraction
ξ_B	base volume fraction
ξ_S	concentration at fluorescence turn on threshold
τ_b	dye bleaching time constant
ω	vorticity
pdf	probability density function
LIF	laser induced fluorescence

Chapter 1

INTRODUCTION

The present work is concerned with mixing in a nominally planar, incompressible shear layer. This type of flow arises when two fluids of different speeds, which are initially separated by a thin partition (for example, a splitter plate), merge with each other. A schematic of the flow configuration is shown in Figure 1.1.1. If the Reynolds number is sufficiently high, intense mixing occurs in the region of the velocity gradient between the streams. For this reason such shear layers are often called mixing layers. The dramatic increase in the amount of mixing as the Reynolds number is increased was called the 'mixing transition' by Konrad (1976). This will be discussed in more detail later in the introduction.

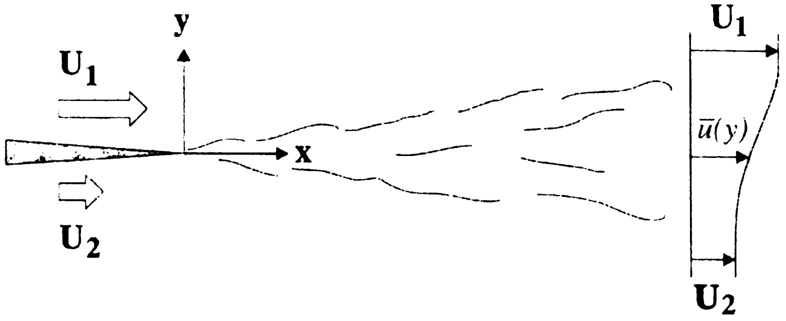

Figure 1.1.1. Geometry of a shear layer.

Over the past few decades turbulent mixing layers have been the subject of a great deal of attention. This is not only because of their occurrence in countless numbers of naturally-occurring and engineering flows, but also due to their fundamental importance in the study of free shear flows. In practical applications, shear layers govern the rate of mixing in combustion chambers, and are also responsible for some of the broadband noise generated in propulsion systems. The ability to control the mixing, structure and growth of the shear layer would have a significant impact on many engineering applications. The purpose of the current work is to investigate the ways in which the molecular mixing field is affected by two-dimensional and three-dimensional external perturbations.

1.1 Background

There have been many significant experimental and computational works related to the present study in recent years. These studies fall into three main categories which will be discussed in the following sections.

1.1.1 The Natural Layer

A shear layer which is not subjected to any externally imposed disturbances is often referred to as a natural shear layer. Probably the most important recent discovery concerning natural shear layers was made by Brown & Roshko (1971, 1974). They initially wanted to study the effect of a density difference in their gaseous layer. While they did find that large changes of the density ratio across the mixing layer had a relatively small effect on the layer spreading angle, they were astonished to find that the flow was dominated by large coherent structures over a wide range of Reynolds numbers. Their shadowgraph pictures also showed that a fine mesh of small scale three-dimensional motions was superposed on the background of the large structures.

At about the same time, Winant & Browand (1974) proposed that the primary mechanism by which the shear layer grows is by the amalgamation of two neighboring structures into a single larger structure. They called this interaction 'pairing'. In the natural layer the vortices are irregularly spaced so that when pairings (and other amalgamations) take place, the growth of the layer increases, on the average, in a linear fashion. Hernan & Jimenez (1982) have suggested that the pairing process is not the only mode of growth of the shear layer. Their results indicated that most of the entrainment is achieved during the normal life of the large spanwise structures, but not during pairing. However, there seems to be little doubt that most of the entrainment of irrotational fluid into the layer is associated with the evolution of the large scale structures.

The work of Dimotakis & Brown (1976) showed that the large scale motions persisted, in a liquid mixing layer, up to Reynolds numbers of 3 x 10^6 (based on the velocity of the high-speed stream and the distance from the trailing edge of the splitter plate to the measurement location). They also pointed out that the dynamics of the shear layer may in fact be governed by a global 'feedback mechanism'. This mechanism suggests that the initiation of the layer at the splitter plate tip is coupled with the large scale structures located farther downstream.

The formation and persistence of the organized two-dimensional structures has been documented in numerous other investigations (for example, Rebollo, 1973; Browand & Weidman, 1976; Wygnanski et al., 1979; Browand & Ho, 1983). There is, however, a secondary structure present in the flow. Miksad (1972) was among the first to observe weak longitudinal vortical structures in his low Reynolds number gaseous layer, and concluded that 'once a secondary vortex structure is established transition to turbulence occurs'. In the works of Konrad (1976) and Breidenthal (1978, 1981), plan views of their shear layers revealed streamwise streaks. Breidenthal interpreted these to be pairs of streamwise vortices of alternating signs. This was confirmed by the cross-sectional views of Bernal (1981). His pictures showed structures composed of pairs of counter-rotating streamwise vortices superimposed on the spanwise vortices. A more recent study by Huang & Ho (1990) has led to the conclusion that the interactions between the merging spanwise structures and the streamwise vortices leads to the generation of small scale three-dimensional motions. The production of small scale motion is regarded to be the mechanism which increases mixing in the layer, by means of increased interfacial area (Jimenez, Martinez-Val & Rebollo, 1979).

Thus, a simplified view of the development of the flow in a turbulent shear layer is given by the following. It is well known that for a shear layer with laminar boundary layers on the splitter plate, disturbances are amplified immediately downstream of the plate by Kelvin-Helmholtz instability. These disturbances grow from the plate tip with a certain natural frequency which is dependent on the velocity ratio and the initial momentum thickness, θ_o, of the layer. These instability waves initially grow exponentially, until they saturate and large spanwise structures develop. Through the interaction of these structures with the streamwise vortices, small-scale motions are produced, which subsequently lead to enhanced mixing within the layer. Prior to the establishment of fully rolled-up vortices certain aspects of the flow can satisfactorily be described by linear inviscid stability theory (Michalke, 1965). The ensuing interactions of the primary and secondary vortices resulting in the fine scale three-dimensional motions need further investigation to enable a more detailed understanding.

1.1.2 Molecular Mixing

The vast majority of research in shear layers, and shear flows in general, has concentrated on the momentum transport properties of the flow. Quantities typically measured include mean and rms velocities, frequency spectra of the velocity fluctuations, Reynolds stresses and, more recently, vorticity (Lang, 1985; Foss & Haw, 1990; Foss & Wallace, 1989; Balint & Wallace, 1989). In contrast, studies concerned with quantifying the levels of the mixing taking place have been far fewer. Some exceptions are the experimental works of Konrad (1976), Breidenthal (1978, 1981), Koochesfahani (1984, 1986), Zhang & Schneider (1995), and Karasso & Mungal (1996, 1997).

Konrad used a concentration sampling probe in a non-reacting gaseous layer to infer the amount of mixing, whereas Breidenthal used an absorption technique in a chemically reacting liquid layer to deduce the amount of chemical product. They found that a rapid increase in the amount of mixing (or chemical product) occurred some distance downstream of the splitter plate, when the Reynolds number became sufficiently large. The increase in mixing (mixing transition) was attributed to the increase of interfacial area between the two fluids, which, in turn, was a consequence of the development of small-scale three-dimensional motions. In Figure 1.1.2 a plot is reproduced from Roshko (1990) which describes the mixing transition. The amount of mixed fluid normalized by the shear layer width is plotted versus large structure Reynolds number, $\Delta U\delta/\upsilon$, where $\Delta U = U_1 - U_2$, υ is the kinematic viscosity, $\delta = \Delta U \, / \, (\partial\bar{U}/\partial y)_{max}$ is the vorticity thickness, and $\bar{U}$ is the mean velocity. The vorticity thickness is linearly related to the 'visual thickness' of the shear layer, i.e. the width of the ‘wedge’ containing the large structures. As noted above, Huang & Ho (1990) related the development of small-scale motions to the interactions between the streamwise vortices and merging spanwise structures. The computational study of Moser &

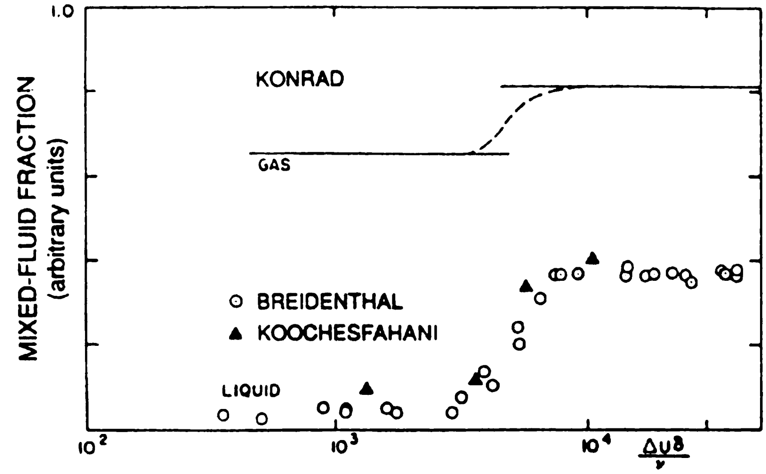

Figure 1.1.2. The mixing transition.

Rogers (1990) found that 'when the flow is sufficiently three-dimensional, a pairing can cause the mixing layer to undergo a transition to small-scale turbulence'. The mixing of a passive scalar was seen to increase with this small-scale transition.

Koochesfahani (1984) extended the application of laser-induced fluorescence (LIF) from a flow visualization tool to a mixing diagnostic. In his liquid layer, both chemically reacting and non-reacting (passive scalar mode) experiments were performed. The main results were that, during the mixing transition, the amount of mixed fluid increased and that, at the same time, the dominant mixed-fluid concentration changed. The initial roll-up of the vortical structures was found to be asymmetric such that the cores contained a large excess of high-speed fluid. The LIF technique is also used in the present study for both chemical product measurements and passive scalar measurements.

1.1.3 The Forced Layer

Some of the earlier works in (pre-mixing transition) shear layers (Freymuth, 1966; Browand, 1966) were undertaken in an attempt to establish a link between the instability of the flow and the onset of turbulence. However, the researchers found that there was a large amount of spatial 'jitter' in the flow. This was due to the fact that, in a natural layer, instability waves in a wide range of frequencies are amplified, even though there is a dominant natural frequency. The different phase-speeds of these waves then produced the irregularity which was observed.

As a remedy for this situation, low-level forcing at about the natural frequency was applied to the layers. This provided a clear phase reference which allowed more stable measurements to be made. It was thought that there was no effect on the dynamics of the flow, other than a decrease in broadband noise. It later became apparent (Oster & Wygnanski, 1982; Ho & Huang, 1982; Zaman & Hussain, 1981) that, in fact, external periodic oscillations at relatively low amplitudes can significantly affect the growth rate of the shear layer, and that the large structures can, to some extent, be controlled by them.

The dramatic effect of two-dimensional forcing on the layer growth rate is illustrated in Figure 1.1.3, which has been reproduced from Browand & Ho (1983). A representative segment for the growth rate of a natural layer has been included at the right hand side of this plot for comparison. The data for this plot were taken from the forced layers of Oster & Wygnanski and Ho & Huang. The data of Oster & Wygnanski were obtained at a high Reynolds number, post-mixing-transition layer, while those of Ho & Huang were produced mainly in pre-mixing-transition experiments. From this figure it can be seen that, as opposed to the linear growth found in natural layers, the forced layer experiences three different types of growth. Initially the growth rate is enhanced, compared to the natural case. Then there is a period of little or no growth, and finally the growth approaches that of the natural layer.

This plot shows the normalized growth rate as a function of the parameter,

$$x^* \equiv \lambda x f / U_c ,$$

first introduced by Oster & Wygnanski (1982). This dimension-less parameter encompasses the effects of the ratio, $\lambda = (U_1-U_2)/(U_1+U_2)$, to which the post-mixing-transition growth rates are proportional, the forcing frequency, f, the downstream distance, x, and the mean speed $U_c = (U_1+U_2)/2$. The growth of the layer is measured by the momentum thickness,

$$\theta = \int_{-\infty}^{\infty} \frac{(U_1-U)(U-U_2)}{(U_1-U_2)^2}\, dy,$$

which, in the plot, has been normalized by U_c / f, the wavelength of the perturbation.

Oster & Wygnanski found that they could segregate the flow into three main parts, representing the different response characteristics mentioned above. These regions of the flow were categorized as follows :

I $x^* < 1$: the growth rate is enhanced by a factor of 2 or more,

II $1 < x^* < 2$: the flow forms a periodic array of vortices with passage frequency equal to the forcing frequency; the growth rate is inhibited in this 'frequency-locked' region, even reduced to zero; Reynolds stresses are reversed in sign,

III $x^* > 2$: relaxation to unforced growth rate.

In the present work the effects on mixing are investigated as x^* is increased by raising the forcing frequency while maintaining a fixed downstream location. Many of the mixing results in Chapters 3 and 4 are plotted against the x^* variable.

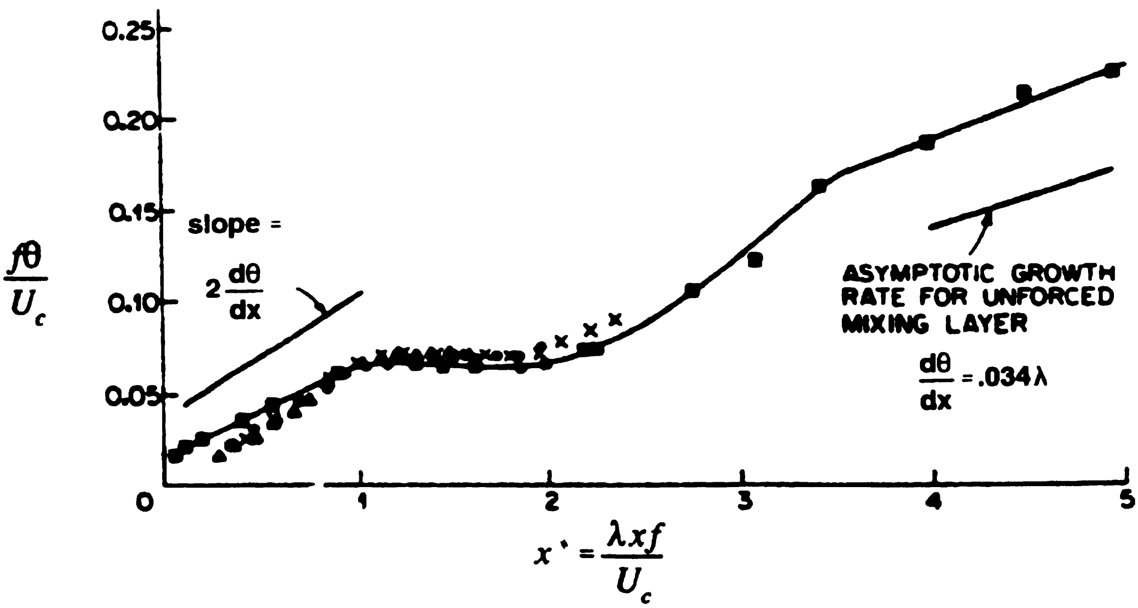

Figure 1.1.3. Shear layer growth versus x^*.

Ho & Huang (1982) showed how they could manipulate the growth rate and control vortex merging by forcing the layer at a subharmonic of the most-amplified (or natural) frequency. For example, forcing the layer at the first subharmonic produced pairing of neighboring vortices and forcing at the second subharmonic yielded 'tripling'. They also found that pairing took place at the downstream location where the energy of the subharmonic mode of the velocity fluctuation reached its peak. This illustrated the importance of the development of the subharmonic mode of the shear layer to the process of vortex merging.

Previous work in our lab (Koochesfahani & MacKinnon, 1991) concentrated on the effects of 2-D forcing on the passive scalar mixing field. The forcing frequencies used were much lower than the natural roll-up frequency ($f << f_o$). It was found that while the total amount of mixed fluid increased when forcing was applied the amount of mixed fluid *per unit width* of the layer remained nearly constant. That is, the increase in mixing was attributable more to the increased width of the layer rather than to any enhancement in small scale mixing. If the mixing efficiency were defined as the fraction of the layer filled with mixed fluid, the forcing did not in fact result in a more efficient mixer. Later results (MacKinnon & Koochesfahani, 1994) showed an increase in mixed fluid fraction as x^* was increased by using 2-D forcing at a higher frequency. The implementation of a 3-D perturbation in the low-speed boundary layer of the splitter plate resulted in significant spanwise variations of the amount of mixed fluid and the average mixed-fluid concentration. One again, when the amount of mixed fluid was normalized by the local layer width, it was found that the mixed-fraction fraction increased only for the higher frequency 2-D forcing, i.e. higher x^* values. One of the limitations of the passive scalar technique is that it typically overestimates the actual amount of mixing, unless the resolution of the measurements is extremely high (this issue is addressed further in Chapter 2). For a study of this type it is highly desirable to measure the true extent of mixing. This can be achieved by using LIF in the chemically reacting mode, as in the present work.

The study of Roberts (1985) is, to the best of our knowledge, the only other investigation to quantify the amount of chemical product in a liquid shear layer undergoing imposed 2-D perturbations. Roberts found that the effect of 2-D forcing can significantly alter the amount of chemical product in the layer. In pre-transitional flows there were large increases in the amount of chemical product in the frequency-locked region. In post-transitional flows increases were observed only in the very early stages of the enhanced growth region. The mixing data were obtained using an absorption technique which yields the integrated chemical product along the line of sight of an illuminating beam/sheet. Thus, the shear layer width is not available for these measurements. Also, the experiments were conducted at a single stoichiometric mixture ratio, from which it is not possible to extrapolate the total amount of mixing.

The forced studies cited above have all been concerned with the effects of two-dimensional forcing on various aspects of the shear layer. However, the intricacies of the interplay between the large scale spanwise structures and the streamwise vortical structures have recently received much attention. In order to facilitate studies related to the origin and evolution of the streamwise structures, several researchers have incorporated 3-D perturbations in a variety of forms to trigger the generation of these structures. Breidenthal (1980) was one of the first to perform such a study on shear layers and wakes, and utilized a splitter plate with a spanwise variation of either wedges or serrations at the trailing edge. His results showed that the shear layer readily developed the typical 2-D structures, and that further downstream there were no signs of the initial 3-D disturbance. Lasheras, Cho & Maxworthy (1986) placed a small cylindrical 'peg' alternately in one of the splitter plate boundary layers and found that the resulting horseshoe vortex induced regions of streamwise vorticity under the straining field of the spanwise structures. The streamwise structures were found to propagate laterally by self-induction. They also noted that whenever streamwise vorticity first appeared, it was always in the braid region between consecutive spanwise structures. Lasheras & Choi (1988) studied the effects of using two types of sinusoidal variations (indentations and corrugations) in the trailing edge of the splitter plate. They concluded that perturbations in the spanwise vorticity, subjected to the large straining field between the primary vortices, are stretched in the axial direction resulting in pairs of counter-rotating streamwise vortices whose axes are aligned with the direction of maximum strain. Nygaard & Glezer (1991) have studied the interactions of the spanwise and streamwise vortices and proposed a method by which these interactions lead to the generation of small scale three-dimensional motions. Bell & Mehta (1990, 1993) have measured turbulence transport quantities in shear layers with streamwise vorticity injection from a variety of sources including arrays of vortex generators, arrays of pegs, and corrugations at the splitter plate. They recorded significant changes in properties such as the layer growth and the Reynolds stress in the far-field.

1.2 Extension of molecular tagging velocimetry (MTV) to mixing studies

While most of the discussion so far has concentrated on quantifying various aspects of the mixing process, the fact remains that scalar mixing data are not sufficient, by themselves, for providing a detailed understanding of entrainment, whereby irrotational fluid is inducted into the layer, and mixing in turbulent flows. Additional flow kinematics are needed for this purpose. In recent years two-component velocity maps have been measured in many turbulent flows using particle image velocimetry (PIV) or molecular tagging velocimetry (MTV) approaches. Ongoing developments within our own lab regarding the MTV technique (Koochesfahani et al., 1996, Gendrich & Koochesfahani, 1997) have resulted in its successful implementation in shear layer and wake flows, among others. Although still at an exploratory stage in the present work, the MTV method has been combined with passive scalar LIF to allow the simultaneous whole-field measurements of velocity and concentration in a mixing layer. This technique allows the superposition of vorticity and mixing fields as well as the non-intrusive measurement of Reynolds fluxes such as $\overline{u'\xi'}$ and $\overline{v'\xi'}$, quantities which have typically been very difficult to record experimentally.

1.3 Objectives

The scarcity of molecular mixing results in forced shear layers motivated the present effort to quantify (via chemical reaction) the changes in the amount of mixing, the mixed-fluid fraction and the mixed-fluid composition occurring resulting from external 2-D perturbations in a shear layer.

Recent works incorporating streamwise vorticity injection mechanisms have reported significant influences on far-field turbulent statistics such as Reynolds stresses, attributed to the presence of the 3-D perturbations. Prompted by these results as well as our own previous work in the effects of 3-D forcing on the passive scalar mixing field, the present study sought to quantify the effect of vorticity injection on the molecular mixing field in a shear layer.

In a work independent from the above, the need for both mixing and kinematic data has led to the development of a technique to simultaneously measure velocity and concentration in a mixing layer. Although the technique is still in an evolutionary stage, the objective here was to demonstrate the potential of this approach.

1.4 Outline

Chapter 1 details background information relevant to the study of mixing in forced shear layers. The experimental procedures used are described in Chapter 2. The results for 2-D forcing are presented in Chapter 3, followed by those for 3-D forcing in Chapter 4. The last section of Chapter 4 contains a discussion and summary of these results. Finally, in Chapter 5 the technique for the simultaneous acquisition of velocity and concentration measurements is presented along with some preliminary results. This is followed by a brief summary of the main conclusions.

Chapter 2

EXPERIMENTAL FACILITY, FLOW DIAGNOSTICS AND INSTRUMENTATION

The experiments for the present study were conducted using the liquid mixing layer facility in the Turbulent Mixing Laboratory at Michigan State University. Data were acquired for a variety of 2-D/3-D forcing conditions in a shear layer using three different diagnostic procedures. In this chapter the details of the facility, the experimental set-up and the flow diagnostics are described.

2.1 Shear Layer Facility

The experiments were performed in a gravity-driven, liquid shear layer apparatus, a schematic of which is shown in Figure 2.1.1. The test-section has a cross-section of 4 cm (height) x 8 cm (span) and is 35 cm long. The free-stream speeds were nominally $U_1 = 40$ cm/s and $U_2 = 20$ cm/s, giving a velocity ratio of $r = 0.5$. The initial Kelvin-Helmholtz roll-up frequency was estimated from long temporal sequences of visual data to be approximately $f_o = 38$ Hz. Ho & Huerre (1984) have suggested that the initial most amplified wavelength is related to the initial momentum thickness via $\lambda_o \approx 30\theta_o$. Utilizing the present value for f_o results in an estimate for the initial momentum thickness, $\theta_o \approx 0.25$ mm.

Water was pumped from the two independent supply tanks up to the overhead tanks, where in each a constant head was maintained by making use of an overflow chamber. In addition, a constant head was maintained at the outlet of the test section. These measures

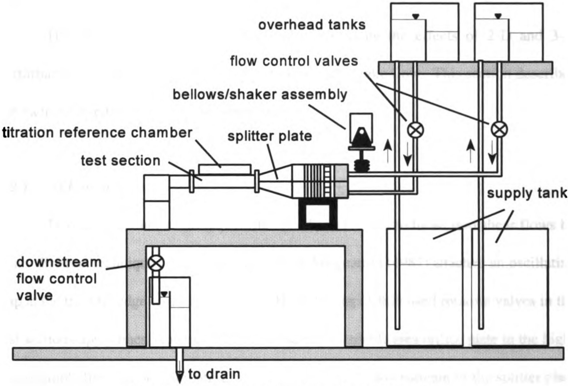

Figure 2.1.1 Schematic of experimental facility.

minimized fluctuations of the free-stream speeds which may have arisen as a result of time dependent boundary conditions at the inflow and outflow. The flow rates were controlled by three valves, one in each supply line upstream of the contraction, and one downstream of the test section. The upper stream was arbitrarily chosen to be the high speed stream for the shear layer experiments.

The development of the splitter plate boundary layers is an important consideration for our experiments. As a means to minimize non-uniform upstream conditions, extreme care was taken during the filling process to expel as much air as possible from the flow management screens and straws and from the underside of the splitter plate.

2.2 Forcing Mechanisms

The goal of the current study was to investigate the effects of 2-D and 3-D perturbations on the mixing field in a shear layer and a wake flow. This section describes the methods used to impose these perturbations.

2.2.1 2-D Forcing

Two-dimensional velocity perturbations have been introduced into shear flows by many different techniques. For example, Oster & Wygnanski (1982) attached an oscillating flap at the trailing edge of the splitter plate, Ho & Huang (1982) used rotating valves in the test section supply lines, Roberts (1985) constructed a variable area orifice plate in the high-speed supply line, and an oscillating airfoil placed slightly downstream of the splitter plate tip was used by Koochesfahani (1989). The oscillating airfoil technique was also used more recently by Katch (1993, 1994) for a mixing study in the same facility as the current experiments. His conclusions were similar to those in a previous bellows-forced layer in our lab (Koochesfahani & MacKinnon, 1991), indicating that the source of the 2-D disturbance is less important than other forcing parameters such as frequency and amplitude. Acoustic excitation is commonly used in gaseous flows.

In the present case, forcing was applied by means of an oscillating bellows operating in the high-speed supply line, upstream of the settling chamber. A schematic of the bellows mechanism and location may be seen in Figure 2.1.1. The motion was controlled by a magnetic coil vibrator and amplifier system (Vibration Test Systems VTS 50), the input to which was supplied by a function generator (Hewlett Packard HP3314A). Sinusoidal motions were used for all of the 2-D forcing cases. Three different relatively low forcing amplitudes were used. The rms perturbation levels in the high-speed free-stream were found to be less than about 4% for all cases.

2.2.2 3-D Forcing

As mentioned above, researchers have used a variety of ways to introduce 3-D perturbations into the shear layer. These typically take the form of spanwise modifications at the trailing edge of the splitter plate, e.g. wedges or serrations (Breidenthal, 1980), indentations or corrugations (Lasheras & Choi, 1988), a matrix of surface heater elements (Nygaard & Glezer, 1991), and arrays of pegs or right-triangular vortex generators (Bell & Methal, 1990, 1993). In the present case, since it was not possible to modify the splitter plate, the most convenient method of introducing 3-D perturbations was to place a single small cylindrical peg (Lasheras et. al, 1986), of diameter 7 mm and height 3 mm, on the centerline of the splitter plate about 1.5 cm upstream of the tip. The presence of this peg injected streamwise vorticity of both signs into the flow in the near-field region. Since the strength of the vorticity is expected to depend on the speed of the flow in the vicinity of the peg, three different configurations were used: no peg, peg on the low speed side and peg on the high speed side of the splitter plate.

2.3 Diagnostics

The results in this study have been obtained using three different experimental procedures: passive scalar laser-induced fluorescence (LIF), chemically reacting LIF and molecular tagging velocimetry. The former two methods provided a variety of mixing related information and are described briefly below; further details are available in

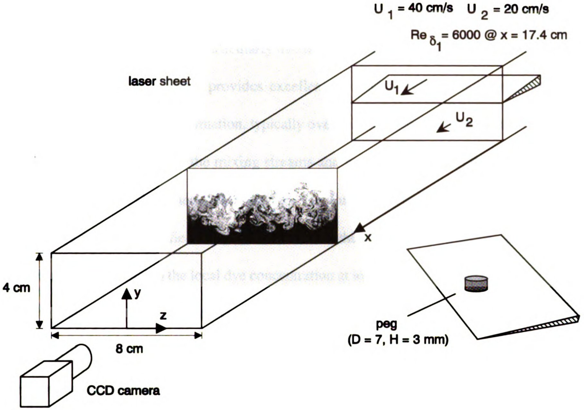

Figure 2.3.1 Shear layer experimental set-up for passive scalar LIF spanwise imaging

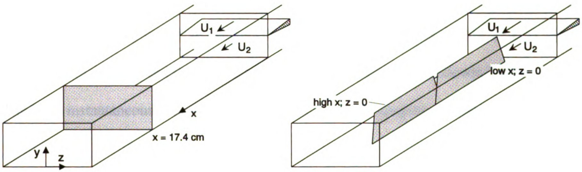

Figure 2.3.2 Laser sheet orientations used for shear layer LIF experiments

Koochesfahani (1984, 1986). The latter, used in conjunction with passive scalar LIF to yield simultaneous velocity/vorticity and concentration measurements, is introduced here and discussed further in Chapter 5.

2.3.1 Passive Scalar Laser-Induced Fluorescence

Passive scalar LIF is a particularly useful tool in the study of mixing flows. It is a non-intrusive technique which provides excellent flow visualization and can also yield quantitative concentration information, typically over a 2-D plane. Generally, a fluorescent dye is premixed with one of the mixing streams and becomes visible in the presence of a laser sheet. A CCD camera then records the fluorescence intensity, from which a quantitative concentration field can be obtained since the fluorescence intensity is known to be linearly proportional to the local dye concentration at low values of concentration (see e.g. Koochesfahani, 1984, Appendix A).

In the current experiments water from the low-speed stream is premixed with a solution of disodium fluorescein dye to an initial concentration of about $C_{d_0} \approx 2x10^{-7}$M (molar concentration). The low-speed fluid subsequently becomes diluted as it is mixed with the pure fluid from the high speed stream (water). Recording the fluorescence intensity yields the dye concentration, and therefore the relative concentration of high speed to low speed fluid in the layer, as can be seen from the following relationships. The local instantaneous concentration of the dye, C_d, in a sampling volume is given by

$$C_d = C_{d_0} \frac{\upsilon_2}{(\upsilon_1 + \upsilon_2)} ,$$

where υ_1 and υ_2 are the volumes of high speed and low speed fluid, respectively, within the sampling volume. Therefore the normalized concentration of high speed fluid, ξ , is

$$\xi = 1 - \frac{C_d}{C_{d_0}} ,$$

i.e. the high-speed fluid volume fraction, $\upsilon_1/(\upsilon_1 + \upsilon_2)$. Note that values of $\xi \approx 0$ and $\xi \approx 1$ correspond to pure low speed fluid and pure high speed fluid, respectively. Other values of concentration indicate mixed fluid. Concentration pdf's can then be used to compute various quantities of interest, such as the mixed-fluid probability and the mixed-fluid thickness, δ_m.

Illumination was provided by the beam from a 4 watt argon-ion laser (Excel 3000) which was focused through a converging lens and then passed through a cylindrical lens to produce a thin laser sheet (about 0.5 mm thick, or $2\theta_0$). A schematic of a typical experimental set-up for spanwise imaging is shown in Figure 2.3.1; an inset of the splitter plate is also shown with the peg on the high speed side. The sheet was imaged in three spanwise and three streamwise orientations for passive scalar data; the same orientations were used for the chemically reacting measurements, with the exception that the two upstream spanwise stations were not utilized. Figure 2.3.2 shows a schematic of these arrangements. Only a subset of this data has been incorporated into the present work since the focus here is on mixing effects near the end of the mixing transition.

The fluorescence intensities were recorded by a Sony XC-77RR CCD camera, which was operating at 60 fields/s with an exposure time of 1 msec. A Nikkor 50mm f/1.2 lens was used for streamwise imaging and a Nikkor 35mm f/1.8 lens was used for spanwise imaging. The camera contains a 2-D array of 768 (horizontal) x 484 (vertical) "pixels", of which 512 x 484 were digitized. In our streamwise imaging experiments, the 4 cm width of the test section was imaged onto about 230 pixels, resulting in a spatial resolution of 170 (H) µm x 170 (V) µm. The 512 horizontal pixels correspond to a streamwise range of about 9 cm.

The analog signal from the camera was digitized to 8 bits and stored on hard disk in real time (60 fields/sec) by a digital image acquisition system (Trapix 5500) with a capacity of 4.5 Gb, or almost 10 minutes of data at a resolution of 512 x 512 pixels. Typically, a sequence of 13 forcing cases was captured in a single automated acquisition. The available amount of reservoir fluid dictated that each individual forcing case was comprised of 1024 fields of data (or about 128 Mb). For the lowest forcing frequency (4 Hz) cases this record length corresponded to the passage of about 70 structures. It is believed that this record length is sufficient for the present purpose. The amount of useful reservoir fluid was maximized during the runs by implementing a trigger-controlled data acquisition board along with a GPIB board to control changes of the forcing frequency and amplitude.

The LIF technique has an important limitation, as noted by Breidenthal (1981), when used in the passive scalar mode. This technique typically overestimates the amount of mixed fluid (i.e. it provides an upper bound to the actual molecular mixing). The difficulty arises when the sampling volume of the measurement apparatus is larger than the smallest mixing scales, as is usually the case. It is then impossible to determine, within the resolution of the measuring device, whether or not two fluids are mixed. In the present case the smallest diffusion (Batchelor) scales are expected to be on the order tens of microns, significantly less than the 170 µm spatial scale resolved here. For all the drawbacks of the passive scalar mode it remains the simplest way to estimate the pdf of the concentration field. In order to make unambiguous mixing measurements the chemically reacting mode of LIF was used to quantify the mixing results reported here.

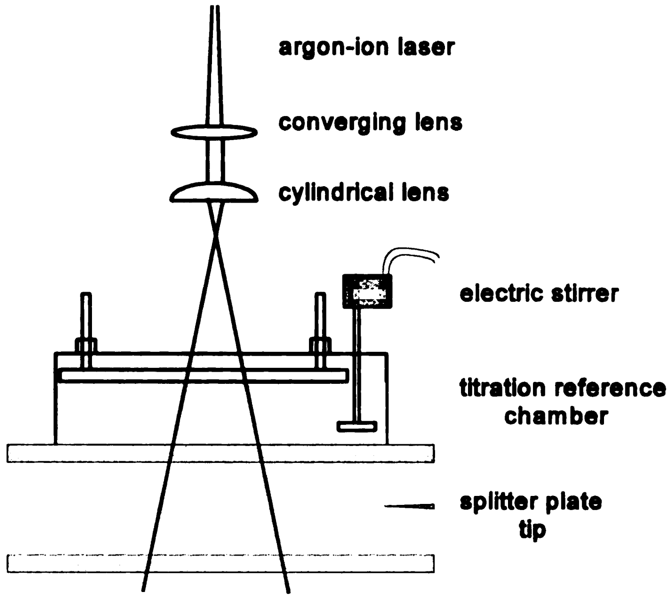

Figure 2.3.3. Optical set-up for chemically reacting LIF.

2.3.2 Chemically Reacting Laser-Induced Fluorescence

The chemically reacting mode of LIF (Koochesfahani, 1984, 1986) overcomes the limitations of its passive scalar counterpart by labeling only those parts of the flow which are molecularly mixed. This is achieved by exploiting the dependency on the local chemical environment of the dye's fluorescence capability. In the present case fluorescein has been used because of its sensitivity to pH. The chemical reaction is a diffusion-limited, acid (A)-base (B) reaction of the type $A + B \rightarrow P$ with the dye premixed in the acid solution. The fluorescence is "off" in an acidic environment with pH ≤ 4. Conversely, above this threshold the dye fluoresces efficiently in the presence of argon-ion laser illumination. Thus, at a reaction interface the local pH rises sharply and this is accompanied by a correspondingly rapid increase in the fluorescence intensity. This fluorescence intensity, I_f, is proportional to the chemical product concentration, C_p, where chemical product is defined here as the molecularly mixed fluid whose pH is above the fluorescence threshold. The normalized product concentration is then given by

$$\frac{C_P}{(C_P)_{max}} = \frac{I_f}{(I_f)_{max}} ,$$

where $(C_p)_{max}$ is the maximum possible product concentration (at fluorescence "turn-on") and $(I_f)_{max}$ is the corresponding maximum fluorescence intensity. Note that $(I_f)_{max}$ was available throughout the experiments in the titration reference chamber (see Figure 2.3.3). A plot of fluorescence intensity versus solution pH is shown in Figure 2.3.4a. For low pH the fluorescence is effectively 'turned-off', but as the pH increases above the threshold value (pH ≈ 4) a rapid increase in fluorescence occurs. The intensity increases with pH until a maximum is reached, at about pH ≈ 8, after which it remains essentially constant. Figure 2.3.4b shows the fluorescence intensity as a function of base volume fraction $\xi_B = \nu_B/(\nu_A+\nu_B)$ as the volume of base ν_B is increased during a titration of a fixed volume ν_A of the acid/dye solution. Unlike the intensity-pH behavior, which is a characteristic of the dye, the intensity-ξ_B curve depends on the relative concentrations of acid and dye solutions. The intensity is close to zero at low pH since the solution is very acidic. As base solution is added, a point is reached where the pH threshold is crossed and the fluorescence 'turns on'. After this peak is reached the addition of more base simply dilutes the dye solution, reducing the fluorescence intensity linearly, and ultimately to zero. In the experiments when the base solution is on the high-speed side and the acid/dye solution is on the low-speed side, the concentration of high-speed fluid, ξ, at any point in the flow is just the base volume fraction. Invoking the relationship between C_P and I_f given above, we can then obtain the linear

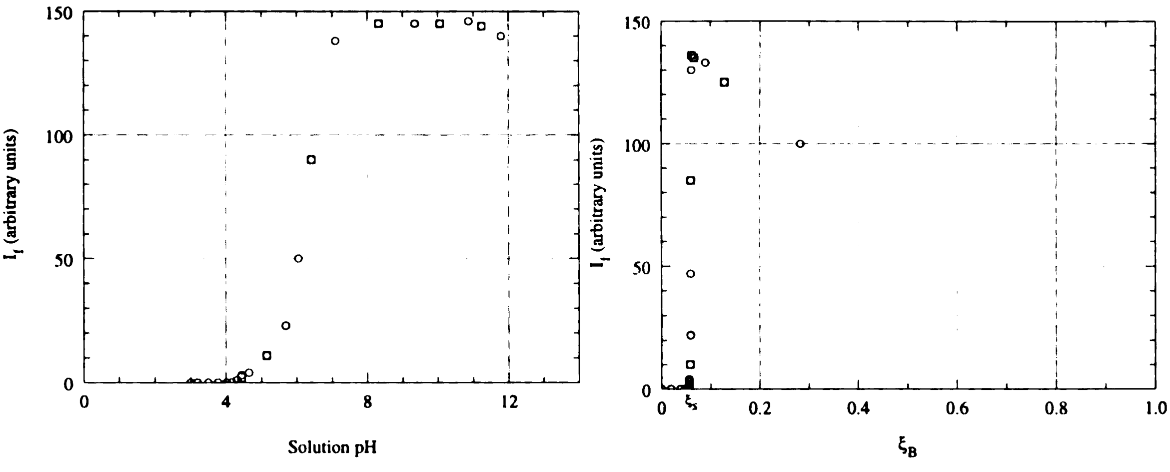

Figure 2.3.4 Fluorescence I_f versus (a) solution pH and (b) base volume fraction, ξ_B.

variation in C_P versus ξ, shown in Figure 2.3.5a. When the acid/dye solution is on the high-speed side this variation is reversed (Figure 2.3.5b). These 'one-sided' triangular forms will be referred to in later chapters. Koochesfahani (1984,1986) has shown that such 'flip' experiments, at low and high stoichiometric mixture ratios, can be used to obtain resolution free estimates for the amount of mixing via the relation, $\delta_m = \delta_{P1} + \delta_{P2}$.

Time-averaging the normalized product concentration field gives rise to profiles of the average product. These are integrated to compute the actual levels of molecular mixing,

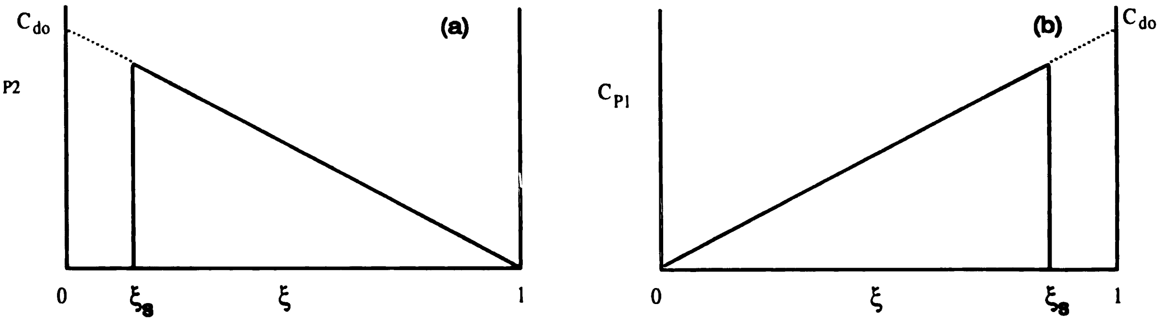

Figure 2.3.5 C_P versus ξ with (a) base on high-speed side and acid/dye on low-speed side and (b) base on low-speed side and acid/dye on high-speed side.

the so-called product thicknesses, δ_{P1} and δ_{P2} .

For the chemically reacting experiments the acid and base free-streams were dilute solutions of sulphuric acid and sodium hydroxide, prepared to pH values of about 3.2 and 12.1, respectively. The effect of density variations between the streams was minimized by adding a solution of sodium sulphate to the acid stream. The densities were matched to within a specific gravity of 0.0005.

2.3.3 Simultaneous Molecular Tagging Velocimetry (MTV) and LIF

The two prior flow diagnostics provide information relating to the flow structure and mixing field (concentration pdf's, amount of mixing, etc.) in a given flow. However, it is the structure and dynamics of the vorticity field which determine the flow behavior. Using molecular tagging techniques (Gendrich et al., 1997), based on novel supramolecular designs at MSU, a method has been developed to simultaneously measure the vorticity field, visualize the structure generated by this field, and record the corresponding concentration field. This type of information has not been obtained previously in a non-intrusive manner. A brief description is given here; further details are available in Chapter 5.

Molecular tagging velocimetry (MTV) is an optical technique typically used to measure two components of the velocity field at many points in a flow at the same time. The process relies on the long lifetime of certain phosphorescent lumophors. In our application, a grid of intersecting laser lines "tags" a region of the flow just after the laser fires and is recorded on a detector. A short time later, a second detector records the displaced grid after it has been convected a short distance by the flow. A spatial correlation approach then provides a local displacement vector, which is proportional to the velocity vector, for each intersection point on the initial grid.

By combining MTV with the standard LIF method i.e. by adding dye to one of the free-streams, and using a third camera, we can measure velocity and concentration at the same time. The schematic in Figure 5.2.2 displays the experimental set-up for the combined MTV/LIF runs.

As mentioned in the introduction we note that this technique is still under development. It has nevertheless provided initial estimates of quantities which are difficult to measure non-intrusively such as the velocity-concentration correlations $\overline{u'\xi'}$ and $\overline{v'\xi'}$, where u and v are the streamwise and transverse velocity components, respectively.

Chapter 3

TWO-DIMENSIONAL FORCING RESULTS

This chapter describes both qualitative observations from flow visualizations and quantitative results from the chemically reacting product measurements and properties derived from these measurements. First, results from the data obtained via streamwise imaging will be presented which will be followed by spanwise imaging results.

Throughout this chapter we will frequently quote results in terms of the dimensionless variable introduced in Chapter 1, namely $x^* \equiv \lambda x f / U_c$, where $\lambda = (U_1 - U_2)/(U_1 + U_2)$, x is the downstream distance, and $U_c = (U_1 + U_2)/2$ where U_1 and U_2 are the high- and low-speed free-stream velocities, respectively. Recall that Oster & Wygnanksi (1982) identified three important ranges for this parameter: $0 < x < 1$ represents a region of enhanced growth; $1 < x < 2$ refers to the "frequency-locked" region characterized by the passage of equally-spaced, non-interacting vortical structures; the range $x > 2$ is associated with the gradual relaxation to the unforced growth rate. Note that x^* is increased by increasing the forcing frequency at a fixed x location. Whether x^* is a truly useful scaling requires that we vary the x location also. Unfortunately this was not possible in the current facility for the reasons mentioned in section 3.2.1. For reference, the forcing frequencies normalized by the initial roll-up frequency, f_0, are f/f_0 = 0.11, 0.21, 0.42 and 0.82 for f = 4, 8, 16, and 32 Hz, respectively.

Due to the sheer volume of data, in certain figures we have elected to show flow images from only a single 2-D forcing amplitude. This is justified since, for about 75% of the experiments with forcing, the amplitude was found to have only very minor effects. Similarly, for readability in some plots we will only include the results of one amplitude. Additional data are included when necessary to highlight exceptional cases. Summary plots include data from all forcing conditions.

3.1 Streamwise evolution at mid-span

We first discuss the development of the shear layer in the streamwise direction at the mid-span location. Data were obtained from two different streamwise fields of view - an upstream view covering a range of about 2.5 cm ($100\theta_o$) $< x <$ 11.5 cm ($460\theta_o$), and a downstream view covering a range of about 11.5 cm ($460\theta_o$) $< x <$ 20 cm ($800\theta_o$). Figure 3.1.1 shows representative instantaneous images of the concentration field and the structure of the flow for various 2-D forcing frequencies. The flow is from right to left. The samples shown here have been forced at the intermediate amplitude; however, they are also representative of the flow structure for the other forcing amplitudes. In these images the high-speed free-stream concentration ($\xi \approx 1$) is labeled black and the low-speed free-stream concentration ($\xi \approx 0$) is labeled light grey; the mixed fluid concentrations are represented by darker shades of grey. The result of the Kelvin-Helmholtz instability is clearly seen in these views, where naturally occurring disturbances in the flow are amplified immediately downstream of the splitter plate. One of the most noticeable features of these images is that the growth of the forced layers is modified relative to that of the unforced layer. In particular, for the two lower forcing frequencies $f = 4$, 8 Hz, we see that their growth is restricted only by the test-section height at the regions furthest downstream. These views also highlight the frequency response of the forced shear layer. In each case, the structures being shed near the splitter plate tip, at the natural frequency of the layer, roll around and amalgamate with each other until the large structure passage frequency, at some distance downstream, becomes synchronized with the forcing frequency. Notice, for example, the quadrupling of four small structures at the extreme right side of the 8 Hz case, which becomes a single much larger structure further downstream. Such ‘collective interactions’ are characteristic for forcing where $f/f_0 << 1$ (Ho & Huang, 1982).

We focus now on the latter third of the downstream view. The downstream location x = 17.4 cm is labeled for reference since this is the location at which all the spanwise chemical reaction product measurements were made. At this fixed location we step through the range of x^* (= $\lambda x f / U_c$) values 0.77, 1.55, 3.1 and 6.2 by varying the forcing frequencies f = 4, 8, 16 and 32 Hz, respectively.

The flow regimes categorized by the x^* parameter are clearly identifiable at this downstream location - Figure 3.1.1(b) shows the enhanced growth phase (f = 4 Hz, x^* = 0.77); the frequency-locked region (f = 8 Hz, x^* = 1.55) is depicted in Figure 3.1.1(c); Figure 3.1.1(d) shows the beginning of a period of re-adjustment to the unforced growth rate (f = 16 Hz, x^* = 3.1); the flow in Figure 3.1.1(e) resembles the unforced layer, having reached the re-adjustment stage (f = 32 Hz, x^* = 6.2). Before 2-D forcing is applied, Figure 3.1.1(a), a weak braid region can be seen between the large structures, along with the incursion of unmixed free-stream fluids into the center of the layer. Much larger structures are seen in the enhanced growth and frequency-locked cases, together with correspondingly larger and more penetrative entrainment "tongues" of mostly unmixed fluid. This indicates that although the layer is wider and has entrained more fluid, much of it is still unmixed. We might therefore expect that for these two cases the amount of mixed fluid per unit width of the layer would not increase relative to the unforced layer. This qualitative assessment is in agreement with the plot of mixed-fluid fraction versus x^*, to be discussed in the next section. As we shall see, in fact at $x^* = 0.77$, 1.55, corresponding to the 4 Hz and 8 Hz cases, the mixed-fluid fraction is lower than for the unforced layer.

In contrast to the other cases in Figure 3.1.1 we see that for $f = 16$ Hz ($x^* = 3.1$) and, to a lesser extent $f = 32$ Hz ($x^* = 6.2$), there is no discernible braid in the vicinity of our measurement station ($x = 17.4$ cm). By the latter stages of the downstream view the organized structures and braid regions appear to have been broken down through a complex series of interactions. It is interesting to note that the 16 Hz case produced the largest value of mixed-fluid fraction, followed in value by that of the 32 Hz case ($x^* = 3.1$, 6.2, respectively, in Figure 3.2.8).

We focus momentarily on the unforced case alone. The shear layer width δ_1 in the unforced case was computed at many streamwise locations and is shown in Figure 3.1.2. The plot includes a range of asymptotic 'best-fit' growth rates for unforced shear layers (Brown & Roshko, 1974) at the present velocity ratio, with which the present data is in nominal agreement.

Breidenthal's (1981) plot of chemical product normalized by the local vorticity thickness versus Re_{δ_ω} for an unforced shear layer is reproduced in Figure 3.1.3 with data from the present case superposed. We have estimated the vorticity thickness using the ratio $\delta_1 / \delta_\omega = 2.1$ suggested by Brown & Roshko (1974). Note that Breidenthal's data were obtained using two velocity ratios, namely $r = 0.76$ and $r = 0.38$. For the present case the velocity ratio is $r = 0.5$ and this data falls between the latter two data sets. While the absolute magnitudes of the normalized product differ, the onset of the mixing transition appears to be bracketed appropriately within Breidenthal's results. It is also apparent that the location of our spanwise data measurements (at $Re_{\delta_\omega} \approx 2700$) corresponds to a Reynolds number near the end of the mixing transition.

The normalized product thicknesses for the unforced case is shown in Figure 3.1.4 as a function of downstream distance. This plot shows that a plateau is reached at the downstream end of the measurements. The values for these two limits for the present case of $r = 0.5$ and $\xi_s = 0.05$ are : $\delta_{P1}/\delta_1 \approx 0.208$ and $\delta_{P2}/\delta_1 \approx 0.148$. These values are higher than the limiting product thicknesses of $\delta_{P1}/\delta_1 \approx 0.165$ and $\delta\ /\delta_{P2} \approx {}_1 0.125$ quoted by Koochesfahani & Dimotakis (1986) obtained from experiments operating at $r = 0.38$ and $\xi_s = 0.09$. Karasso & Mungal (1996) operating at $r = .25$ and $\xi_s = 0.06$ report similar values ($\delta_{P1}/\delta_1 = 0.171, 0.174, 0.179$; $\delta_{P2}/\delta_1 = 0.125, 0.128, 0.132$ depending on Re) for their untripped cases. As we shall see in section 3.2 there is an element of spanwise variation in most of the measured quantities. Other factors potentially contributing to the observed differences may be due to test-section confinement issues, upstream initial conditions or non-zero pressure gradient effects. Such areas provide good sources for future study.

3.2 Spanwise Results

This section describes the effects of the 2-D forcing on the amount of mixing and the composition of the mixed fluid.

3.2.1 Amount of mixed fluid

Spanwise chemically reacting data were acquired at a downstream location of $x = 17.4$ cm. This location was chosen as a compromise between completion of the mixing transition and an attempt to minimize the interference of the test-section side walls. This location corresponds approximately to the third last data point on the mixed fluid fraction plots of the previous section and as mentioned above is near the end of the mixing transition.

Sample image time series of chemical product concentration C_{Pl} are shown in Figures 3.2.1-3.2.5 for the cases of no 2-D forcing, $f = 4$ Hz, $f = 8$ Hz, $f = 16$ Hz, $f = 32$ Hz using the intermediate forcing amplitude. Recall that in the C_{Pl} experiments the acid/dye combination comprises the high-speed free-stream. Since the shear layer rolls up with a bias of high-speed fluid more signal is obtained in these measurements. In these images the flow is coming "out of the page" toward the reader and the full cross-section (4 cm x 8 cm) of the test-section is shown to scale. The images highlight only the regions of the flow which are molecularly mixed with a local pH above the fluorescence "turn-on" threshold. This is in contrast to the passive scalar concentration images of the previous section which label one of the free-streams as well as the fluid which *appears* to be mixed. The shades of grey in these images are directly proportional to the normalized product concentration via the grey-scale map at the bottom of each figure. The product concentration can be related back to the high-speed fluid concentration using the 'triangle' plots of Figure 2.3.5. The eight images in each case are progressive in time and are arranged in column sequential order. The Δt between successive images is 1/60 second.

The first case, that of the unforced flow, shows samples of the braid regions between larger structures, which contain relatively low levels of mixing (e.g. frame 5), as well as the cores of larger structures indicated by significantly more mixed fluid (e.g. frames 3 and 8). While the regions of mixed fluid form a highly convoluted interface with the free-streams they are confined, on the average, to about the middle two-thirds of the test-section height.

Regions which may be inferred to contain streamwise vorticity can be seen in each frame, mostly in the form of 'mushroom-shaped' counter-rotating pairs.

In Figure 3.2.2 ($f = 4$ Hz, $x^* = 0.77$) we are monitoring the passage of a very large structure. The first frame shows the connective braid region between a large structure which has just passed by and the structure about to come. The core of the structure contains a large amount of mixed fluid and occupies a correspondingly larger fraction of the test-section height compared to the cores of the unforced case. One can easily imagine a temporally periodic variation in the amount of mixed fluid synchronized to the forcing frequency. In fact, due to the large amount of free-stream fluid and the low amount of mixing accompanying the braid regions, the probability of finding mixed fluid at the centerline ($y = 0$) is lower than that of the unforced case. Secondary streamwise structures appear to be randomly distributed throughout many of the frames.

The $f = 8$ Hz, $x^* = 1.55$ case is shown in Figure 3.2.3. In this sequence we see the core of a large structure, then the braid region which is followed in turn by the passage of the next core. Once again, the cores exhibit a substantial amount of mixed fluid and occupy a large fraction of the test-section height. An interesting feature of this series of images is that many of them display a crude spanwise periodicity of the secondary streamwise structures (see, for example, the last two images).

Turning our attention to the $f = 16$ Hz, $x^* = 3.1$ case of Figure 3.2.4 we can immediately notice a lack of a braid region in any of the frames. There is a large amount of mixed fluid in every frame. A time average of the product concentration field would be expected to yield a much larger amount of mixed product than in any of the previous cases. This is borne out in the mixed-fluid plot discussed below. Also, the flow structure in this series looks as though it has a different character from the preceding cases - there seems to be less contrast or variation in the product concentration and the flow has the appearance of being more 'lumpy'.

Figure 3.2.5 ($f = 32$ Hz, $x^* = 6.2$) shows flow patterns somewhat reminiscent of the unforced case, but once again without the presence of braid structures. The shear layer is evidently thinner here compared with the other forced cases.

In determining the amount of product a large number of images like those just discussed are averaged. Line profiles are then extracted at many spanwise locations. These profiles are then normalized according to the procedures outlined in Chapter 2. The amount of mixed product δ_{P1} or δ_{P2} is then the area under the normalized profiles. The profiles are also used to estimate the shear layer width, δ_1. The average C_{P1} product images for the forced cases are shown in Figure 3.2.6. As before the lighter greys indicate higher product concentrations. We can see the larger layer widths for the lower two frequencies compared to those of the $f = 32$ Hz ($x^* = 6.2$) case, for example. There is evidence of weak three-dimensionality in the center (vertically) of the layer for $f = 16$ Hz ($x^* = 3.1$), as well as much weaker corrugations at the upper and lower edges of the layer for $f = 4$, 8 Hz ($x^* = 0.77$, 1.55). The unforced case is shown in Figure 4.2.15 for comparison with the 'unforced' peg cases.

We now quantify the amount of mixed fluid in the layer. Using the procedure referred to above the mixed fluid thickness, $\delta_m = \delta_{P1} + \delta_{P2}$, was acquired for all the forcing cases at many points in the spanwise z-direction, along with the visual thickness, δ_1, so that the mixed-fluid fraction, δ_m / δ_1, could be computed. The results are summarized in Figure 3.2.7 for the intermediate forcing amplitude cases.

In terms of the amount of mixed fluid shown in Figure 3.2.7(a) the 16 Hz case consistently has the highest values. This is followed at significantly lower values at $f = 32$ Hz. Lower again are the $f = 4$, 8 Hz cases which show only marginally more mixed fluid than the unforced case.

The shear layer width is plotted in Figure 3.2.7(b). As noted from the instantaneous and averaged product concentration images, the 4 and 8 Hz cases have the largest layer widths. When the amount of mixed fluid is normalized by the local layer width these two cases then naturally produce the lowest levels of the mixed-fluid fraction as shown in part (c). The unforced layer and the 32 Hz cases show comparable layer widths and consequently their respective mixed-fluid fractions retain the same relative magnitudes as their mixed fluid thicknesses. The largest value of mixed-fluid fraction is attained by the 16 Hz case, with a width just larger than the unforced case but a much greater mixed-fluid thickness.

In order to characterize each case in the simplest possible way the various quantities described above have been averaged across the span and the results are plotted in Figure 3.2.8 versus the dimension-less variable x^*. In addition, all of the forcing amplitudes have been incorporated into these plots so that the effect of the forcing amplitude can now be quantified. In this plot 'a1' refers to the highest amplitude, and 'a3' to the lowest. The corresponding spanwise rms fluctuations for each quantity follow in Figure 3.2.9.

The span-averaged plots shown in Figure 3.2.8 confirm the trends just described from the plots of the spanwise variation of $\delta_m(z)$, $\delta_1(z)$ and $(\delta_m/\delta_1)(z)$. The most noticeable feature of the span-averaged mixed-fluid plot (figure 3.2.8(a)) is that the variation in forcing amplitude has a small effect on the amount of mixed fluid with the exception of the $x^* = 3.1$ ($f = 16$ Hz) cases. At this frequency the flow exhibits a strong sensitivity to very small changes in forcing amplitude. The reason for this sensitivity is not clear from the present study. Also, at $x^* = 3.1$, these cases are the only ones which reflected significant changes in the shear layer width. In contrast, the mixed-fluid fraction is not nearly as sensitive to forcing amplitude.

The rms fluctuations plotted in Figure 3.2.9 indicate that compared to the unforced layer the two highest x^* regions display the largest levels of fluctuations in each of the three quantities. The lowest amplitude component at $x^* = 3.1$ shows the greatest fluctuations. This may be due to the higher amplitude forcing inducing a more two-dimensional behavior. Qualitative confirmation may be seen in Figure 3.2.6(c,a3). These plots will be compared later with their counterparts from the experiments with 3-D forcing.

The final plot in this section (Figure 3.2.10) shows the mixed-fluid fraction for each forcing case as a percentage of the mixed-fluid fraction from the unforced case. On a per-unit-layer-width basis the intermediate amplitude case at $x^* = 3.1$ displays approximately 35% more mixing than the unforced case.

3.2.2 Composition of mixed fluid

We turn our attention now to the composition of the mixed fluid. This is an important part of any mixing control strategy; it is clearly undesirable if an attempt at mixing control produces enhanced mixing but at an unwanted mixture composition. The results which follow are based on the same spanwise chemically reacting LIF image data as the previous section.

Insight into the composition of the mixed fluid by is revealed by computing the average concentration of the *mixed* fluid, $\xi_M(z)$, which is shown (Koochesfahani, 1984, 86) to be given by

$$\xi_M = \frac{\delta_{P1}}{\delta_{P1} + \delta_{P2}} ,$$

where δ_{P1} and δ_{P2} are the product thicknesses from measurements at high and low stoichiometric mixture fractions, respectively. $\xi_M(z)$ represents, at a given z-location, the average mixed-fluid concentration across the extent of the layer in the y-direction.

Figure 3.2.11 shows the variation of $\xi_M(z)$, over almost 90% of the span, for the 2-D forcing cases at the intermediate amplitude. The most noticeable feature here is that the f = 16 Hz case shows a different type of behavior from the other cases. Whereas the unforced layer and f = 4, 8, 32 Hz (x^*=0.77, 1.55, 6.2) exhibit little spanwise variation, the mixed-fluid concentration at f = 16 Hz (x^*=3.1) shows a large decrease across most of the span. In other words, $\xi_M(z)$ is almost invariant with x^* until some point above $x^* = 1.55$, where it becomes significantly modified, and finally returns to an invariant state sometime before reaching $x^* = 6.2$. A value of 0.5 corresponds to a 1:1 mixture of high-speed stream to low-speed stream fluid. At some z locations ξ_M is below 0.5, indicating that more low-speed fluid is mixed on average!

A further averaging of $\xi_M(z)$, with respect to z, yields the span-averaged mixed-fluid concentration, $\overline{\xi_M}$. This quantity is plotted in Figure 3.2.12 for all of the forcing amplitudes and confirms the description just given. Note that it is only one of the amplitudes at $x^* = 3.1$ which produces the dramatic effect of altering the average concentration from that of the unforced flow, $\overline{\xi_M} \approx 0.59$, to a value of $\overline{\xi_M} \approx 0.5$. That this is indeed dramatic is apparent when one considers that the imposed forcing on the shear layer, with one free-stream twice the speed of the other, has resulted in a 1:1 mixture composition usually attributed to that of a wake flow with equal speeds! The spanwise rms concentration fluctuations are shown in Figure 3.2.13 and depict, as we might expect, the highest values for $x^* = 3.1$ ($f = 16$ Hz).

As qualitative confirmation of this drop in concentration we include in Figure 3.2.14 and Figure 3.2.15 sample images within the $x^*= 1.55$ and $x^* = 3.1$ regimes from the two chemical product experiments. To interpret the intensities represented in these images we recall that the product concentration C_{P1} is related to the high-speed fluid concentration ξ via the 'triangle' plots in Figure 2.3.5 . Figure 3.2.14 shows samples from the high stoichiometric mixture fraction experiment; thus increasing C_{P1} values correspond to increasing ξ values. In comparing the two images the lower image for the most-part contains *darker* shades of grey than the upper image. This corresponds to *lower* concentrations as indicated in the span-averaged mixed-fluid concentration plot. A similar effect is seen in Figure 3.2.15 which shows samples from the low stoichiometric mixture fraction (C_{P2}) experiments. However, in this case it is the *lighter* greyscales (lower image) which correspond to *lower* concentrations, according to the "calibration" plot in Figure 2.3.5.

A third pair of samples in Figure 3.2.16 confirms the above conclusions in perhaps a more dramatic fashion. These images were obtained from the passive scalar LIF technique, which highlights the two free-streams as well as the mixed fluid. The high-speed fluid concentration is labeled according to the colormap at the bottom of the figure. At $x^* = 1.55$ the mixture is mostly yellow corresponding to relatively high concentrations, whereas at $x^* = 3.1$ the dominant color is green indicating midrange high-speed fluid concentrations.

Chapter 4

THREE-DIMENSIONAL FORCING RESULTS

This chapter describes the results of the effects of combined 2-D/3-D forcing on the mixing field and the composition of mixed fluid. The 3-D forcing takes the form of streamwise vorticity injection near the tip of the splitter plate due to the presence of a small cylindrical disturbance element, or 'peg', in one of the two splitter plate boundary layers. Two sets of experiments were conducted - those with the peg in the low-speed boundary layer and those with the peg in the high-speed boundary layer. Qualitative observations from flow visualizations as well as quantitative results from the chemically reacting product measurements and properties derived from these measurements are presented. The type of 3-D forcing used is indicated in figure captions and legends etc. by the use of either of the abbreviations "LS" or "HS", referring to whether the disturbance element is on the low- or high-speed side of the splitter plate, respectively. The word 'unforced', in quotes, is used in reference to the flows for which the peg is present, but which do not have imposed 2-D forcing.

4.1 Streamwise Flow Structure at Mid-Span

Sample streamwise flow images acquired using passive scalar flow visualization for the case of 3-D forcing in the low-speed boundary layer are shown in Figure 4.1.16. As in the previous chapter the upstream and downstream views are created from two independent sets of experiments and, in general, the two images selected in each pair are not necessarily in phase. In comparing these views with the case of no 3-D forcing we see that the same type of large scale features are present. Before 2-D forcing is applied we can see braid regions accompanied by mostly unmixed free-stream fluid connecting the larger structures. The downstream views at $f = 4$, 8 Hz correspond to the enhanced growth and frequency-locked regions, respectively. The layer is wider in both cases but clearly contains a large amount of unmixed fluid. In the region of re-adjustment to the unforced growth rate, the $f = 16$, 32 Hz cases show very little braid structure.

There are some subtle differences, however, compared to the no-peg case. Beginning at the farthest upstream locations, the interface between the high- and low-speed streams is much less sharply defined and appears to contain more small scale structures and more mixed fluid. These additional disturbances in the flow structure are attributed to the presence of the peg.

The peg's influence on the flow structure appears even greater when the source of the 3-D forcing is in the high-speed boundary layer, as can be seen in Figure 4.1.17. As for the two previous cases, the various x^* regimes are clearly identifiable, and we may infer similar conclusions regarding the amount of mixing taking place. However, although the large scale structures are still evident, they appear to have less free-stream fluid associated with them and the cores appear to be more well-mixed than in the previous case. The spanwise views in the next section will illustrate further the significant disturbances caused, in particular, by the peg on the high-speed side of the splitter plate.

4.2 Spanwise Results

First we describe the effects of the 3-D forcing on the amount of mixed fluid which results. This is followed by an account of the forcing effects on the composition of the mixed fluid.

4.2.1 Amount of mixed fluid

Short time-sequences of chemically reacting (C_{Pl}) flow visualization images are shown in Figures 4.2.1 - 4.2.5 for the case of 3-D forcing on the low-speed side of the splitter plate. The sequences shown were obtained using 2-D forcing at the intermediate amplitude. The overall flow behavior is similar to the cases without 3-D forcing from the previous chapter. In particular, the alternating passage of braid regions and core regions is easily inferred for the cases of no 2-D forcing, $f = 4$ Hz ($x^* = 0.77$) and $f = 8$ Hz ($x^* = 1.55$) in Figures 4.2.1-4.2.3. The higher frequency cases ($x^* = 3.1, 6.2$) once again show a lack of any braid structure (Figures 4.2.4-4.2.5). There is, however, an interesting structural difference in the vicinity of the center-span which is noticeable in Figures 4.2.1 - 4.2.3. The first two frames in Figure 4.2.1 show good examples of the feature in question. These frames show the layer almost separated into two regions of mixed fluid in the vicinity of $z = 0$. The effect is not quite so strong but is nonetheless still present for $f = 4, 8$ Hz. More solid confirmation of this observation is available in the time-averaged product images of Figure 4.2.6. A distinct "indentation" into the lower edge of the shear layer in the averaged images can be seen for essentially all of the cases except $f = 16$ Hz, about which it is difficult to make the same conclusion. It is speculated, albeit in an over-simplified way, that the streamwise vorticity in the legs of the horseshoe vortex generated by the peg has remained sufficiently coherent to cause, on the average, an up-wash of low-speed fluid near the center-span of the layer. Images from a low speed shear layer shown later in section 4.3 indicate the same relative sense of vorticity portrayed by this argument.

Various quantities of interest have been computed by extracting profiles from the average product images at many z-locations. The results are plotted in Figures 4.2.7-4.2.9.

The mixed-fluid thickness (δ_m), visual thickness (δ_1) and mixed-fluid fraction (δ_m/δ_1) are shown in Figure 4.2.7 for the subset consisting of the intermediate forcing amplitude. The mixed fluid thickness plot depicts an undulating variation across the span with less mixed fluid in the central portion of the test-section compared to off-center regions particularly for the cases of no 2-D forcing, and $f = 4$, 8 Hz. The regions with less mixed fluid coincide with the regions of the "indentations" in the average product images. As in the previous chapter, the two higher frequency cases show more mixing than the other cases.

The layer widths, δ_1, in general show less significant variations across the span than the mixed-fluid thickness. The two higher frequency cases have widths comparable to that of the 'unforced' case, all of which are narrower than those for $f = 4$, 8 Hz.

The mixed-fluid fraction, δ_m/δ_1, shows more mixing per unit width of the layer for the two higher frequency cases than the 'unforced' case, which in turn has larger values than the two lower frequency cases. The two peaks in the $f = 16$ Hz case have resulted from locally relatively high mixing levels coupled with slightly smaller layer widths, and are expected to be related to the signature of the peg.

The observations just described are very similar to those which resulted when there was no 3-D disturbance. This fact is better illustrated by the span-averaged versions of the three quantities just presented, depicted in Figure 4.2.8. The plots in this figure essentially parallel those in Figure 3.2.8., both in terms of trends and magnitudes. The only exceptions are due to the high sensitivity displayed by the two larger amplitude $f = 16$ Hz cases in the $\overline{\delta_m}$

and $\overline{\delta_1}$ plots. Once again, the mixed-fluid fraction shows little sensitivity to forcing amplitude.

In comparing these three plots with similar plots from the no-peg case it is clear that, in spite of the modifications noted above due to 3-D (LS) forcing, at a given x^* location we have not in fact achieved either more mixing or more mixing per unit width of the layer. In fact, within this comparison, the largest value of mixed-fluid fraction appears for a case without 3-D perturbation.

The spanwise rms plots of the same three variables are shown in Figure 4.2.9. The 'unforced' and $f = 4$, 8 Hz cases in the rms δ_m plot show much higher rms fluctuations than their no-peg counterparts. The 'unforced' layer width δ_1 rms is only moderately higher than for the no-peg case. All other cases, however, show fluctuations more or less comparable to those without 3-D forcing. Once again the $x^* = 3.1$ ($f = 16$ Hz) cases show a greater sensitivity to forcing amplitude.

We turn our attention now to the case when the 3-D disturbance element is placed on the high-speed side of the splitter plate. This is the case which shows the largest increase in the amount of mixed fluid, although not in the mixed-fluid fraction.

Sample time series of instantaneous chemical product images (C_{P1}) are shown in Figures 4.2.10-4.2.14. Each set except for $f = 16$ Hz ($x^* = 3.1$) shows data acquired with the intermediate 2-D forcing amplitude; the 16 Hz set, having been forced at the highest amplitude, is depicted here because it resulted in the largest amount of mixed fluid which was recorded in the current experiments, as well as providing significant mixed-fluid composition effects. In the first set (Figure 4.2.10), that of the 'unforced' case, we can still distinguish braid regions and large structure core regions. There is perhaps also evidence of a counterpart to the 3-D (LS) forcing 'indentation' seen earlier in this section, but on the opposite side of the shear layer, commensurate with the change in sign of the streamwise vorticity. For example, near the center-span portion of frames 1, 6 and 7 there appears to have been an incursion of unmixed fluid on the upper side of the shear layer. While one could draw attention to many similar features across the span, the existence of a repeatable effect at this location is borne out by the time averaged product image. Figure 4.2.15(c) shows the 'unforced' average product image for this case, and includes the analogous images from the cases of no 3-D forcing and 3-D (LS) forcing for comparison in parts (a) and (b), respectively.

Returning to the time series data, the $f = 4$, 8 Hz cases indicate the passage of large coherent structures connected by relatively quiescent braids, along with a lot of seemingly energetic small scale activity. These cases also show a well defined "wiggle" in their average product images in Figure 4.2.16. Additionally, there appear to be counter-rotating vortical structures thrust towards the bottom side of the test-section in many of the frames. These features, too, are repeatable enough to show up in the average product images.

For the final two cases, $f = 16$, 32 Hz ($x^* = 3.1$, 6.2) we are not surprised at the lack of appearance of a braid structure. The 16 Hz case indicates a particularly large amount of mixed fluid. As mentioned earlier, this case in fact produced the largest average mixed-fluid thickness from all of the current experiments. The average product images for this case, Figure 4.2.16(c), show a much more significant degree of contortion than all the other cases. This must be attributed to the disturbance element on the high-speed side of the splitter plate.

We now discuss the mixing related quantities computed from the average product images. The mixed-fluid thickness plotted in Figure 4.2.17(a) shows a much larger amount of mixed fluid for the 16 Hz case relative to the other cases. The remaining cases have comparable levels of mixed fluid and show a well-defined reduction in mixed fluid over about the middle third of the test-section span. All of the profiles show some degree of undulation. The layer width plot in Figure 4.2.17(b) also shows an undulatory nature, with relative peaks near the center-span, for each of the profiles. As in the previous cases the widths associated with the *f* = 4, 8 Hz are larger than the "unforced" and 32 Hz cases; the 16 Hz case is wider this time having been forced at the highest amplitude.

The mixed-fluid fraction (Figure 4.2.17(c)) shows widely varying profiles for the two highest frequencies. The 'unforced' case has a greater mixed-fluid fraction than that at the two lower frequencies; all cases show a relative drop in value at locations near their mid-sections compared to those closer to the side-walls.

These results are summarized in the span-averaged plots of Figure 4.2.18. The trends are very similar to those of the no 3-D forcing and 3-D (LS) forcing conditions. An exception for the span-averaged mixed-fluid thickness is that it is not only the highest amplitude case at $x^* = 3.1$ which has a large value - the lowest amplitude case has a relatively high value, also. Compared to the 'unforced' case, forcing at $f = 16$ Hz and at high amplitude has resulted in over 50% more span-averaged mixed fluid. However, as we can see from the span-averaged mixed-fluid fraction plot, on a per unit layer width basis, we do not in fact achieve greater mixing efficiency.

The rms variations across the span of δ_m, δ_l and (δ_m / δ_l) are shown in Figure 4.2.19. The mixed-fluid rms values are much higher compared to those when 3-D forcing is absent (Figure 3.2.9). The rms fluctuation in the 'unforced' 3-D (HS) case is more than twice the corresponding value when there is no 3-D forcing. When 2-D forcing is applied in addition there are significant increases in rms variation at each x^* location. It is clear that the peg is exercising a strong spanwise influence on the mixing field.

Making similar comparisons for the rms fluctuation in shear layer width shows that the "unforced" 3-D (HS) case has only slightly higher variations than the unforced, no peg case. Also, very large fluctuation levels are found for the two lower amplitude 16 Hz, 3-D (HS) cases. The fluctuations in the mixed-fluid fraction are found to be greatest for the high amplitude 16 Hz 3-D (HS) case, followed closely by the 32 Hz 3-D (HS) cases.

4.2.2 Composition of mixed fluid

In this section we describe the effects of the 3-D forcing on the average mixed fluid concentration, ξ_M. Figures 4.2.20 (a) and (b) shows the spanwise variation of this quantity for the 3-D (HS) and 3-D (LS) forcing cases, respectively. Again the high amplitude $f = 16$ Hz case is plotted here (part (a)), whereas the intermediate amplitude is used for the remaining cases. When the source of the disturbance is on the high-speed side of the splitter plate a well-defined 'wiggle' in ξ_M is found across the span for each forcing case. This wiggle is expected to be due to the signature of the streamwise vorticity generated by the peg. The cases of no 2-D forcing, $f = 4$, 8, and 32 Hz essentially coincide, showing a lower mixed-fluid concentration near mid-span and higher concentrations at off-center spans locations. For $f = 16$ Hz the trend just described completely reverses, indicating a very significant modification of the interplay between the spanwise and streamwise structures. Similar results, although not as dramatic, are found for the case of 3-D (LS) forcing (Figure 4.2.20(b)). It is interesting here that the wiggle patterns show the same characteristics regardless of whether the peg is on the high-speed or low-speed side of the splitter plate, since one would expect a reversal in the sign of the streamwise vorticity when the peg location is switched.

The span-averaged versions of these profiles are shown in Figure 4.2.21. Both plots show similar trends, with the exception of the variations at $x^* = 3.1$ ($f = 16$ Hz). It is apparent that the zone around $x^* = 3.1$ is highly sensitive to the forcing amplitude in terms of mixture composition modifications. The spanwise rms fluctuations in ξ_M are shown in Figure 4.2.22. For 3-D forcing on the low-speed side (Figure 4.2.22(b)), these variations are comparable to those with no peg. In contrast, the 3-D (HS) case of Figure 4.2.22(a) shows significant increases in the levels of fluctuation for all forcing cases.

The next two figures give qualitative confirmation of the spanwise variation in concentration. Figure 4.2.23 shows two instantaneous chemical reaction images forced at $f = 16$ Hz ($x^* = 3.1$). Figures 4.2.23(a) and (b) show product concentration C_{P1} and C_{P2} images, respectively. We note from the triangle plots of Figure 2.3.5(b) that the C_{P1} product concentration increases as the high-speed fluid concentration increases. On the other hand an increase in C_{P2} product concentration indicates a decrease in the high-speed fluid concentration (Figure 2.3.5(b)). We can see a bright patch near the center of the product concentration field in the upper image of Figure 4.2.23 flanked on both sides by darker shades of grey. The colormap shows this to be a 'low-high-low' product concentration variation across the span. The actual high-speed fluid concentration is then also 'low-high-low'. The same effect is seen in Figure 4.2.23(b). This time the product variation across the span is seen to be 'high-low-high'. Referring once again to the triangle plots of Figure 2.3.5 we find the high-speed fluid concentration variation to be 'low-high-low'. A sample image pair from the low-speed 3-D forcing passive scalar experiments is shown in Figure 4.2.24. Here the high-speed fluid concentration may be read directly from the colormap shown. The upper image ($f = 4$ Hz, $x^* = 0.8$) has a 'yellow-green-yellow' variation across the span indicating a 'high-low-high' high-speed fluid concentration, in agreement with Figure 4.2.20. The lower image indicates a high-speed fluid concentration variation which is the reverse of that just described, also in agreement with Figure 4.2.20.

In summary, while the presence of the 3-D disturbance does indeed have a definite effect on the structure of the flow, the total amount of mixing, fluctuations in the mixing field and undulations in the average mixed-fluid concentration, it does not lead to more efficient mixing, i.e. on a per unit layer width basis. This is reflected in Figure 4.2.25 which indicates that the highest mixed-fluid fraction recorded during these experiments was obtained from a case without 3-D forcing. The main message here is that data from purely 2-D forcing and from combined 2-D/3-D forcing (regardless of forcing amplitude) all follow a similar trend. The mixed-fluid fraction initially decreases and is lower than the unforced case in the range $x^* < 2.0$. Mixing enhancement relative to the unforced case then increases beyond $x^* > 2.0$ until it reaches a peak and begins to reduce. However mixing enhancement over the unforced case is maintained at least until $x^* = 6$. A discussion of the main observations from Chapters 3 and 4 follows in the next section.

4.3 Discussion of results from Chapter 3 and Chapter 4

One of the goals of the present work was to attempt to answer the question of whether or not the injection of streamwise vorticity into a turbulent shear layer enhances molecular mixing. The work was motivated by previous passive scalar results in our lab

(Koochesfahani & MacKinnon, 1991, MacKinnon & Koochesfahani, 1994) and the turbulence measurements involving vorticity injection (e.g. Bell & Mehta, 1990, 1993). Our earlier passive scalar study showed that 2-D forcing of a shear layer ($f << f_0$), while increasing the total amount of mixed fluid in correspondence with the enhanced shear layer spreading, did not in fact lead to more efficient mixing, defined in terms of the mixed-fluid fraction. Our latter work found that enhanced mixing efficiency could be achieved by forcing at a higher frequency ($x^* \approx 3$). It was expected that a further enhancement of the small scale mixing could take place in the presence of increased turbulent transport due to injected streamwise vorticity at the splitter plate tip. At the same time, higher 2-D forcing frequencies were added to the list of forcing parameters. Contrary to our expectations, essentially the same trends, including magnitudes, were found in the mixed-fluid fraction, δ_m / δ_1, versus x^* for purely 2-D forcing and combined 2-D/3-D forcing. In other words, the injected streamwise vorticity and the resulting increased turbulent transfer did not further increase the mixing efficiency over the trends found for purely 2-D forcing.

While surprising and somewhat counter-intuitive, a similar result concerning the latter effect has been reported previously. Karasso & Mungal (1997) have recently investigated the effects of stabilizing and de-stabilizing streamwise curvature on the concentration field in mixing layers at post-mixing transition conditions. Curvature tends to produce streamwise vortical structures of the Taylor-Görtler type. Chemical product measurements were made in straight and curved shear layers; in the latter, both stable ($U_{inner} < U_{outer}$) and unstable ($U_{inner} > U_{outer}$) velocity configurations were used. They cite the work of Plesniak et al. (1994), who performed velocity measurements in both stable and unstable curved layers and found that well-organized spatially stationary streamwise vorticity was generated, which produced significant spanwise variations in the mean velocity and Reynolds stress distributions (although the source was attributed more to the amplification of small incoming disturbances than to the Taylor-Görtler instability). In addition, Plesniak et al. reported that for the unstable layer the vorticity thickness, peak streamwise vorticity and primary Reynolds stress were higher than those for the stable and straight layers. Meanwhile, the product measurements of Karasso & Mungal showed that both the mixed-fluid fraction and the average mixed-fluid concentration remained constant regardless of whether the stable, unstable or straight flow configuration was used. The experiments which are cited above suggest caution in relating the enhancement of momentum mixing with that of molecular mixing.

It is well-known (Breidenthal, 1980, Koochesfahani & Dimotakis, 1986) that the mixed-fluid fraction above the mixing transition depends on the Schmidt number, $Sc \equiv \upsilon/D$, defined as the ratio of the diffusion coefficient of momentum to that of mass. The apparent similarity between the 2-D and combined 2-D/3-D forcing in the present study may be a further effect of this parameter. Schmidt numbers for liquids are typically about three orders of magnitude larger than for gases, on account of the very low mass-diffusion coefficients for liquids. In gases, Schmidt numbers are on the order of unity, indicating comparable diffusion of mass and momentum. It appears that the small scale motions which are presumably generated due to the injected streamwise vorticity are simply not small enough to have any effect at the molecular level. A natural and interesting extension of the current work would therefore be to repeat the present experiments in a gas phase shear layer. In this regard, the effects of a variety of spanwise perturbations on the turbulent momentum transport properties have been well documented recently by Bell & Mehta (1993). They found that the introduction of an array of cylindrical pegs in the high-speed side boundary layer not only generated a regular array of counter-rotating vortex pairs but also affected the layer growth rate and turbulence properties in the far-field. Strong, although somewhat different, effects were also found when an array of vortex generators, was the source of spanwise perturbation.

What seems somewhat ironic here is that a mechanism has been found which enhances mixing efficiency, the source of which appears to lie in the two-dimensional nature of the (relatively high) forcing frequency. The contribution of the braids to the overall mixing product in liquid shear layers is generally considered to be small, the mixing being confined to a thin interface undergoing a diffusion-limited reaction, while that of the cores is significantly larger. It is speculated that by destroying the braid structures a dramatic increase in mixing takes place. This may be related to forcing at a frequency close to the subharmonic of the fundamental roll-up frequency ($f/f_o = 0.42$). The computational instability analysis of Monkewitz (1988) states that, 'the development of the subharmonic, leading eventually to pairing or *shredding*, crucially depends on its phase relation with the fundamental'. We note here that there is still a lot of room for improvement in terms of mixing enhancement - the largest value of the mixed-fluid fraction (δ_m / δ_1) which was recorded during the current experiments is approximately 0.5, i.e. on the average only about half of the shear layer width contains mixed fluid.

The 3-D perturbation does, however, have a definitive effect on the development of the shear layer. The spanwise undulations seen for the peg cases in the mixed fluid thickness, $\delta_m(z)$, the shear layer width $\delta_1(z)$, and the average mixed-fluid concentration, $\xi_M(z)$, can all be attributed to the presence of the 3-D perturbation. As a means to help visualize the types of streamwise structures generated by the peg, included in Figure 4.3.1-2 are passive scalar LIF samples from a low-speed shear layer with a peg in the *low-speed* side boundary layer. The signature of the peg is readily apparent in these images. Notice also the predominance of the middle peak of low-speed (light grey) free-stream fluid. Qualitatively, this is the result of the induced velocity from the streamwise vorticity in the legs of the horseshoe vortex generated by the peg. It is expected that the sense of this induced motion will change as the peg is moved to the high-speed side of the splitter plate. This provides a simplistic and qualitative reasoning for the 'indentations' discussed in section 4.2. It is interesting to see in Figure 4.3.2 that when 2-D forcing is applied how the number of streamwise structures increases dramatically. This reason for this will be clearer after the following description. Volumetric iso-concentration surfaces composed from these images are shown in Figure 4.3.3 and provide a perspective view of the 3-D structure of the flow.

Lasheras et al. (1986) performed an experiment in a low-speed shear layer, utilizing a chemical reaction with a pH sensitive marker to visualize the instantaneous interface between the two streams, and to analyze the origin and development of three-dimensional streamwise vorticity. They confirmed earlier findings that the layer is composed of counter-rotating pairs of streamwise vortices and stated that these structures were the result of the unstable response of the layer to 3-D perturbations in the upstream conditions. Further, they found that the streamwise vorticity was always seen to form first on the braids between consecutive spanwise structures and then to propagate into their cores. They proposed a mechanism to explain their structural observations. Their argument is modified for the present case and is schematically represented in Figure 4.3.4. The 3-D perturbation would result in a 'kink' of the axis of the primary spanwise vorticity, as shown at (a). The positive strain would then stretch the kink in the streamwise direction producing a pair of counter-rotating streamwise vortices (b). At the base of the kink the vortex lines would be lifted upward due to the influence of the streamwise vorticity. The vertical shear and/or strain would then orient the vortex axis in the axial direction, to be acted upon by the positive strain (c). This effect would continue to magnify as well as to propagate in the spanwise direction. While it is understood that the above description is necessarily an over-simplification, it is felt that the basic features of this mechanism are relevant to the present case.

It is intriguing to note that the orientation of the spanwise trends in $\xi_M(z)$ observed in the peg cases are preserved regardless of whether the 3-D disturbance is in the high-speed or low-speed boundary layer. One might expect that a mirror-image of the initial streamwise vorticity (as the peg changes sides) would be revealed as a mirror-image of the 'wiggle' in the spanwise concentration plots at each forcing frequency. The reason for the observed behavior is not yet clear.

The large reduction in span-averaged mixed-fluid concentration at $f = 16$ Hz ($x^* = 3.1$), was particularly noticeable for the case with no 3-D forcing. An explanation may be attempted solely on the basis of quasi 2-D structures. Dimotakis (1986) has related the entrainment into the shear layer to the upstream/downstream asymmetry of the large scale structure spacing. The 2-D forced layer at $x^* = 3$ has already passed through the frequency locked region $1 < x^* < 2$. This region is characterized by equally-spaced large structures. The upstream/ downstream symmetry of the large structure spacing in this region would imply a unity entrainment ratio. Because there is a delay between fluid entrainment and ultimate mixing, at some value of x^* beyond 2, the mixture concentration is expected to decrease toward that corresponding to 1:1 mixing, namely $\xi = 0.5$. While this picture may seem consistent with our results, the intriguing question is why the frequency-locked region should affect the mixture composition at all - the nearly zero growth rate in this region implies almost no additional fluid is entering the layer.

In closing, we note that it may be tempting in certain applications to use low frequency forcing ($f \ll f_0$, $x^* < 2$) to enhance the spreading rate of a shear layer in the hope of achieving better mixing. This work suggests that more efficient mixing would occur if no forcing were used at all.

Chapter 5

SIMULTANEOUS WHOLE-FIELD MEASUREMENTS OF VELOCITY AND CONCENTRATION

The previous two chapters have concentrated on measurements of the amount of mixing in a forced shear layer along with the changes in the mixed fluid composition which result from the forcing. However, the flow behavior which leads to the various mixing effects is not well understood. Since it is the structure and dynamics of the vorticity field which determine the mixing field in these flows, additional knowledge of the flow kinematics in the form of velocity and vorticity fields is needed to learn more about the dynamics of the mixing processes taking place. The subject of the present chapter is a description of a novel technique to acquire simultaneous non-intrusive velocity and concentration data over a plane in a two-stream liquid flow. Preliminary results of whole-field velocity /vorticity maps with corresponding concentration fields are presented along with point measurements of turbulent statistics such as velocity-concentration correlations. The experiments discussed below took place with the help of Mr. R. Cohn, whose assistance is gratefully acknowledged. Many of the details described here have recently been presented at the 13th U.S. National Congress of Applied Mechanics (Koochesfahani & MacKinnon, 1998).

5.1 Background

There exists an extensive body of literature on turbulent statistics in many types of flows involving mean and/or fluctuating measurements of *either* velocity components *or* scalar quantities (e.g. temperature, concentration). Studies involving *both* velocity and scalar measurements are far more limited. One of the earliest was the pioneering study by Keagy & Weller (1949). Their results in a helium jet included profiles of mean velocity using a Pitot probe and mean concentration using a sampling probe. Following a suggestion from Corrsin, Way & Libby (1970, 1971) developed a two-sensor hot-wire probe capable of monitoring fluctuations of one velocity component and of concentration in a low-speed helium jet. Antonia et al. (1975) and Chevray & Tutu (1978) produced results involving two fluctuating velocity components and temperature fluctuations using a cold-wire sensor mounted on an X-wire probe in heated air jets. More recently, the advent of optical diagnostics such as LDV, LIF and particle scattering techniques have presented new opportunities for the non-intrusive simultaneous acquisition of multiple flow variables. Owen (1976) used a combination of LDV and LIF to measure velocity and concentration correlations in a co-axial liquid jet. Stårner (1983) and Dibble & Schefer (1983) acquired velocity, density, and species concentration via LDV/Mie scattering and LDV/Raman scattering, respectively, in a diffusion flame. Such works have led to important information on velocity/scalar correlations for modeling in the Reynolds averaged conservation equations. All of the above investigations, however, have incorporated single point measurements. One of very few studies involving simultaneous planar measurements is that of Frank, Lyons & Long (1996), who have combined particle-image velocimetry (PIV) and LIF to record two velocity components as well as concentration in gas-phase flows. The present work monitors two components of velocity and concentration in liquid-phase flows. It's advantage stems from the fact that, in contrast to all of the above non-intrusive techniques, the use of seeding particles is not required. Seed particles have the potential to contaminate either the velocity (e.g. out of plane motion) or the concentration measurements or to lose neutral buoyancy (in reacting flows).

5.2 Experimental Technique

The shear layer facility used for the mixing measurements was also used for the simultaneous velocity/concentration measurements. As before, the free-stream speeds were set to $U_1 \approx 40$ cm/s and $U_2 \approx 20$ cm/s, and the same forcing frequencies were used. The procedure for the simultaneous measurement is a combination of two non-intrusive techniques - molecular tagging velocimetry (MTV) for the velocity data and laser-induced fluorescence (LIF) for the concentration data. For a detailed description of various MTV approaches including the one used here the reader is referred to Koochesfahani et al. (1996), Gendrich et al. (1997). Briefly, the MTV procedure used is as follows.

A three component phosphorescent compound (1-BrNp • Gβ-CD • ROH) is premixed in the entire shear layer facility. Details of this complex may be found in Ponce et al. (1993). The molecules of the triplex become long lifetime tracers (e^{-1} lifetime ≈ 4 ms) when excited ('tagged') by photons. The source of the excitation is a pulsed laser (Lambda Physik LPX 220i, wavelength 308 nm), which is used to tag the regions of interest. The laser beam is converted via a beam-splitter, mirrors and 'beam-blockers' into a two-dimensional grid of thin laser lines. An example of the resulting tagged grid is shown in Figure 5.2.1(a). An initial image of the grid is recorded at time $t = t_o$, just after the laser fires. The tagged molecules comprising the laser grid are then convected by the flow. A short time (Δt) later, within the lifetime of the tracer, the phosphorescent luminescence from the grid is recorded by a second camera. A sample of a distorted grid is shown in Figure 5.2.1(b). Using a spatial correlation technique, for each intersection point of the grid the displacement between its initial and final locations is computed. Knowing the time between images allows the resulting two-dimensional displacement field to be converted to a velocity field. Two cameras, triggered Δt apart, are used to acquire the initial and displaced images of the grid. The two camera system is adopted to minimize the effects of variations in the initial grid pattern (e.g. laser beam pointing instability, vibration of the optics, etc.) which would be misinterpreted as flow velocity fluctuations.

The concentration measurement is facilitated by premixing a solution of fluorescein with the reservoir fluid of *only one* of the free-streams, as in the LIF method discussed earlier. Both reservoirs have the phosphorescent triplex premixed to enable velocity measurements over the whole field of view. The fluorescence intensity field at $t = t_o$ gives the concentration field. This is recorded by a third camera viewing the opposite side of the test-section from the MTV cameras. A schematic of the set-up is shown in Figure 5.2.2.

The issue of cross-talk between the MTV and LIF signals is a relevant one, but can be shown to be almost negligible. Consider the two emission spectra in Figure 5.2.3. In part (a) of this figure the fluorescence and phosphorescence emissions of the MTV triplex are shown to occur over the approximate ranges 300-400 nm and 460-700 nm, respectively. Part (b) shows that the fluorescein emission occurs above about 490 nm. We first consider the effect of the MTV signal on the LIF measurement. It is clear that the fluorescence emission of the MTV triplex is spectrally well separated from that of the fluorescein and can easily be filtered out. We note here that the quantum efficiency of the triplex phosphorescence ϕ_e = 0.035, about 1/30th that of the fluorescence of the fluorescein. Thus the triplex phosphorescence is easily dominated by the LIF signal. The effect of the relatively weak phosphorescence emission can be reduced to negligible levels by reducing the exposure of the LIF detector (1 μs in the present case). Further, the triplex compound does not absorb and re-emit fluorescein's emission. As for the effect of the LIF signal on the MTV measurement - the fluorescence emission from fluorescein decays to near zero levels well before the pair of MTV images are acquired. A timing chart is sketched in Figure 5.2.4 and shows the relative positions of the laser pulse and the triggering of the three cameras.

For the work described here two types of data were acquired:

1) a low density grid (i.e. thick grid lines spaced relatively far apart) was used for the actual combined MTV/LIF measurements, and

2) a relatively high density of laser grid lines was used to acquire purely velocimetry data.

It was felt that the thicker grid lines of the lower density grid would provide better flow visualization with which to compare the MTV vorticity fields, and also reduce potential errors in the concentration field due to laser pointing variations. This, of course, leads to a trade-off in spatial resolution. However, in future experiments it is expected that the spatial resolution will be increased significantly. A sample of the three images required for a combined MTV/LIF measurement is shown in Figure 5.2.5. The top image show the concentration field due to the fluorescein acquired by the LIF camera. The lower two images display the initial laser grid pattern due to the MTV triplex and it's subsequent distortion Δt later acquired by the two MTV cameras.

5.3 Preliminary Results

The following results have been extracted from the first application of the combined

MTV/LIF procedure. As noted above, the study is still somewhat exploratory in nature in the sense that certain parameters remain to be optimized (e.g. spatial resolution, LIF exposure, laser beam pointing stability). However, it is believed that the results obtained demonstrate that the technique is capable of producing quantitative two-dimensional concentration/vorticity fields as well as turbulent statistics such as velocity-scalar Reynolds fluxes.

The first three figures (5.3.1-5.3.3) provide examples of the combined two-component velocity measurements and concentration in a shear layer with no forcing, and forcing at $f = 4$ Hz and $f = 8$ Hz, respectively. These figures display the concentration field (upper image) aligned horizontally with the velocity field/vorticity contours (lower image). The mean convection speed has been subtracted from the velocity field. Stagnation points are seen between adjoining large structures and the regions of vortical motion inferred by the concentration measurements appear to closely track the vorticity field from the MTV measurements.

Next some turbulence point statistics are presented from the high-density grid data. While such data are available at many grid intersections, only transverse profiles at a single x-location ($x \approx 15.5$ cm) near the mid-point of the grid are reported here. Figures 5.3.4-6 show the present data of maximum normalized u_{rms}, v_{rms}, and $-\overline{u'v'}$ versus Re_{δ_ω} along with data compiled from the literature on unforced plane shear layers. In each case the present datum point falls within the scatter of the existing data, and provides some initial validation of the velocity measurements. Profiles of the mean streamwise velocity plotted using similarity coordinates are shown in Figure 5.3.7, where $U_c = (U_1+U_2)/2$ is the mean free-stream speed and y_c is the transverse co-ordinate at which this value occurs in the mean profiles. An increase in the shear layer width, $\delta_{\omega,}$ at *f* = 4 Hz is clearly seen relative to the unforced case. The width at *f* = 8 Hz appears to be very similar to that of the unforced layer. We note that it remains to be shown how δ_1 varies with δ_ω in forced shear layers. The present technique is capable of providing such information. Profiles of the Reynolds stress $-\overline{u'v'}$ are plotted in figure 5.3.8. The familiar bell-shaped profile is seen in the unforced case, while the *f* = 4 Hz case shows much larger intensities, indicative of more organized motions. The Reynolds stress intensity drops significantly at *f* = 8 Hz. Oster & Wygnanski (1982) show a qualitatively similar drop with streamwise distance at a fixed frequency in one of their plots. The average concentration and its rms variation in the y-direction are shown in Figure 5.3.9-10. The mean concentration at *f* = 8 Hz case shows a flat region in the middle of the layer consistent with flow visualizations indicating the passage of structures in the frequency-locked x^* regime with fairly well-mixed cores. The rms concentration profiles have a double-humped nature indicating greater variation at the edges of the shear layer. The streamwise and lateral velocity-concentration Reynolds fluxes $\overline{u'\xi'}$ and $\overline{v'\xi'}$ are shown in Figures 5.3.11-12. Unfortunately we have not found this type of data for shear layers in the literature, and therefore quantitative comparisons cannot be made. However, qualitative arguments may be made for the signs of the correlations.

It is evident that the simultaneous application of both the MTV and LIF techniques yields more information than each separately. The non-intrusive combined measurement of the two-dimensional velocity/vorticity field along with the concentration field and structural information is expected to be a useful tool in flow studies concerned with mixing and mixing enhancement.

CONCLUSIONS

Chemically reacting and passive scalar measurements of the structure and mixing field were performed in a turbulent two stream mixing layer undergoing 2-D and combined 2-D/3-D perturbations. The majority of the work presented has focused on quantifying the amount of molecular mixing and the mixture composition as a function of the dimensionless variable $x^* = \lambda x f / U_c$, which was varied by changing the frequency at a fixed downstream location, near the end of the mixing transition. Both streamwise and spanwise measurements were made. A summary of the main conclusions is as follows.

- When 2-D forcing is applied, the amount of molecular mixing, quantified by the mixed-fluid thickness, δ_m, increases by varying degrees relative to that of the unforced layer at all frequencies and amplitudes used.

- If the mixing efficiency is defined as the fraction of the layer occupied by mixed fluid, i.e. the mixed-fluid fraction, δ_m/δ_1, results indicate that mixing efficiency is increased only for $x^* \geq 2$. A peak is reached at some point beyond $x^* = 2$, but mixing enhancement appears to continue until at least $x^* = 6$. It is speculated that the destruction of the braid regions connecting the large spanwise structures is responsible for the increase in mixing efficiency. This may be a related to forcing at a frequency close to the subharmonic. An important result is that below $x^* = 2$, the mixing efficiency is decreased relative to the unforced case. Thus low frequency (*f*

<<f_o) forcing is not recommended if enhanced mixing efficiency is a goal.

- The mixture composition also was affected by 2-D forcing. While there was little variation between the other cases, at $x^* = 3.1$, the span-averaged mixed-fluid concentration, $\overline{\xi_M}$, decreased to approximately 0.5, suggesting a significant modification to the entrainment and mixing process. This value indicates a 1:1 mixture ratio of high-speed to low-speed fluid, more characteristic of a wake flow with equal speeds rather than a shear layer with one stream twice the speed of the other.

- The 3-D perturbations caused a spanwise undulation in the mean mixed-fluid concentration, $\xi_M(z)$. The nature of the 'wiggle' was the same for the cases of no 2-D forcing, $f = 4$, 8 and 32 Hz. At $f = 16$ Hz the nature of the wiggle reversed, for reasons which are still unclear. Interestingly, the character of these wiggles was preserved regardless of whether the source of the 3-D forcing was on the high- or low-speed side of the splitter plate.

- While the span-average mixed-fluid concentrations, $\overline{\xi_M}$, for the majority of cases with 3-D forcing were unchanged or showed slight increases relative to their 'unforced' cases, a tendency towards lower values was found at $x^* = 3.1$.

- The presence of a 3-D disturbance in either of the boundary layers of the splitter plate also caused undulations of the amount of mixed fluid and the layer width. Somewhat surprisingly the trends of the mixed-fluid fraction versus x^* did not change compared to that for purely 2-D forcing. That is, the presence of the 3-D perturbation did not further increase the mixing efficiency over levels for purely 2-D forcing.

- It is often speculated that increased three-dimensional motions should lead to an increase in interfacial surface area and hence yield enhanced mixing efficiency. This is not borne out by the present work and may be a reflection of the Schmidt number in the current liquid phase experiments. This result has potential ramifications in liquid applications where increased mixing enhancement is sought through the use of streamwise vorticity injection mechanisms. Further study is needed in this area, in particular a repeat of the current work in gas phase flows would be highly illustrative.

- A novel technique has been presented for the simultaneous non-intrusive measurement of two velocity components and concentration in a plane, along with preliminary results. It is expected that this approach will be a useful tool in flow studies concerned with mixing and mixing enhancement.

APPENDIX

1. Bleaching of the Dye

Continuous exposure to an excitation source results in a loss of absorption efficiency of the fluorescein dye due to a process known as photo-bleaching. Bleached dye molecules do not absorb the laser light, the effect of which is an apparent reduction in dye concentration. The number of absorbing dye molecules decays exponentially in time as (Koochesfahani, 1984)

$$n = n_o e^{-t/\tau_b}$$

where n_o is the number of molecules absorbing at time $t = 0$, n is the number of molecules absorbing at time t, and τ_b is the bleaching time constant. τ_b is a function of the dye used, the laser photon flux (the number of photons per unit area per unit time), and the dye absorption cross section. Koochesfahani (1984) calculated a value of $\tau_b \approx 20$ s for his experiments, indicating that only 37% of the dye molecules would still be absorbing after 20 seconds. Thus bleaching effects can be very significant.

However, the problem of bleaching is greatly reduced in flowing systems. If the dye-bearing fluid passes through the laser sheet in a time much less than τ_b bleaching becomes negligible. The titration reference chamber is more sensitive to bleaching because the same fluid remains in the chamber throughout the experiment. Bleaching is reduced, though, by continuously circulating the fluid and by making the volume of fluid covered by the laser sheet much smaller than the total volume of the chamber. To minimize bleaching effects further, the intensity of the chamber near the *start* of each experiment was used as the normalization constant $(I_f)_{\max}$.

2. Free Stream Intensity Elimination

Ideally, the fluorescent intensities in both free streams are zero. In reality the free-stream which carries the acid/dye solution has nonzero intensity. Typically, values of about 4-8 counts were recorded in the acid/dye stream compared with $(I_f)_{\max} \approx 200$. Although these values are small, they cannot be neglected and measures were taken to effectively 'filter' out the acid/dye free-stream contribution to δ_{P1} and δ_{P2}.

From an acquired image sequence it is straightforward to identify the acid/dye free-stream intensity values present. Once the maximum value has been determined, one possible method to eliminate the free stream contribution is simply to threshold all intensities at or below this value to zero in each image of the sequence. This method is limited by the fact that it may eliminate the contribution of some real phenomena. Nelson (1996) improved upon this technique in the following way. Each column in each image was read and processed separately by the computer. When the intensity along the column fell below the free stream value *for a specified number of consecutive rows* the intensities were set to zero. This method reduces the possibility of actual product being filtered out. The filtering process will identify the nonzero intensity contribution from the acid/dye stream and set these intensities to zero.

The number of consecutive rows, γ, needed before intensities were set to zero had to be determined before processing. Setting γ too low may result in eliminating real features, while setting γ too high can allow some free-stream intensity to remain unfiltered. However, Nelson (1996) has demonstrated that for highly mixed flows, such as those in the present experiments, the product thickness is almost totally insensitive to changes in γ.

REFERENCES

ANTONIA, R. A., PRABHU, A. & STEPHENSON, S. E. 1975
Conditionally sampled measurements in a heated turbulent jet.
J. Fluid Mech. **72**, 455-480.

BALINT, J. L. & WALLACE, J. M. 1989
The statistical properties of the vorticity field of a two-stream turbulent mixing layer.
Advances in Turbulence 2, Springer-Verlag, 74-78.

BELL, J. H. & MEHTA, R. D. 1990
Interaction of a streamwise vortex with a turbulent mixing layer.
Phys. Fluids A **2(11)**, 2011-2023.

BELL, J. H. & MEHTA, R. D. 1993
Effects of imposed spanwise perturbations on plane mixing-layer structure..
J. Fluid Mech. **257**, 33-63.

BERNAL, L. P. 1981
The coherent structure of turbulent mixing layers.
PhD thesis, California Institute of Technology, Pasadena, CA.

BREIDENTHAL, R. E. 1978
A chemically reacting turbulent shear layer.
PhD thesis, California Institute of Technology, Pasadena, CA.

BREIDENTHAL, R. E. 1980
Response of plane shear layers and wakes to strong three-dimensional disturbances.
Phys. Fluids **23(10)**, 1929-1934.

BREIDENTHAL, R. E. 1981
Structure in turbulent mixing layers and wakes using a chemical reaction.
J. Fluid Mech. **109**, 1-24.

BROWAND, F. K. 1966
An experimental investigation of the instability of an incompressible, separated shear layer.
J. Fluid Mech. **26**, 281-307.

BROWAND, F. K. & HO, C. M. 1983
The mixing layer: an example of quasi two-dimensional turbulence.
J. de Mécanique Théorique et Appliquée Numéro Spécial, 99-120.

BROWAND, F. K. & WEIDMAN, P. D. 1976
Large scales in the developing mixing layer.
J. Fluid Mech. **76**, 127-144.

BROWN, G. L. & ROSHKO, A. 1971
The effect of density difference on the turbulent mixing layer.
Turbulent Shear Flows, AGARD-CP-93, 23.1-23.12.

BROWN, G. L. & ROSHKO, A. 1974
On density effects and large structure in turbulent mixing layers.
J. Fluid Mech. **64**, 775-816.

CHEVRAY, R. & TUTU, N. K. 1978
Intermittency and preferential transport of heat in a round jet.
J. Fluid Mech. **88**, 133-160.

DIBBLE, R. W. & SCHEFER, R. W. 1983
Simultaneous measurement of velocity and scalars in a turbulent non-premixed flame by combined laser Doppler velocimetry and laser Raman scattering.
Turbulent Shear Flows 4: 4th Intl. Symp. Turbulent Shear Flows, Karlsruhe, Germany, September 12-14, pp. 319-327.

DIMOTAKIS, P. E. 1986
Two dimensional shear layer entrainment.
AIAA J. **24(11)**, 1791-1796.

DIMOTAKIS, P. E., & BROWN, G. L. 1976
The mixing layer at high Reynolds number : large-structure dynamics and entrainment.
J. Fluid Mech. **78**, 535-560.

FOSS, J. F. & HAW, R. C. 1990
Vorticity and velocity measurements in a 2:1 mixing layer.
Forum on Turbulent Flows, **94**, 115-120.

FOSS, J. F. & WALLACE, J. M. 1989
The measurement of vorticity in transitional and fully developed turbulent flows.
Advances in Fluid Mechanics Measurements (ed. M. Gad-el-Hak).
Lecture Notes in Engineering, **45**. Springer-Verlag.

FRANK, J. H., LYONS, K. M. & LONG, M. B. 1996
Simultaneous scalar / velocity field measurements in turbulent gas-phase flows.
Combustion and Flame **107**, 1-12.

FREYMUTH, P. 1966
On transition in a separated laminar boundary layer.
J. Fluid Mech. **25**, 683-704.

GENDRICH, C. P., KOOCHESFAHANI, M. M. & NOCERA, D. G. 1997
Molecular tagging velocimetry and other novel applications of a new phosphorescent supramolecule.
Experiments in Fluids **23**, 361-372.

HERNAN, M. A. & JIMENEZ, J. 1982
Computer analysis of a high-speed film of the plane turbulent mixing layer.
J. Fluid Mech. **119**, 323-345.

HO, C. M. & HUANG, L. S. 1982
Subharmonics and vortex merging in mixing layers.
J. Fluid Mech. **119**, 443-473.

HO, C. M. & HUERRE, P. 1984
Perturbed free shear layers.
Ann. Rev. Fluid Mech. **16**, 365-424.

HUANG, L. S. & HO, C. M. 1990
Small-scale transition in a plane mixing layer.
J. Fluid Mech. **210**, 475-500.

JIMENEZ, J., MARTINEZ-VAL, R. & REBOLLO, M. 1979
On the origin and evolution of three-dimensional effects in the mixing layer.
Final Report DA-ERO 79-G-079, Universidad Politecnica de Madrid, Spain.

KARASSO, P. S. & MUNGAL, M. G. 1996
Scalar mixing and reaction in plane liquid shear layers.
J. Fluid Mech. **323**, 23-63.

KARASSO, P. S. & MUNGAL, M. G. 1997
Mixing and reaction in curved liquid shear layers.
J. Fluid Mech. **334**, 381-409.

KATCH, G. J. & KOOCHESFAHANI, M. M. 1993
Mixing of species in a two-stream shear layer forced by an oscillating airfoil.
AIAA paper 93-0444; also KATCH, G. J. 1994 M.S. Thesis, Michigan State University.

KONRAD, J. H. 1976
An experimental investigation of mixing in two-dimensional turbulent shear flows with applications to diffusion-limited chemical reactions.
PhD thesis, California Institute of Technology, Pasadena, CA; and *Project SQUID Technical Report* CIT-8-PU.

KOOCHESFAHANI, M. M 1984
Experiments on turbulent mixing and chemical reactions in a liquid mixing layer.
PhD thesis, California Institute of Technology, Pasadena, CA.

KOOCHESFAHANI, M. M., COHN, R. K., GENDRICH, C.P. & NOCERA, D .G. 1996
Molecular tagging diagnostics for the study of kinematics and mixing in liquid phase flows. Presented at the *Plenary Session of the Eighth International Symposium on Applications of Laser Techniques to Fluid Mechanics, Lisbon, Portugal, July 8-11.*

KOOCHESFAHANI, M. M. & DIMOTAKIS, P. E. 1986
Mixing and chemical reactions in a turbulent liquid mixing layer.
J. Fluid Mech. **170**, 83-112.

KOOCHESFAHANI, M. M. & DIMOTAKIS, P. E. 1989
Effects of a downstream disturbance on the structure of a turbulent plane mixing layer.
AIAA J. **27(2)**, 161-166.

KOOCHESFAHANI, M. M. & MACKINNON, C. G. 1991
Influence of forcing on the composition of mixed fluid in a two-stream shear layer.
Phys. Fluids A **3(5)**, 1135-1142.

KOOCHESFAHANI, M. M. & MACKINNON, C. G. 1998
Methods for simultaneous velocity/passive scalar measurements using molecular tagging diagnostics. Presented at the *13th U.S. National Congress of Applied Mechanics, Gainesville, Florida, June 21-26.*

LANG, D. B. 1985
Laser Doppler velocity and vorticity measurements in turbulent shear layers.
PhD thesis, California Institute of Technology, Pasadena, CA.

LASHERAS, J. C., CHO, J. S. & MAXWORTHY, T. 1986
On the origin and evolution of streamwise vortical structures in a plane, free shear layer.
J. Fluid Mech. **172**, 231-258.

LASHERAS, J. C., CHOI, H. 1988
Three-dimensional instability of a plane, free shear layer: an experimental study of the formation and evolution of streamwise vortices.
J. Fluid Mech. **189**, 53-86.

MACKINNON, C. G. 1991
Influence of forcing on the composition of mixed-fluid in a two-stream shear layer.
M.S. Thesis, Michigan State University.

MACKINNON, C. G. & KOOCHESFAHANI, M. M. 1994
Effects of 2-D and 3-D disturbances on mixing in a shear layer.
Bull. Am. Phys. Soc. **39(6)**, 1846.

MICHALKE, A. 1965
On spatially growing disturbances in an inviscid shear layer.
J. Fluid Mech. **23**, 521-544.

MIKSAD, R.W. 1972
Experiments on the nonlinear stages of free shear layer transition.
J. Fluid Mech. **56**, 695-719.

MOSER, R. D. & ROGERS, M. M 1990
Mixing transition and the cascade to small scales in a plane mixing layer.
Proc. of IUTAM Symposium Stirring and Mixing, La Jolla, California, August 20-24.

MONKEWITZ, P. A. 1988
Subharmonic resonance, pairing and shredding in the mixing layer.
J. Fluid Mech. **188**, 223-252.

NELSON, K. E. 1996
Structure and mixing in a low Reynolds number forced wake in a confining channel.
M.S. Thesis, Michigan State University.

NYGAARD, K. J. & GLEZER, A. 1991
Evolution of streamwise vortices and generation of small-scale motion in a plane mixing layer.
J. Fluid Mech. **231**, 257-301.

OSTER, D. & WYGNANSKI, I. 1982
The forced mixing layer between parallel streams.
J. Fluid Mech. **123**, 91-130.

OWEN, F. K. 1976
Simultaneous laser measurements of instantaneous velocity and concentration in turbulent mixing flows.
Proc. AGARD Conf. On Applications of Non-Intrusive Instrumentation in Fluid Flow Research, **AGARD-CP-193**.

PLESNIAK, M. W., MEHTA, R. D. & JOHNSTON, J. P. 1994
Curved two-stream turbulent mixing layers: three-dimensional structure and streamwise evolution.
J. Fluid Mech. **270**, 1.

PONCE, A., WONG, P. A., WAY, J. J. & NOCERA, D. G. 1993
Intense phosphorescence triggered by alcohols upon formation of a cyclodextrin ternary complex.
J. Phys. Chem. **97**, 11137.

REBOLLO, M. 1973
Analytical and experimental investigation of a turbulent mixing layer of different gases in a pressure gradient.
PhD thesis, California Institute of Technology, Pasadena, CA.

ROBERTS, F. A. 1985
Effects of a periodic disturbance on structure and mixing in turbulent shear layers and wakes.
PhD thesis, California Institute of Technology, Pasadena, CA.

ROSHKO, A. 1990
The mixing transition in free shear flows.
Proc. NATO Advance Research Workshop on THE GLOBAL GEOMETRY OF TURBULENCE
(Impact of nonlinear dynamics), Rota (Cádiz), Spain, July 8-14.

STÅRNER, S. H. 1983
Joint measurement of radial velocity and scalars in a turbulent diffusion flame.
Combust. Sci. Technol. **30**, 145-169.

WAY, J. & LIBBY, P. A. 1970
Hot-Wire probes for measuring velocity and concentration in helium and air mixture.
AIAA J. **8**, 976-978.

WAY, J. & LIBBY, P. A. 1971
Application of Hot-Wire Anemometry and Digital Techniques to Measurements in a Turbulent Helium Jet.
AIAA J. **9**, 1567-1573.

WINANT, C. D. & BROWAND, F. K. 1974
Vortex pairing : the mechanism of turbulent mixing layer growth at moderate Reynolds number.
J. Fluid Mech. **63**, 237-255.

WYGNANSKI, I., OSTER, D., FIEDLER, H. & DZIOMBA, B. 1979
On the perseverence of a quasi-two-dimensional eddy-structure in a turbulent mixing layer.
J. Fluid Mech. **92**, 1-16.

ZAMAN, K. B. M. Q. & HUSSAIN, A. K. M. F. 1981
Turbulence suppression in free shear flows by controlled excitation.
J. Fluid Mech. **103**, 133-159.

ZHANG, S. & SCHNEIDER, S. P. 1995
Quantitative molecular-mixing measurements in a round jet with tabs.
Phys. Fluids **7(5)**, 1063-1070.

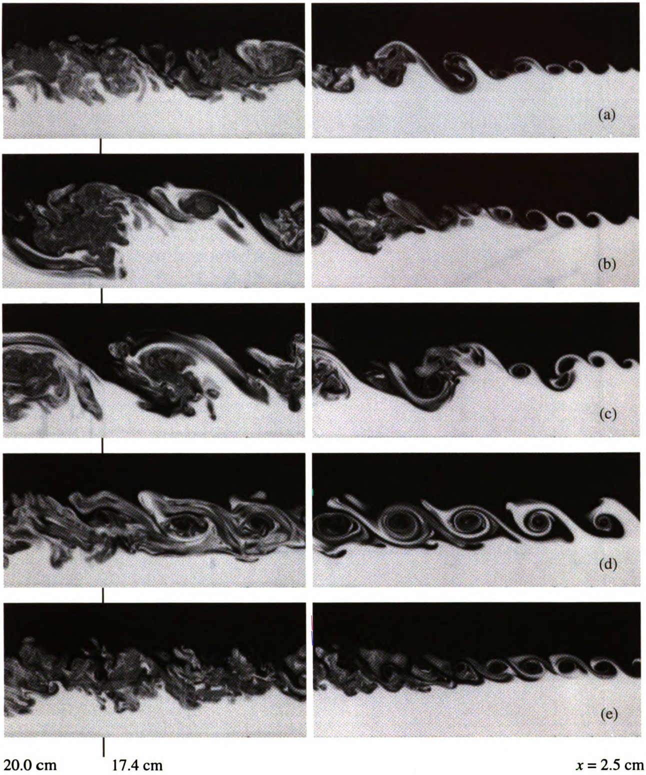

Figure 3.1.1. Streamwise flow structure and passive scalar concentration field for (a) no 2-D forcing, (b) $f = 4$ Hz, (c) $f = 8$ Hz, (d) $f = 16$ Hz, (e) $f = 32$ Hz; mid-amplitude, no 3-D forcing.

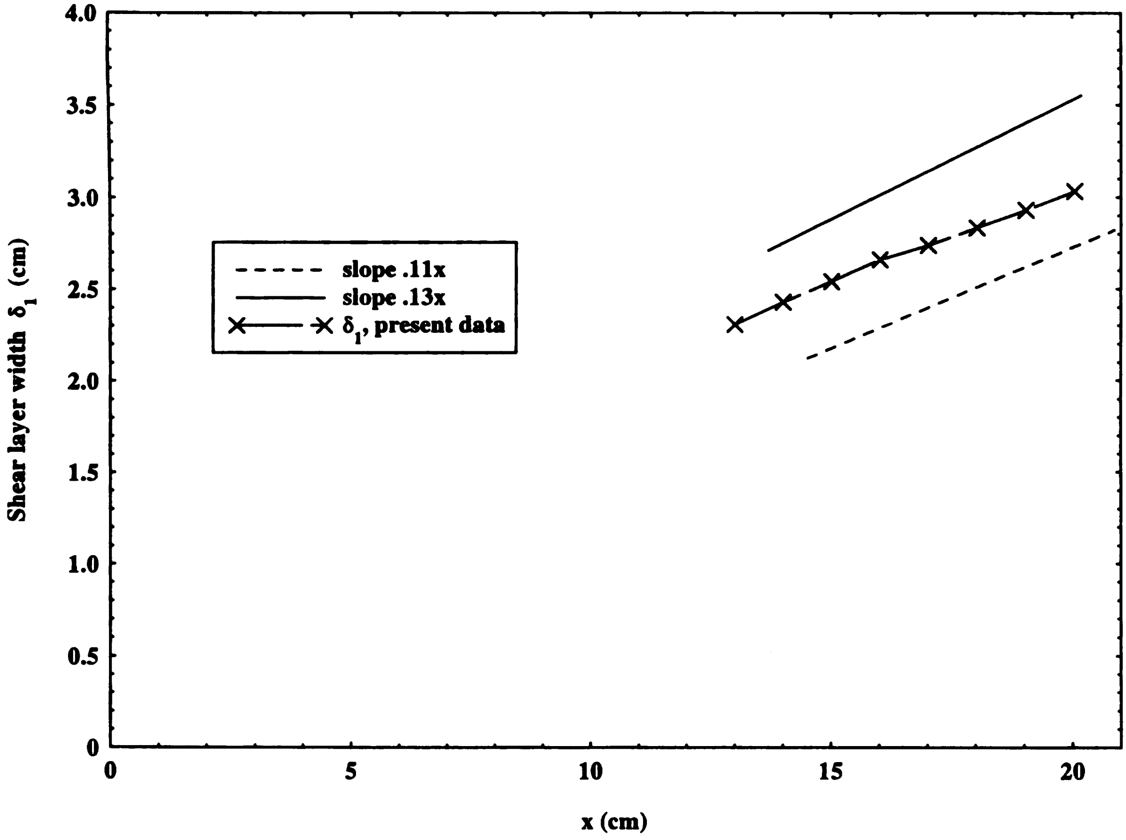

Figure 3.1.2. Unforced shear layer width versus *x*.

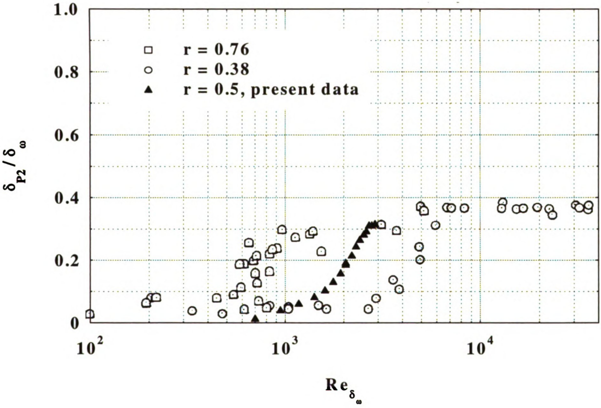

Figure 3.1.3. Comparison of mixing transition with Breidenthal.

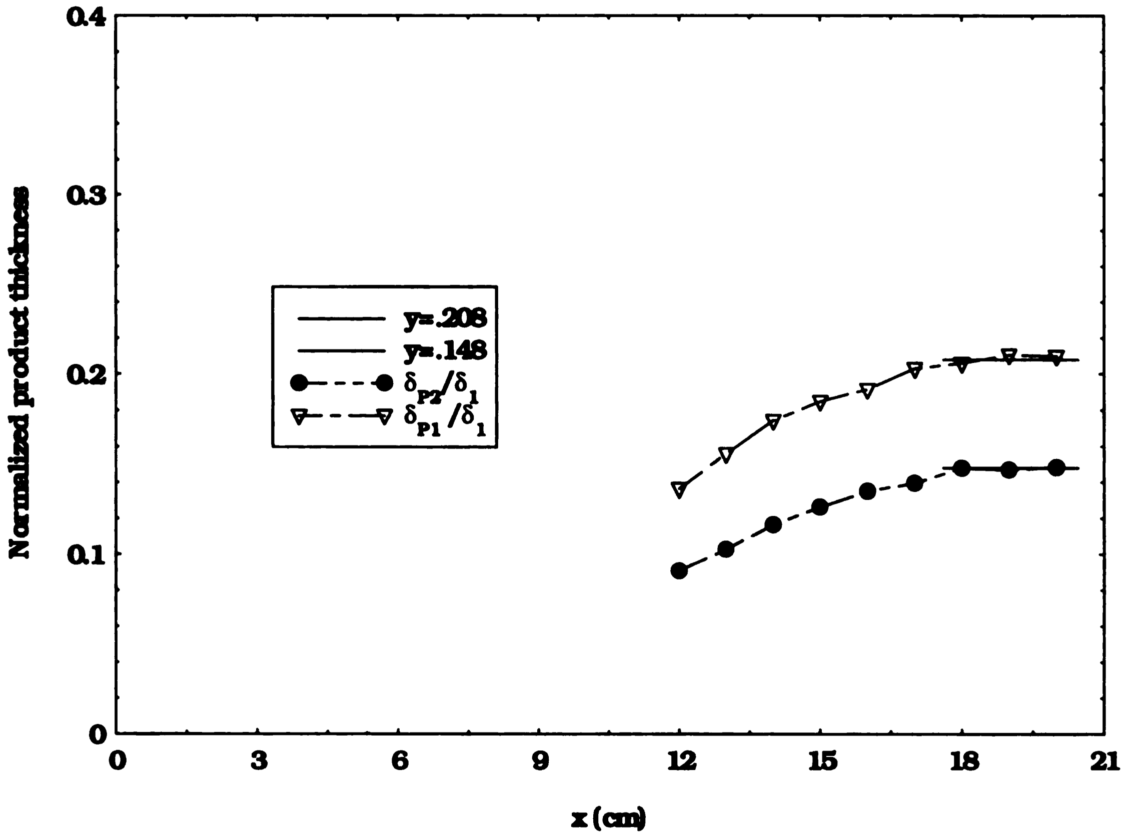

Figure 3.1.4. Normalized product thicknesses versus x.

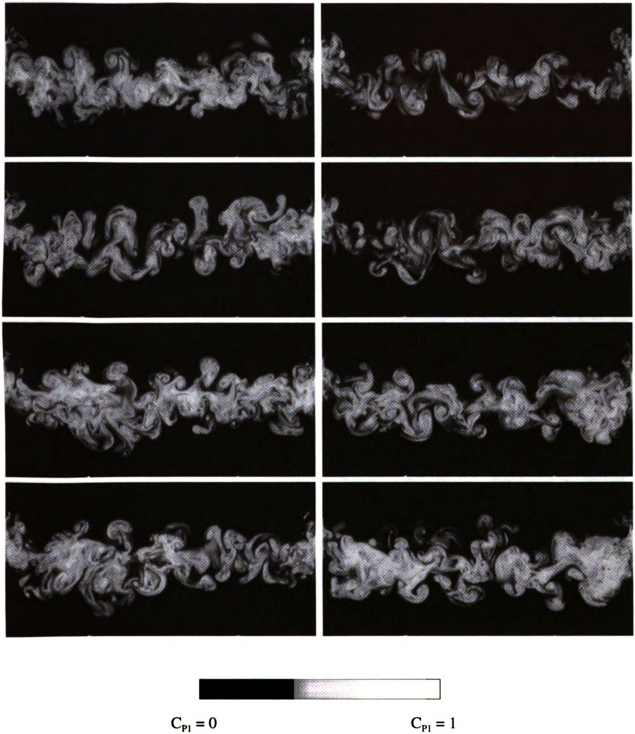

Figure 3.2.1. Spanwise flow structure and product concentration field with no 2-D forcing.

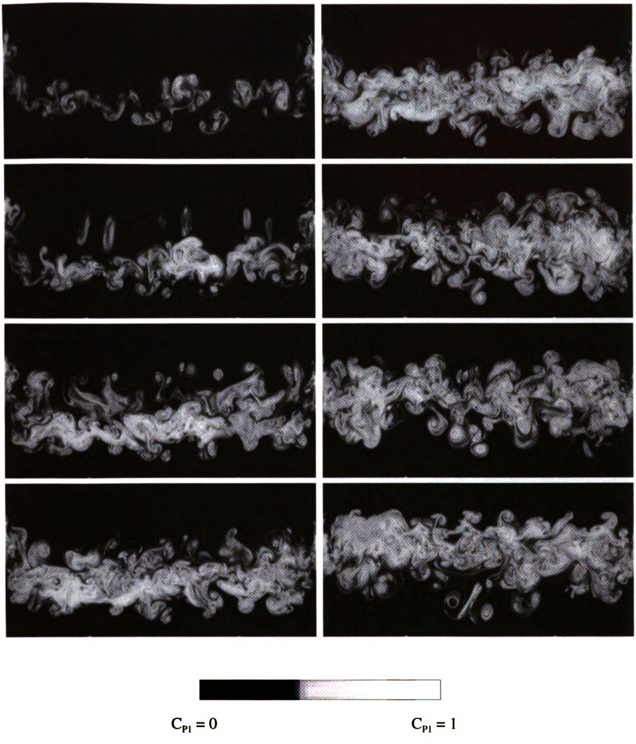

Figure 3.2.2. Spanwise flow structure and product concentration field with 2-D forcing; $f = 4$ Hz, $x^* = 0.77$, $f/f_o = 0.11$.

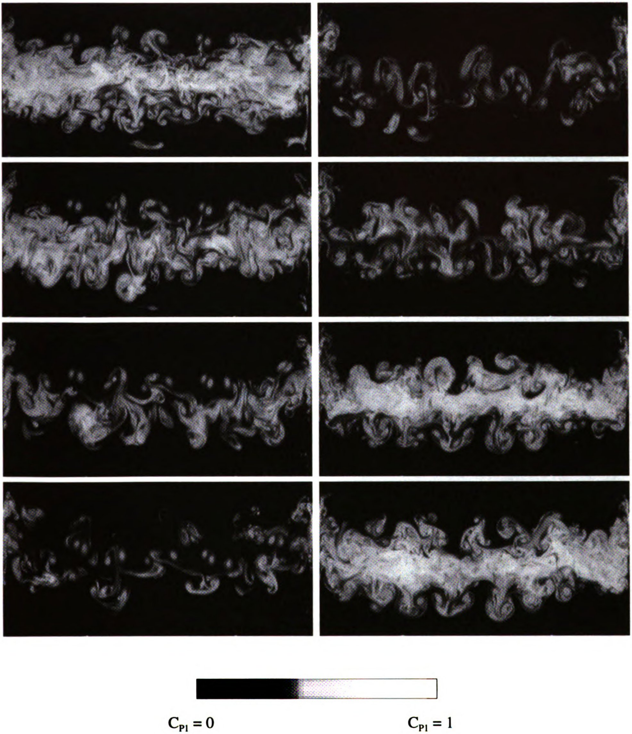

Figure 3.2.3. Spanwise flow structure and product concentration field with 2-D forcing; $f = 8$ Hz, $x^* = 1.55$, $f/f_o = 0.21$.

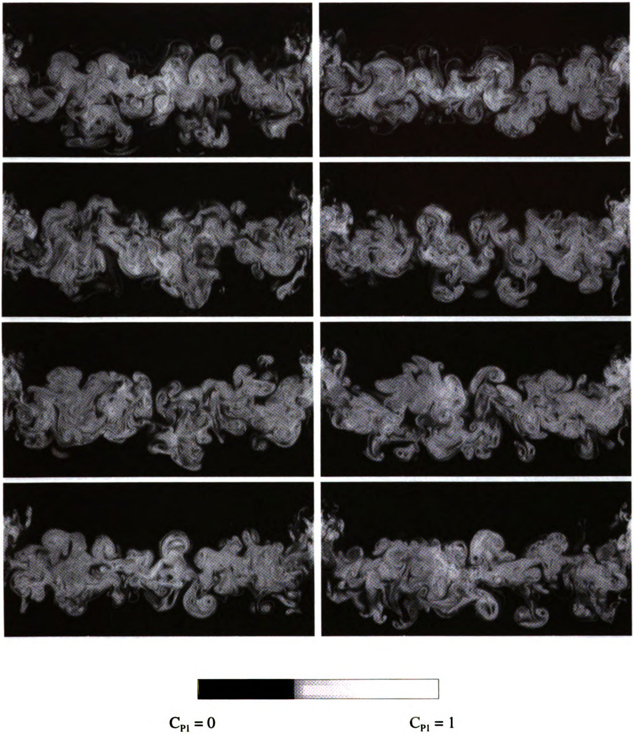

Figure 3.2.4. Spanwise flow structure and product concentration field with 2-D forcing; $f = 16$ Hz, $x^* = 3.1$, $f/f_o = 0.42$.

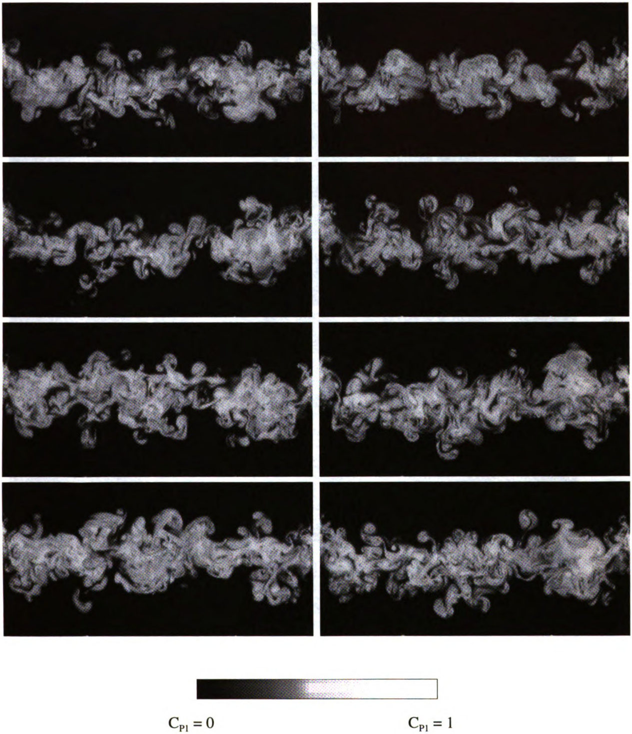

Figure 3.2.5. Spanwise flow structure and product concentration field with 2-D forcing; $f = 32$ Hz, $x^* = 6.2$, $f/f_o = 0.84$.

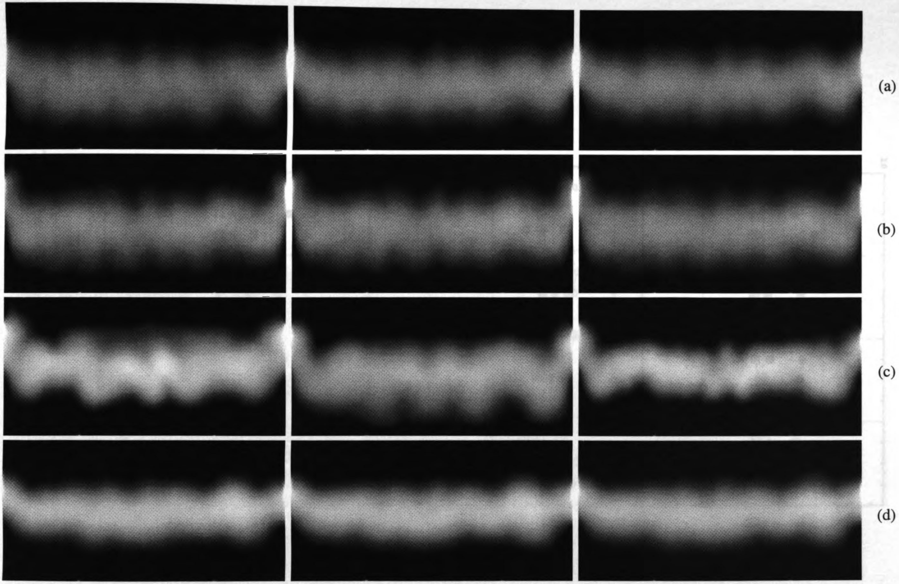

Figure 3.2.6. Average product concentration spanwise images for (a) $f = 4$ Hz, (b) $f = 8$ Hz, (c) $f = 16$ Hz, (d) $f = 32$ Hz; no 3-D forcing.

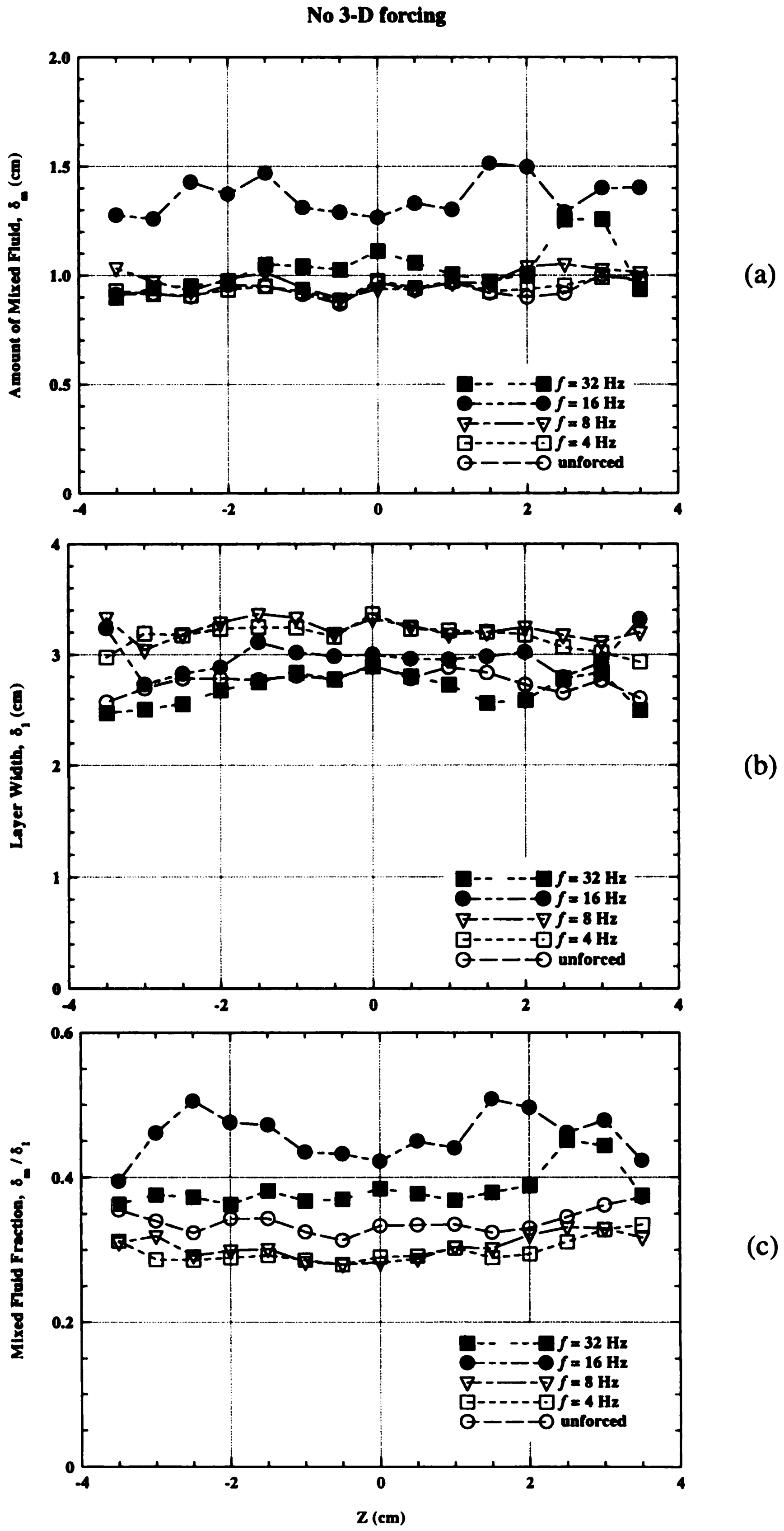

Figure 3.2.7. Calculated quantities versus z at x=17.4 cm; no 3-D forcing.

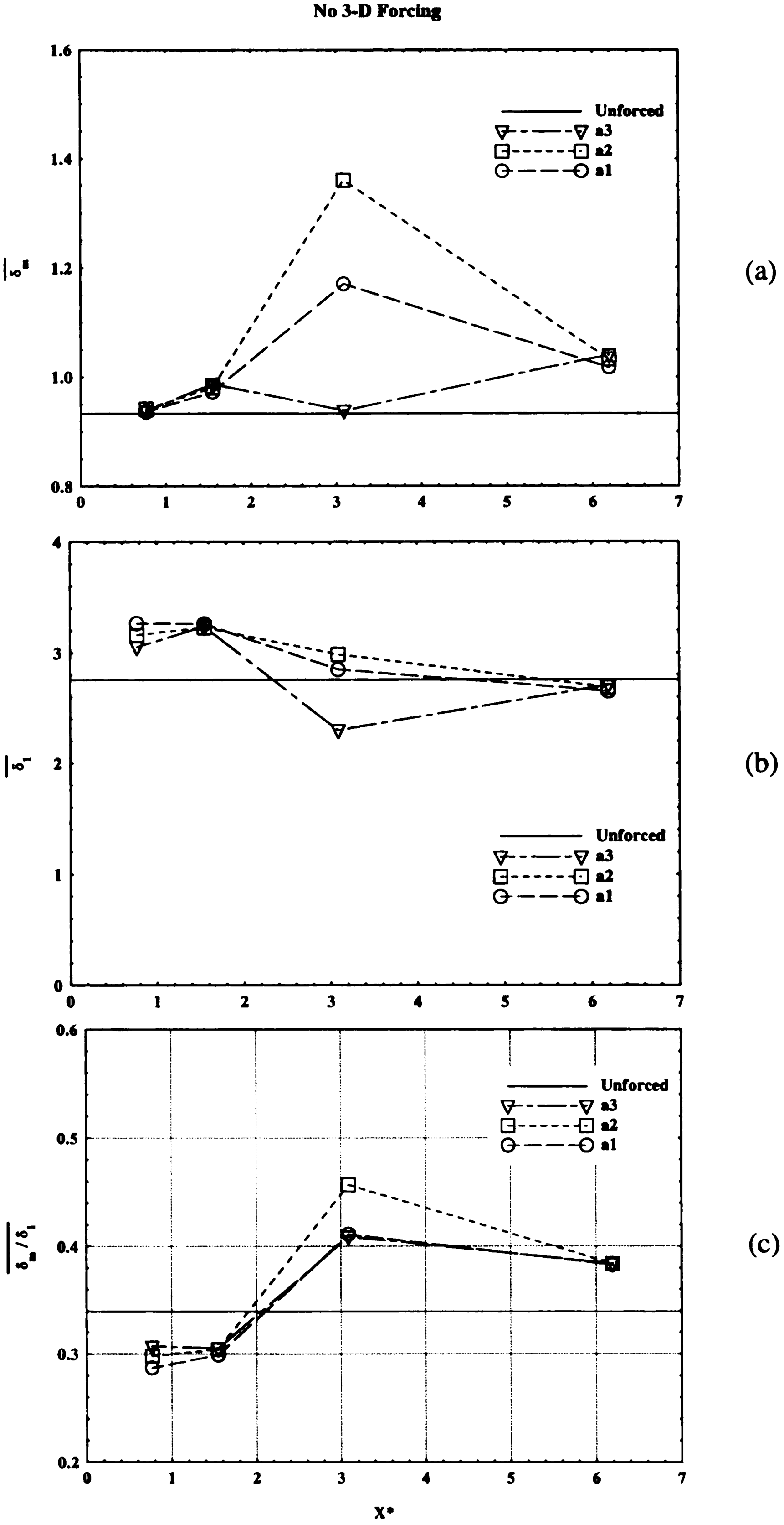

Figure 3.2.8. Span-averaged quantities versus x^*; no 3-D forcing.

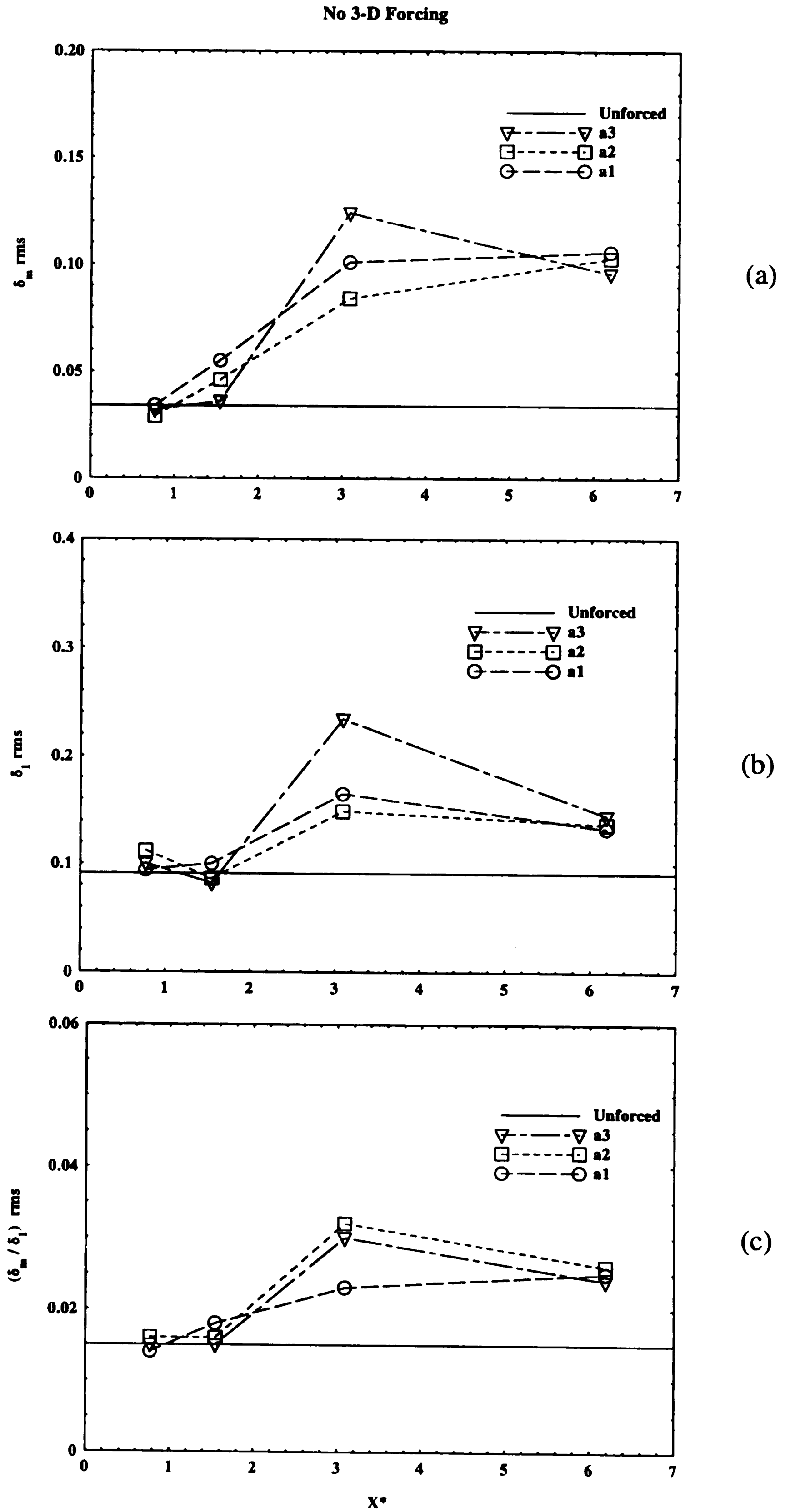

Figure 3.2.9. Spanwise rms quantities versus $x*$; no 3-D forcing.

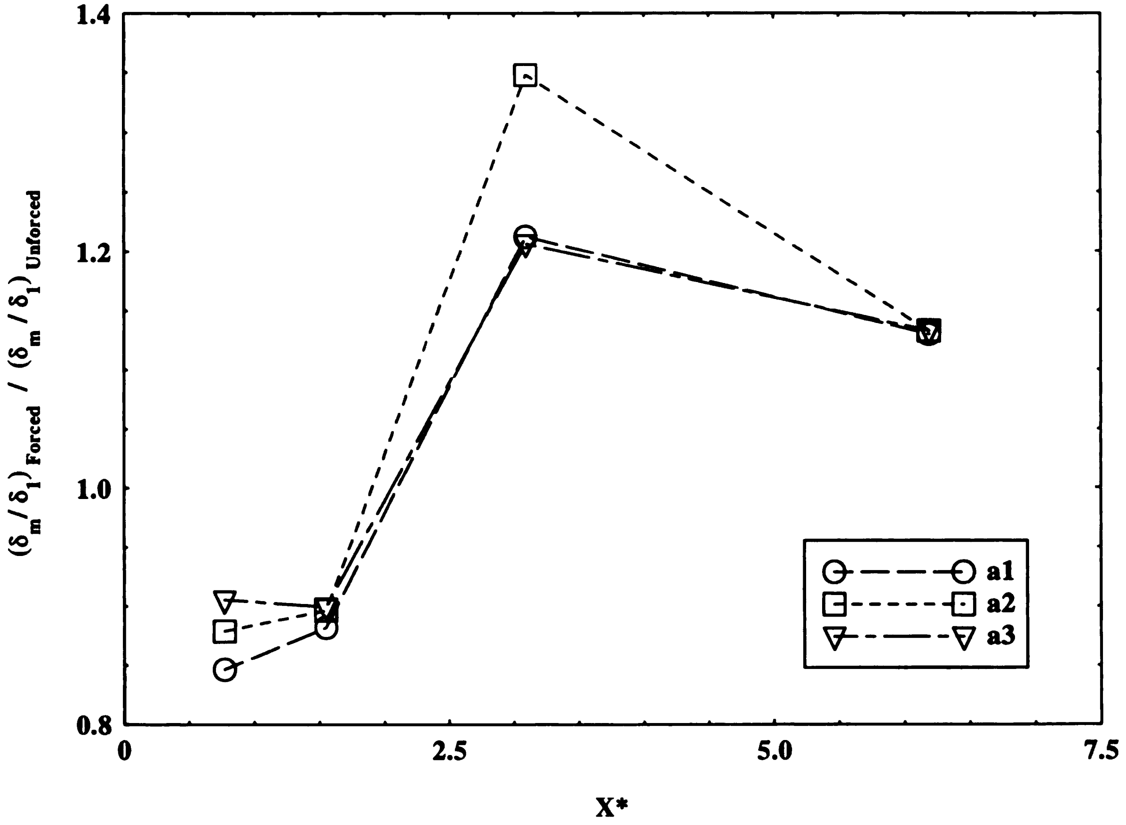

Figure 3.2.10. Forced mixed-fluid fraction relative to unforced mixed-fluid fraction; no 3-D forcing.

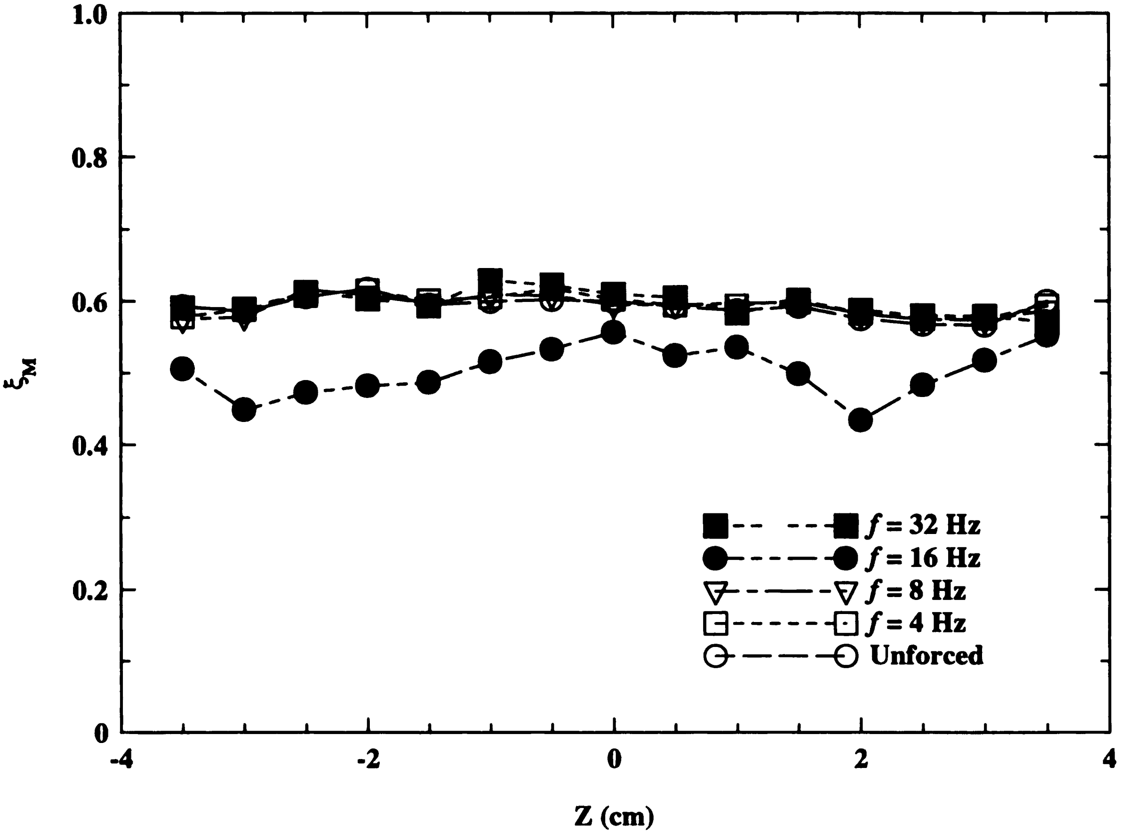

Figure 3.2.11. Average mixed-fluid concentration versus z at x = 17.4 cm; no 3-D forcing.

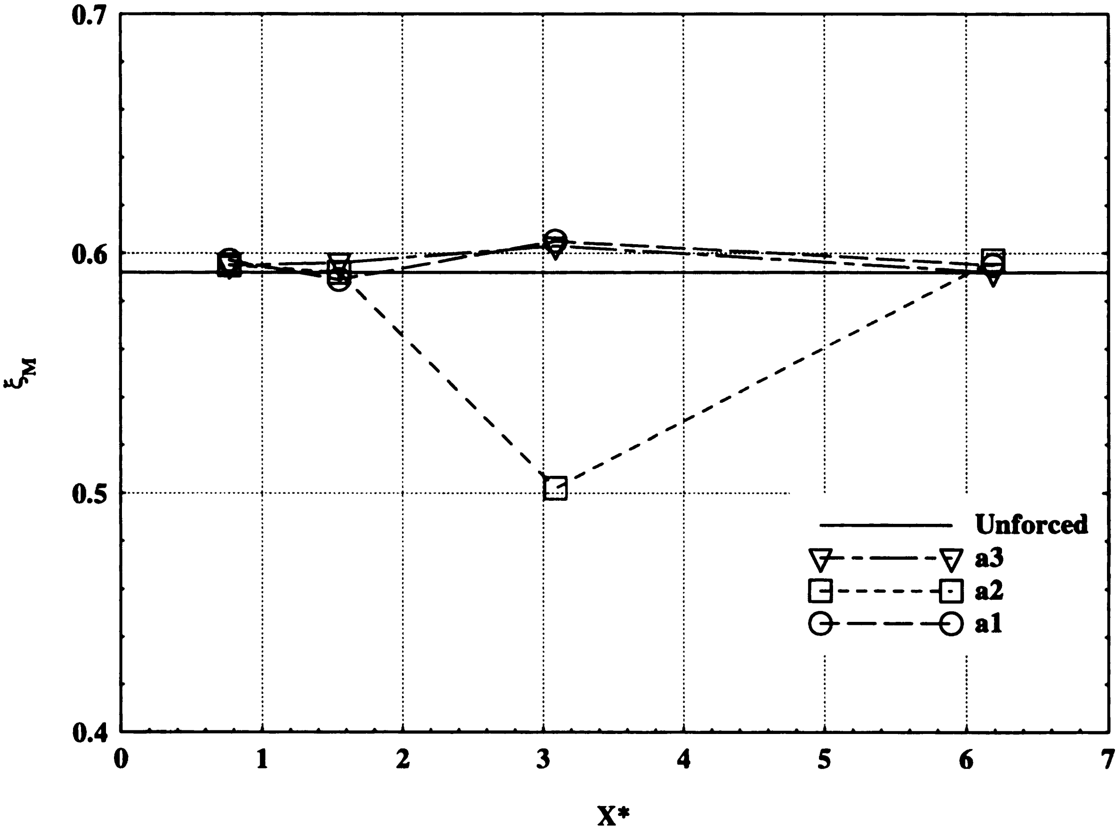

Figure 3.2.12. Span-averaged mean mixed-fluid concentration versus x^*; no 3-D forcing.

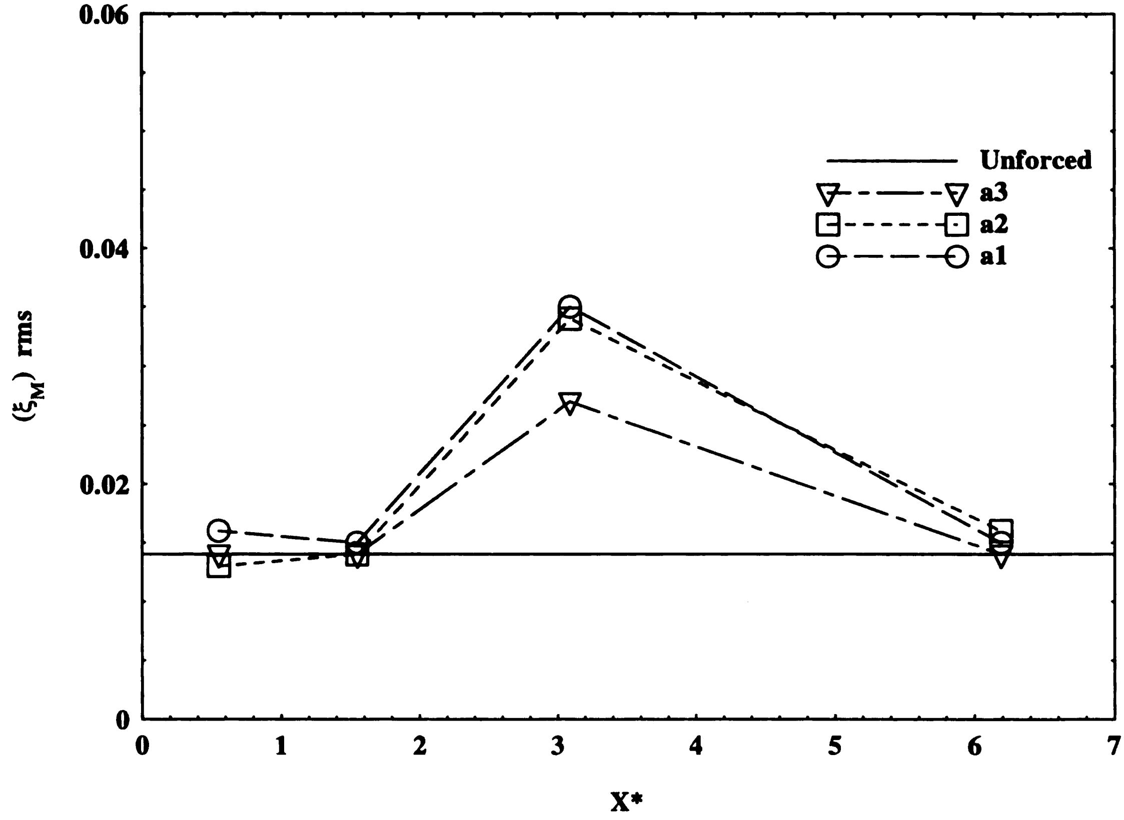

Figure 3.12.13. Spanwise rms of mean mixed-fluid fraction versus x^*; no 3-D forcing.

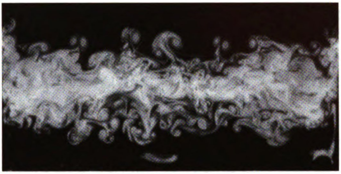

f = 8 Hz; $x^* \approx 1.55$

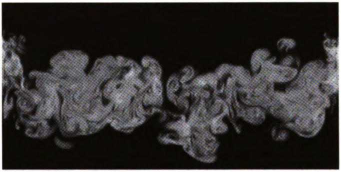

f = 16 Hz; $x^* \approx 3.1$

Figure 3.2.14. Spanwise flow structure and concentration field with purely 2-D forcing; $x = 17.4$ cm.

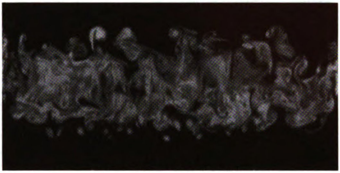

$f = 8$ Hz; $x^* \approx 1.55$

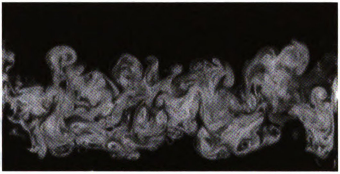

$f = 16$ Hz; $x^* \approx 3.1$

$C_{P2} = 0$ $C_{P2} = 1$

Figure 3.2.15. Spanwise flow structure and concentration field with purely 2-D forcing; $x = 17.4$ cm.

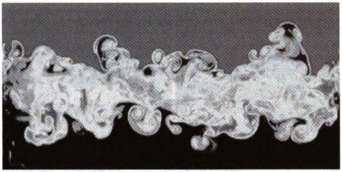

$f = 8$ Hz; $x^* = 1.55$

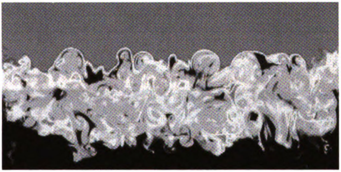

$f = 16$ Hz; $x^* = 3.1$

Figure 3.2.16. Spanwise flow structure and passive scalar concentration field with purely 2-D forcing.

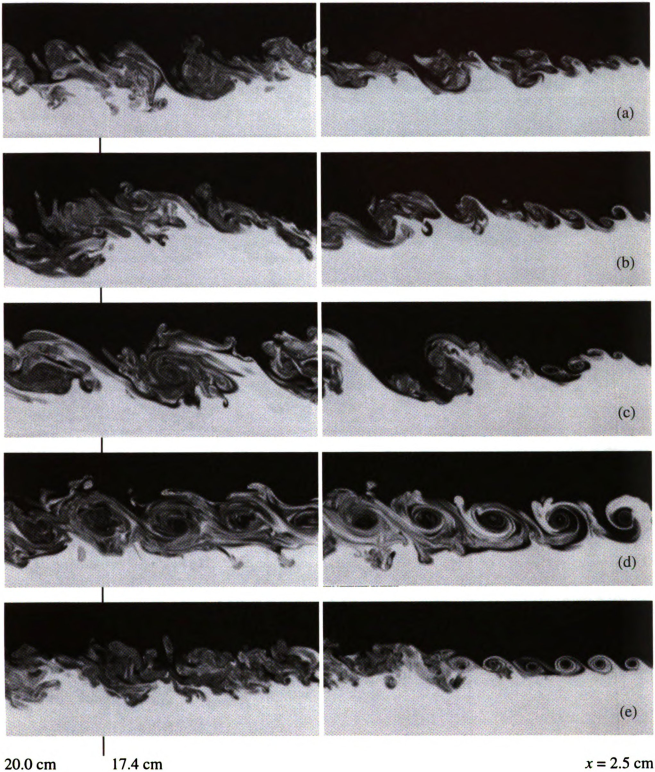

Figure 4.1.1. Streamwise flow structure and passive scalar concentration field with 3-D forcing (LS) for (a) no 2-D forcing, (b) $f = 4$ Hz, (c) $f = 8$ Hz, (d) $f = 16$ Hz, (e) $f = 32$ Hz; mid-amplitude.

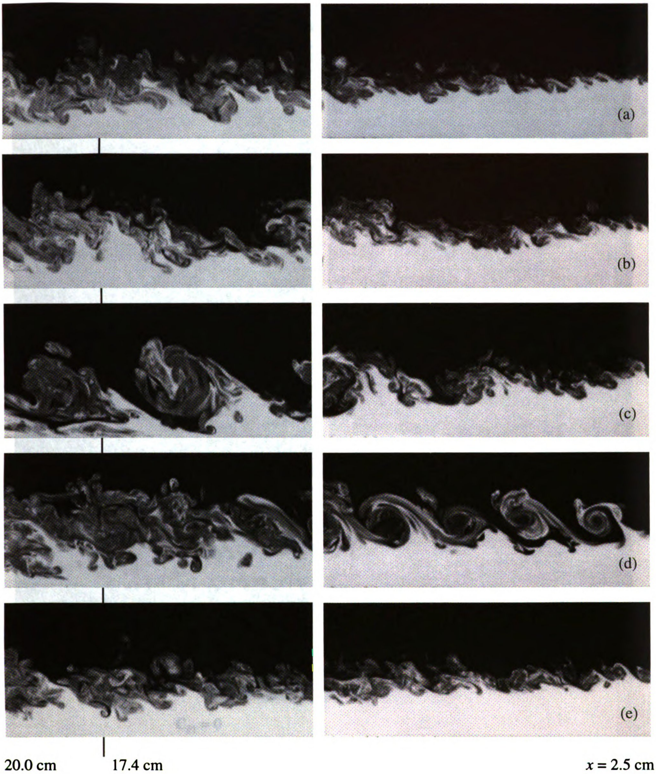

Figure 4.1.2. Streamwise flow structure and passive scalar concentration field with 3-D forcing (HS) for (a) no 2-D forcing, (b) $f = 4$ Hz, (c) $f = 8$ Hz, (d) $f = 16$ Hz, (e) $f = 32$ Hz.

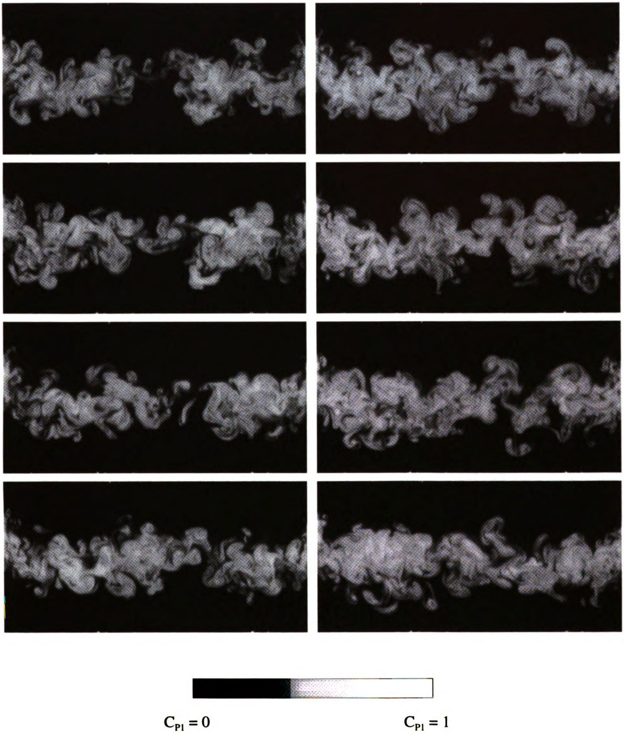

Figure 4.2.1. Spanwise flow structure and product concentration field in a shear layer with 3-D (LS) forcing; no 2-D forcing.

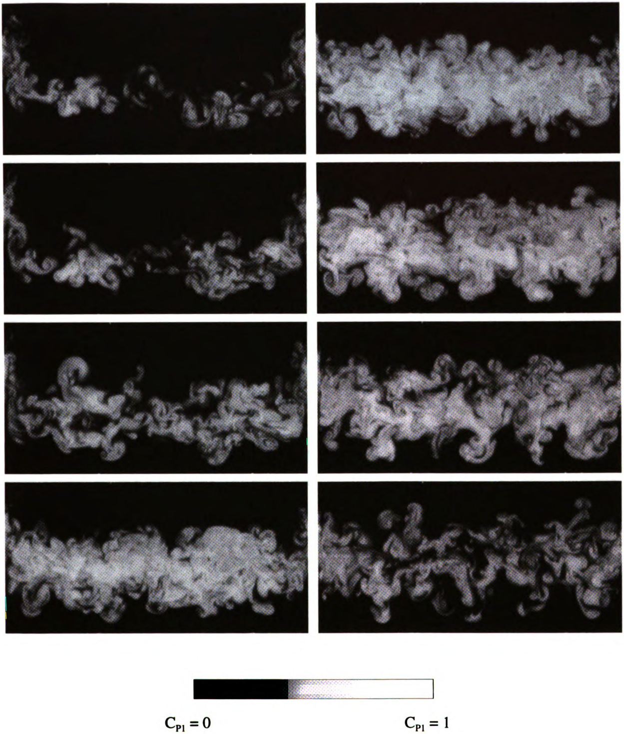

Figure 4.2.2. Spanwise flow structure and product concentration field in a shear layer with 2-D/ 3-D (LS) forcing; $f = 4$ Hz, $x^* = 0.77$, $f/f_o = 0.11$.

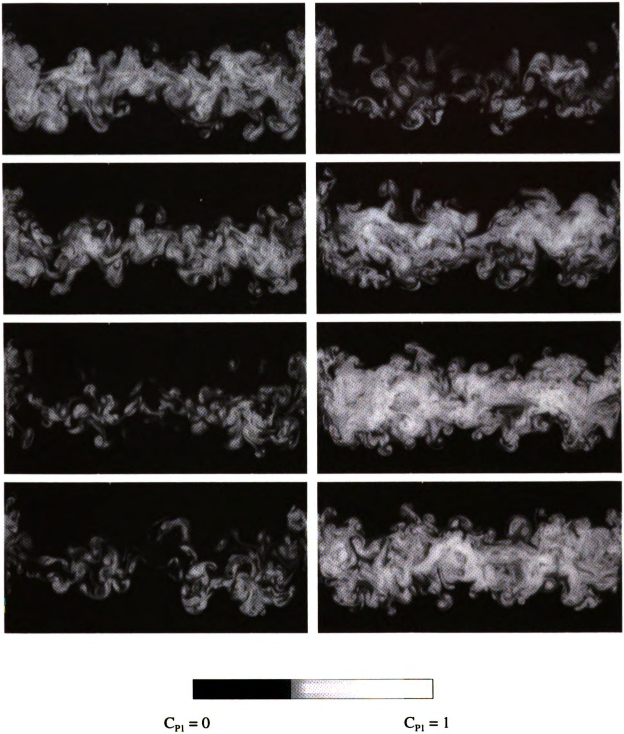

Figure 4.2.3. Spanwise flow structure and product concentration field in a shear layer with 2-D/ 3-D (LS) forcing; f = 8 Hz, x^* = 1.55, f/f_o = 0.21.

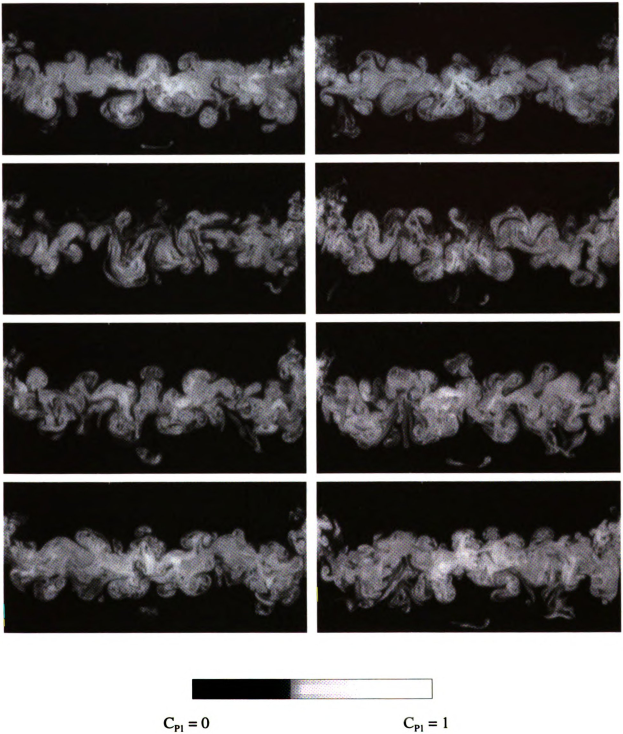

Figure 4.2.4. Spanwise flow structure and product concentration field in a shear layer with 2-D/ 3-D (LS) forcing; f = 16 Hz, x^* = 3.1, f/f_o = 0.42.

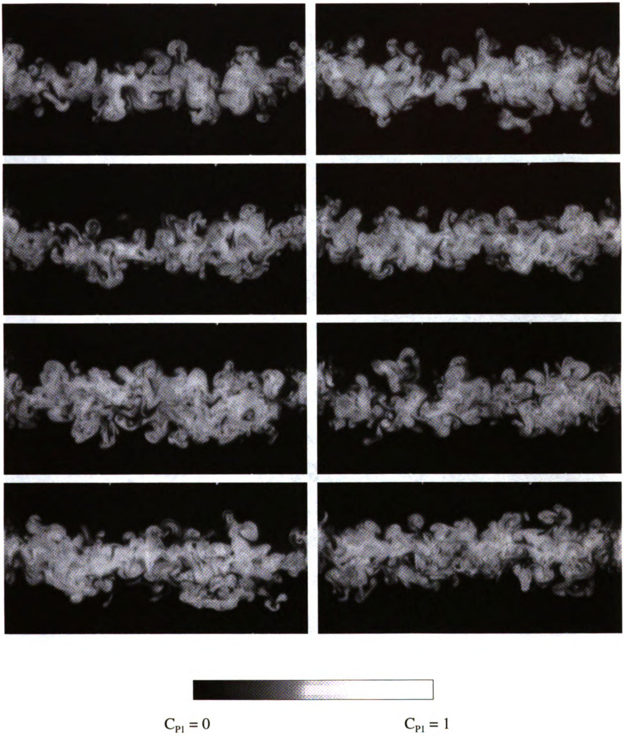

Figure 4.2.5. Spanwise flow structure and product concentration field in a shear layer with 2-D/3-D (LS) forcing; $f = 32$ Hz, $x^* = 6.2$, $f/f_o = 0.84$.

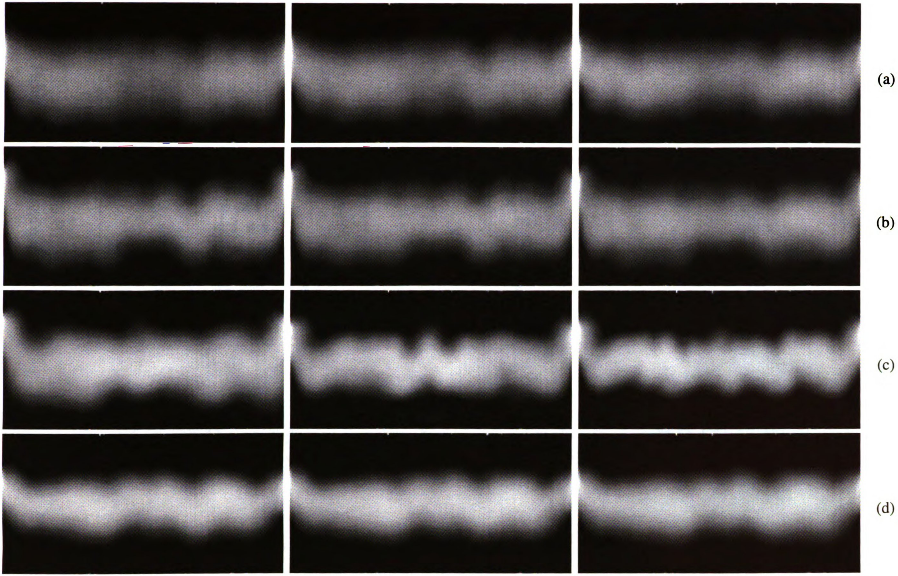

Figure 4.2.6. Average product concentration spanwise images for (a) $f = 4$ Hz, (b) $f = 8$ Hz, (c) $f = 16$ Hz, (d) $f = 32$ Hz; 3-D/LS forcing.

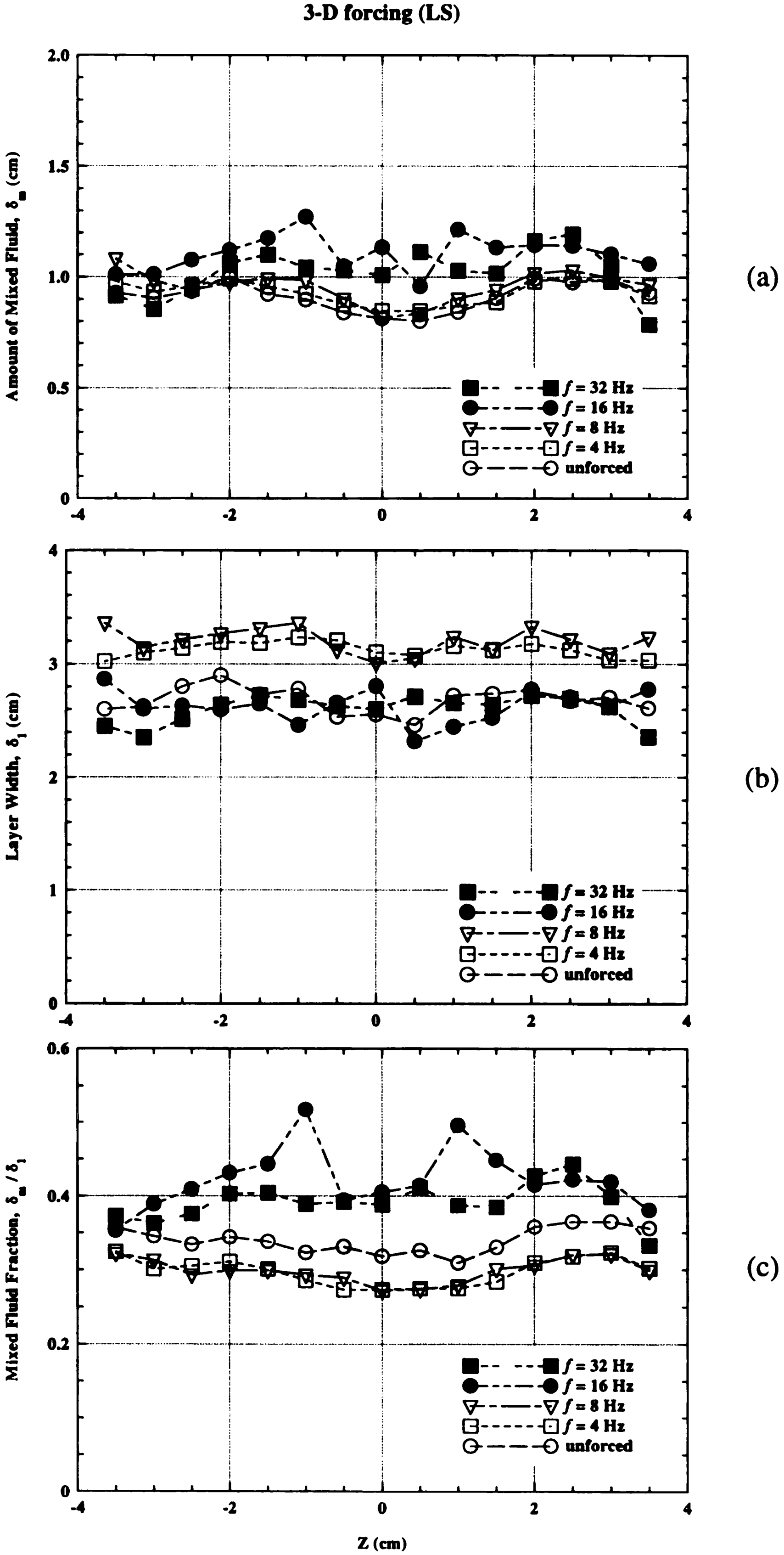

Figure 4.2.7. Calculated quantities versus z at x = 17.4 cm; 3-D(LS) forcing.

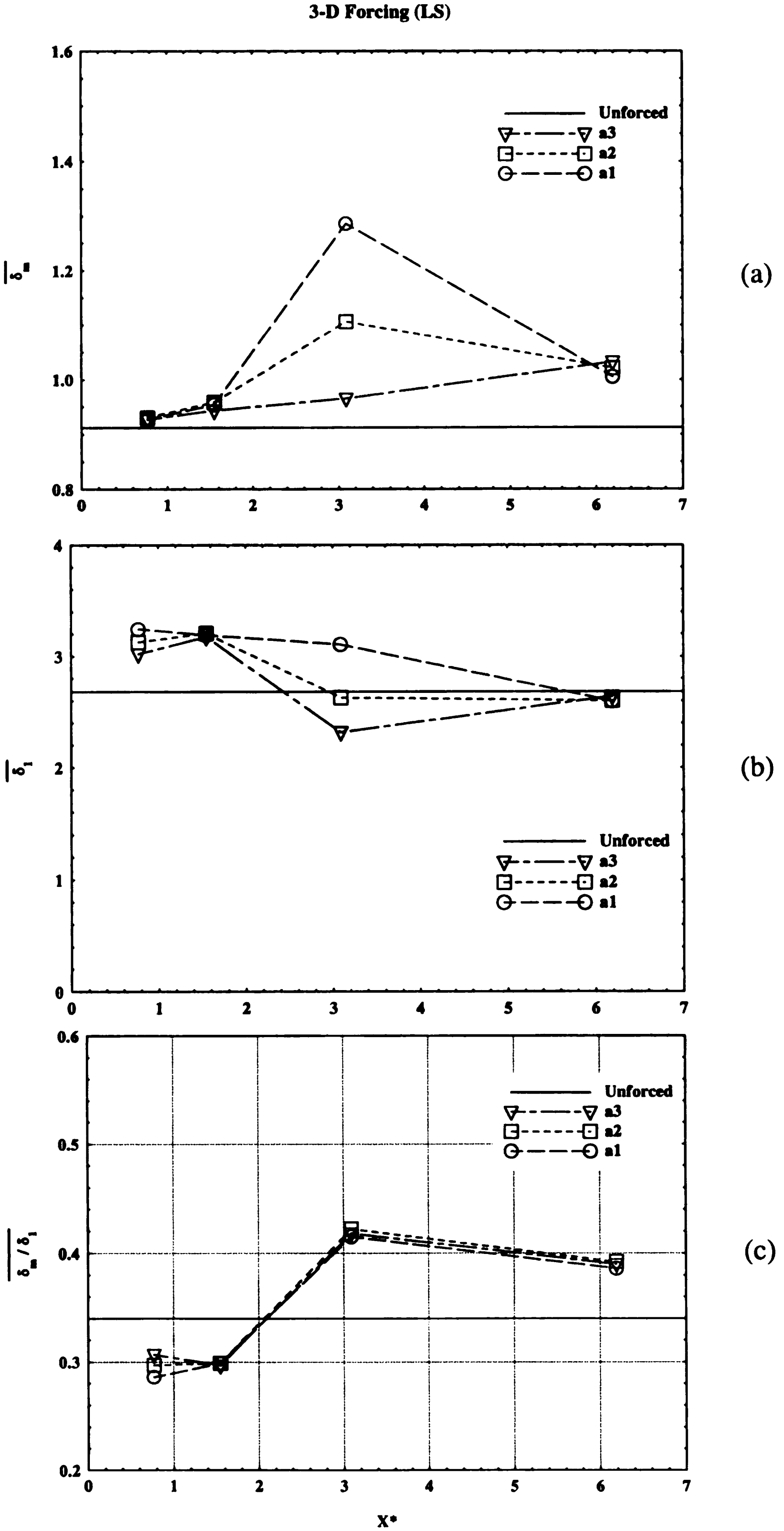

Figure 4.2.8. Span-averaged quantities versus x^*; 3-D(LS) forcing.

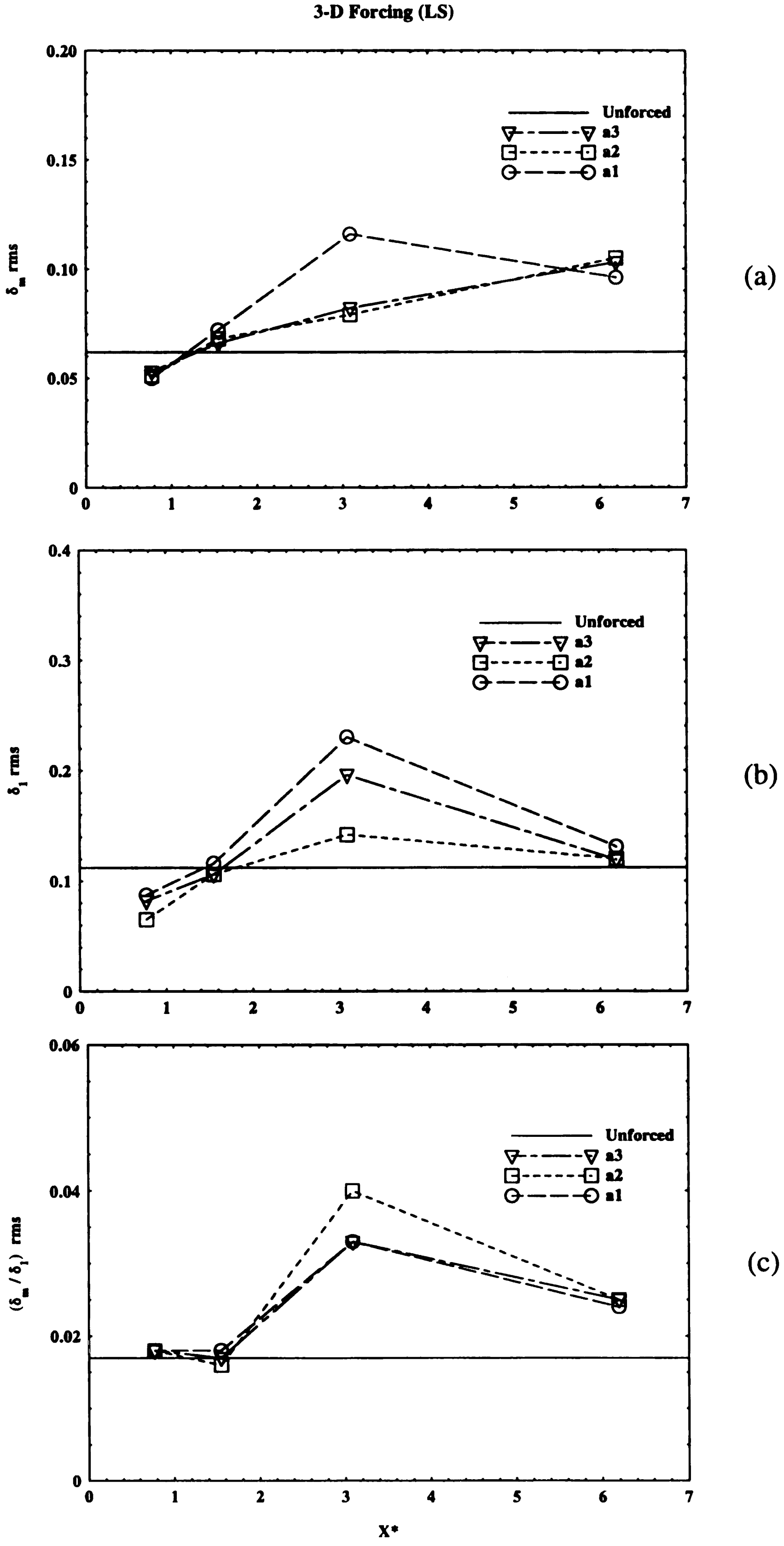

Figure 4.2.9. Spanwise rms quantities versus x*; 3-D(LS) forcing.

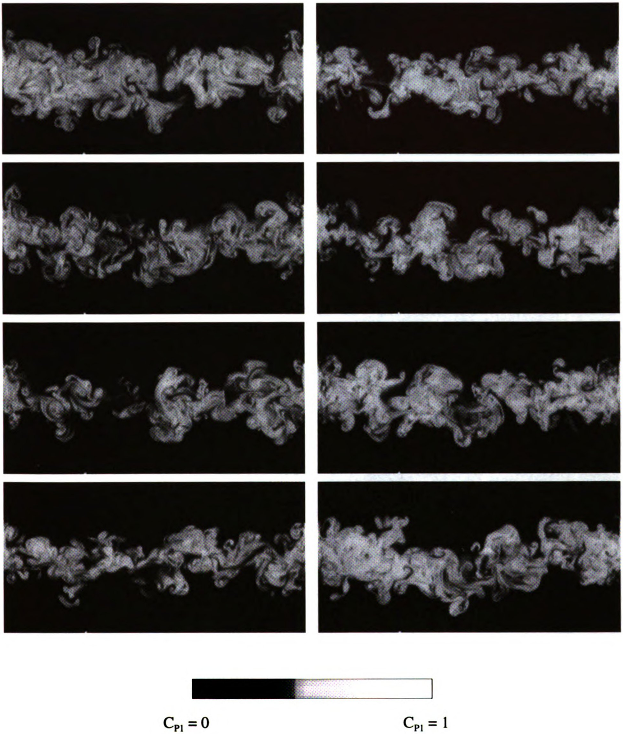

Figure 4.2.10. Spanwise flow structure and product concentration field in a shear layer with 3-D (HS) forcing; no 2-D forcing.

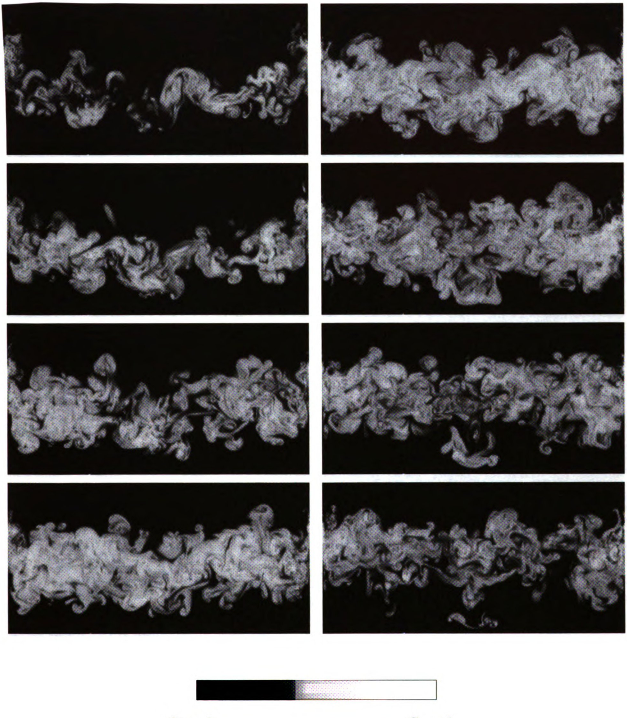

Figure 4.2.11. Spanwise flow structure and product concentration field in a shear layer with 2-D /3-D (HS) forcing; $f = 4$ Hz, $x^* = 0.77$, $f/f_o = 0.11$.

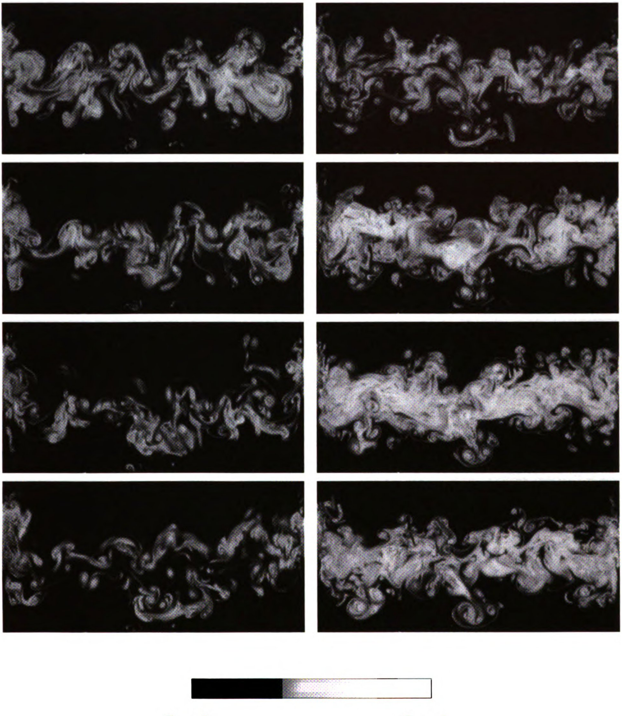

Figure 4.2.12. Spanwise flow structure and product concentration field in a shear layer with 2-D /3-D (HS) forcing; f = 8 Hz, x^* = 1.55, f/f_o = 0.21.

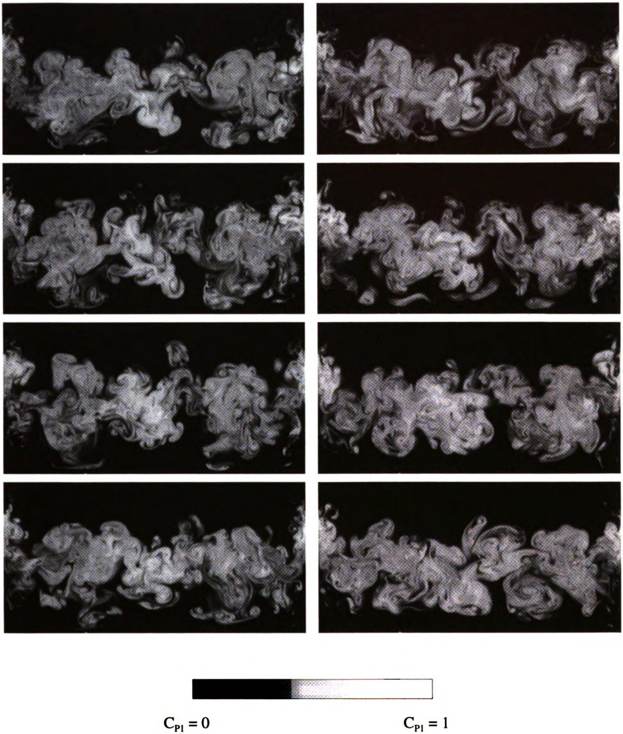

Figure 4.2.13. Spanwise flow structure and product concentration field in a shear layer with 2-D /3-D (HS) forcing; f = 16 Hz, x^* = 3.1, $f/f_o = 0.42$, high amplitude.

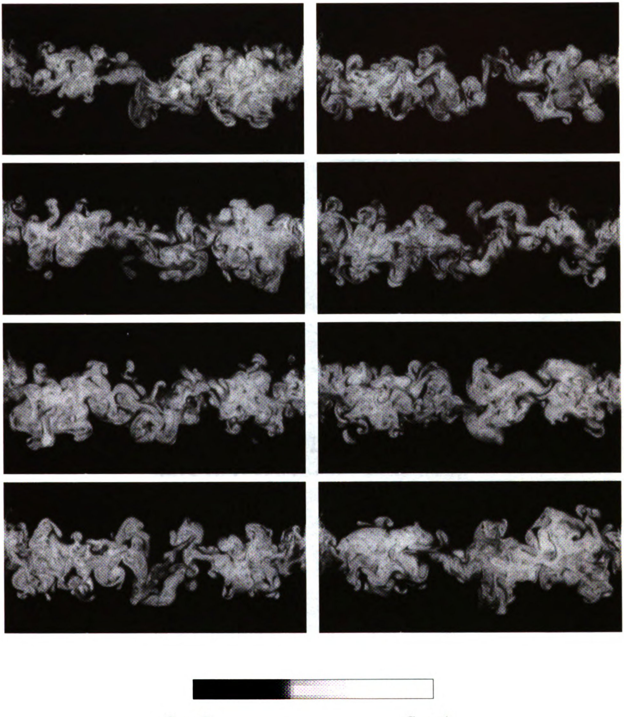

Figure 4.2.14. Spanwise flow structure and product concentration field in a shear layer with 2-D /3-D (HS) forcing; $f = 32$ Hz, $x^* = 6.2$, $f/f_o = 0.84$.

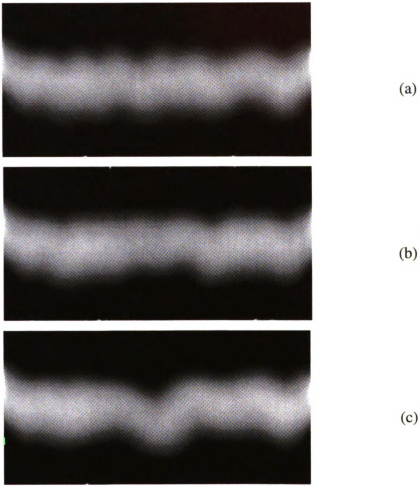

Figure 4.2.15. Averaged product concentration spanwise images with no 2-D forcing for (a) no 3-D forcing, (b) 3-D(LS) forcing, and (c) 3-D(HS) forcing.

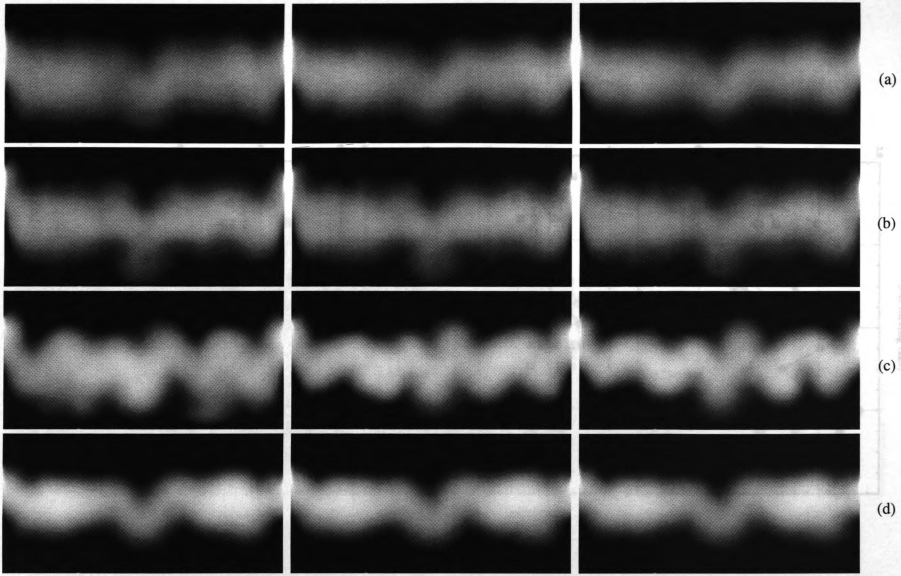

Figure 4.2.16. Average product concentration spanwise images for (a) $f = 4$ Hz, (b) $f = 8$ Hz, (c) $f = 16$ Hz, (d) $f = 32$ Hz; 3-D/HS forcing.

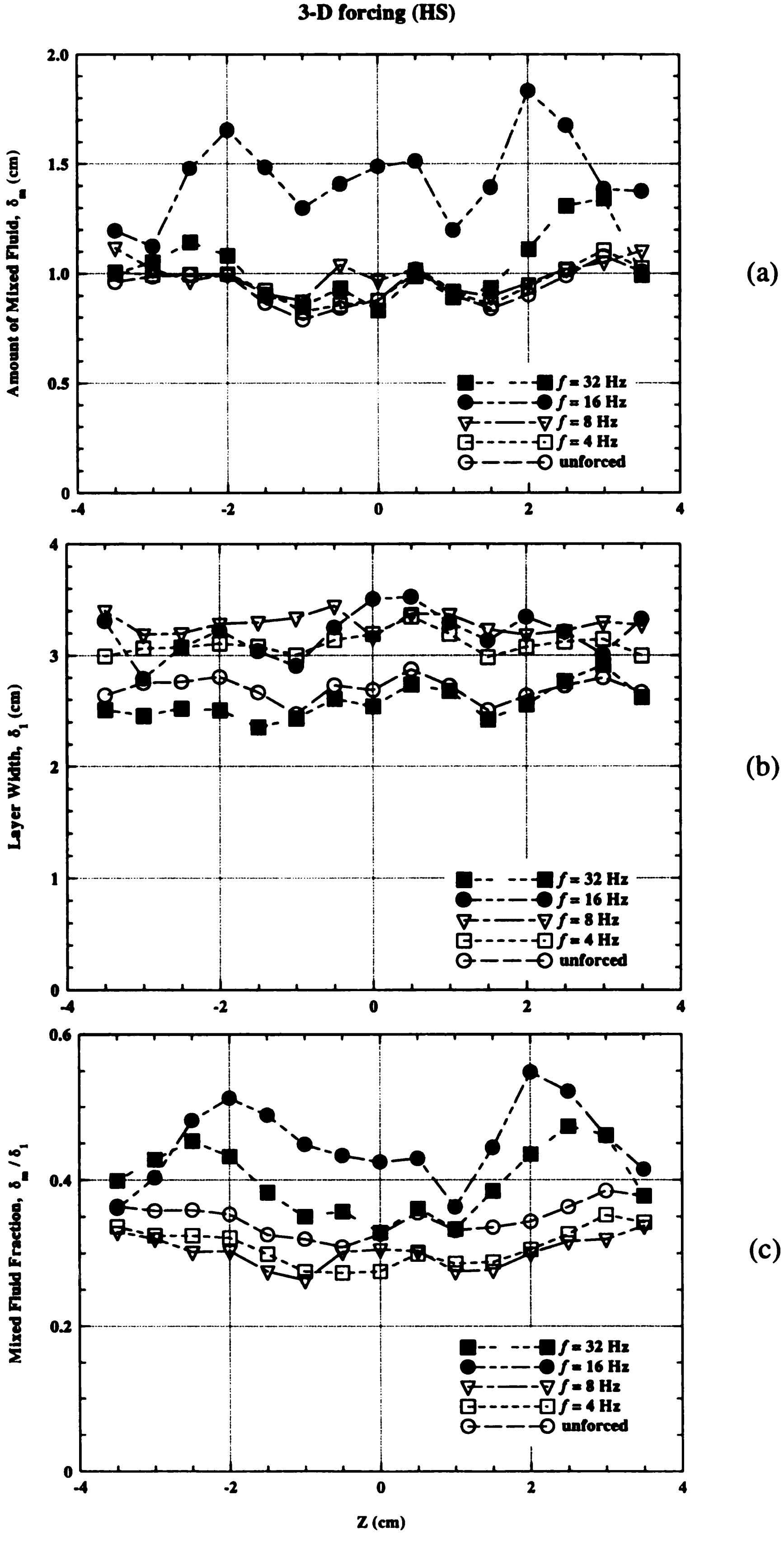

Figure 4.2.17. Calculated quantities versus z at x = 17.4 cm; 3-D(HS) forcing.

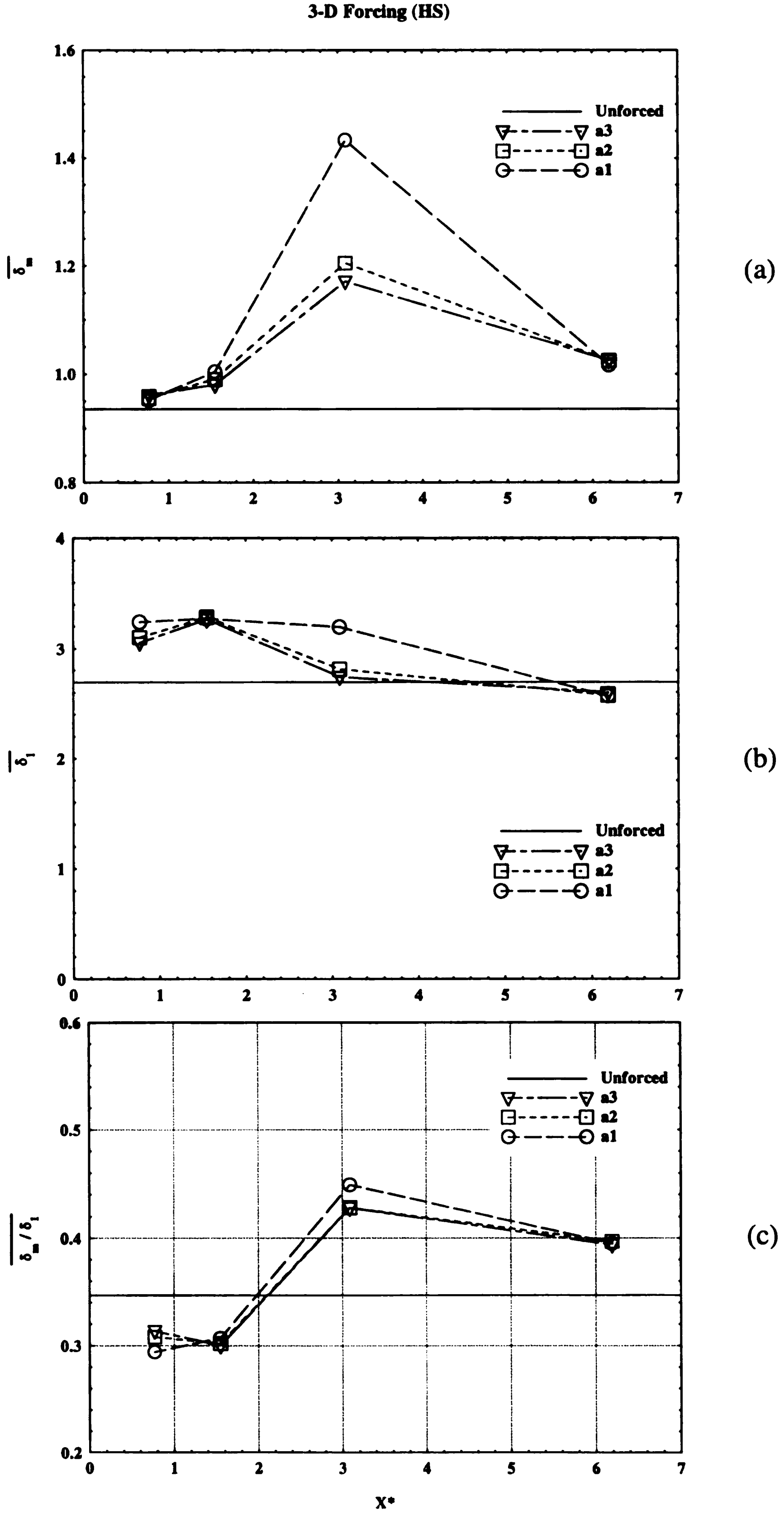

Figure 4.2.18. Span-averaged quantities versus *x**; 3-D(HS) forcing.

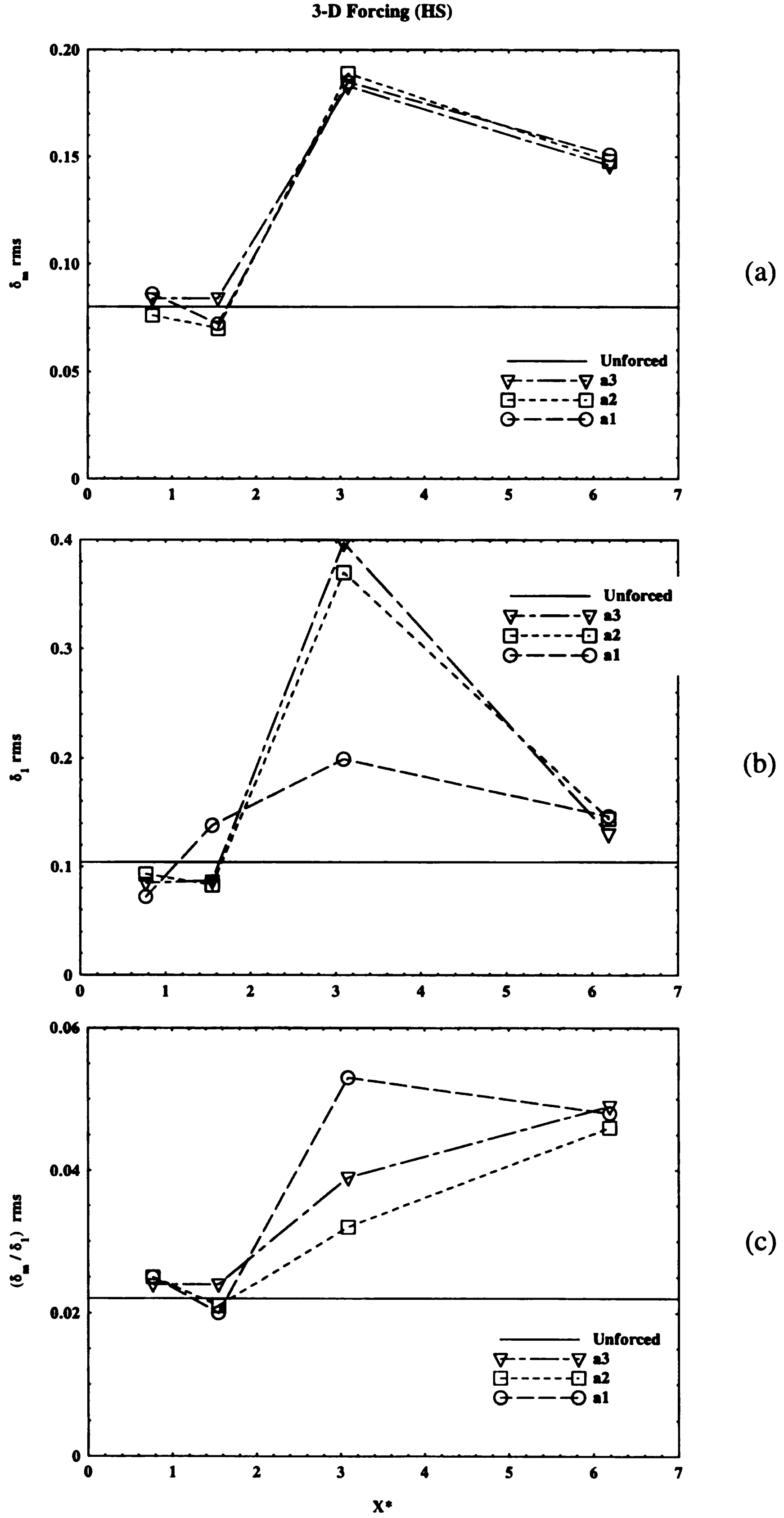

Figure 4.2.19. Spanwise rms quantities versus x^*; 3-D(HS) forcing.

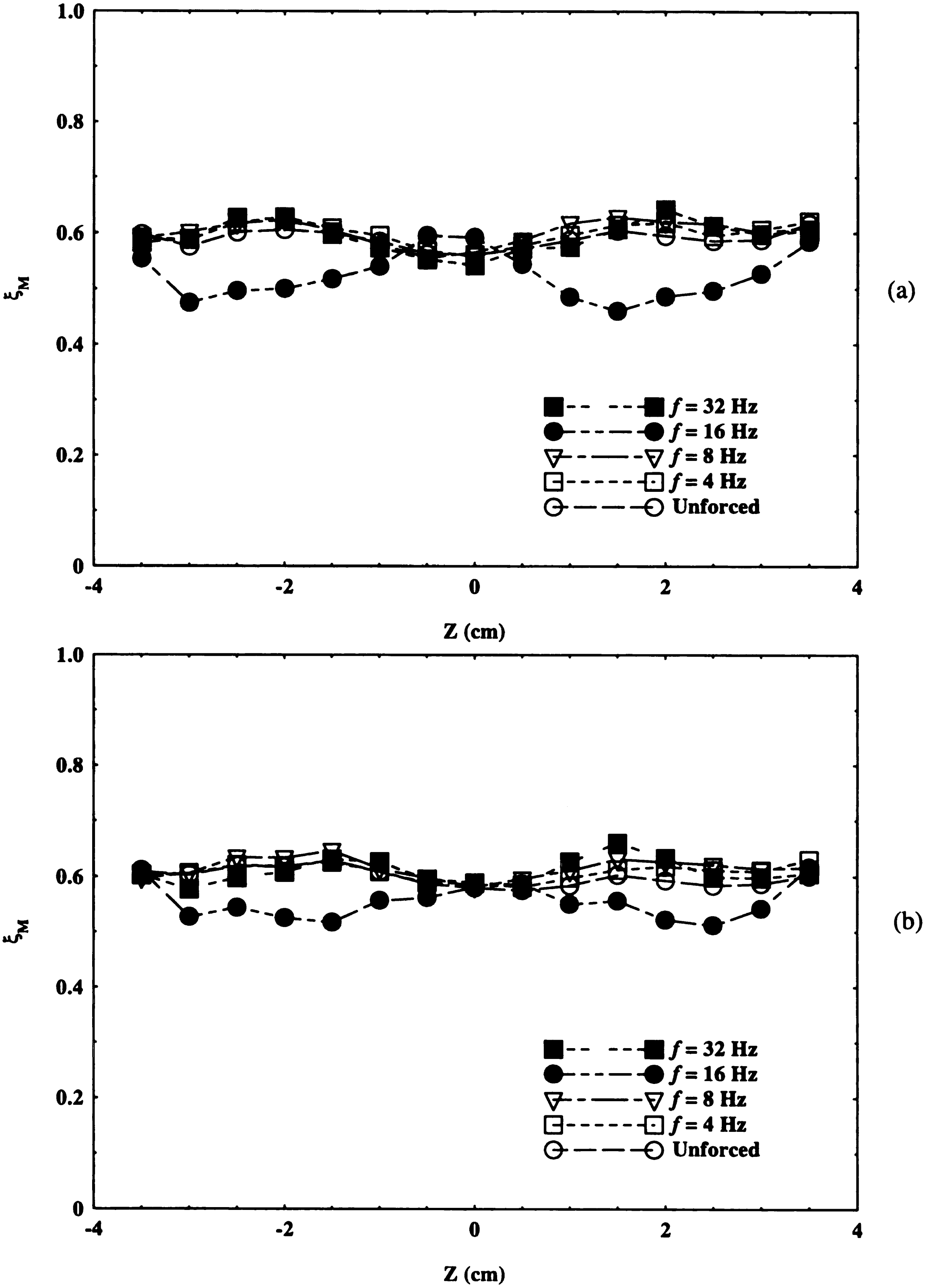

Figure 4.2.20. Average mixed-fluid concentration versus *z* at *x* = 17.4 cm; (a) 3-D(HS) forcing, (b) 3-D(LS) forcing.

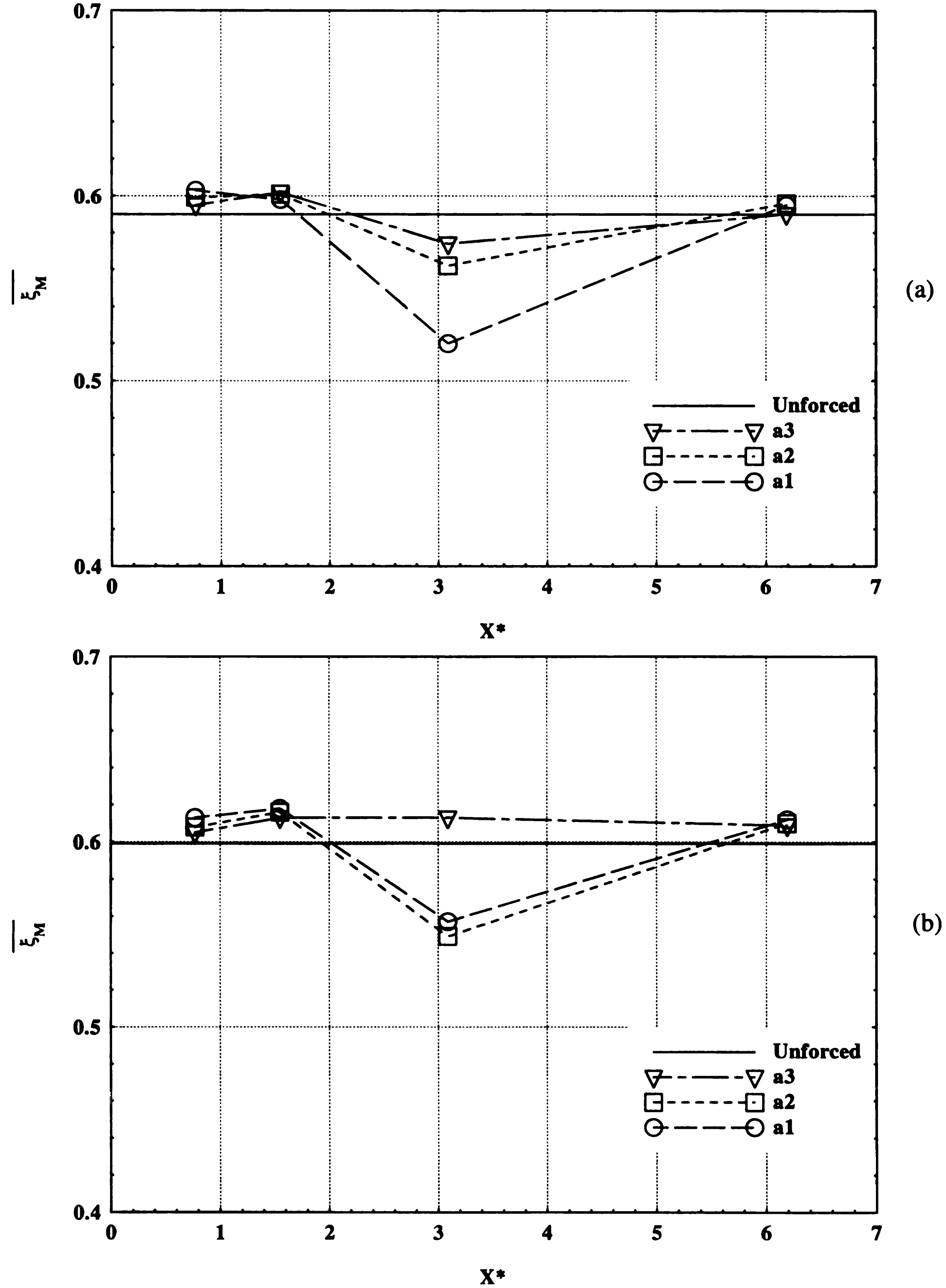

Figure 4.2.21. Span averaged mean mixed-fluid concentration versus x^*; (a) 3-D(HS) forcing, (b) 3-D(LS) forcing.

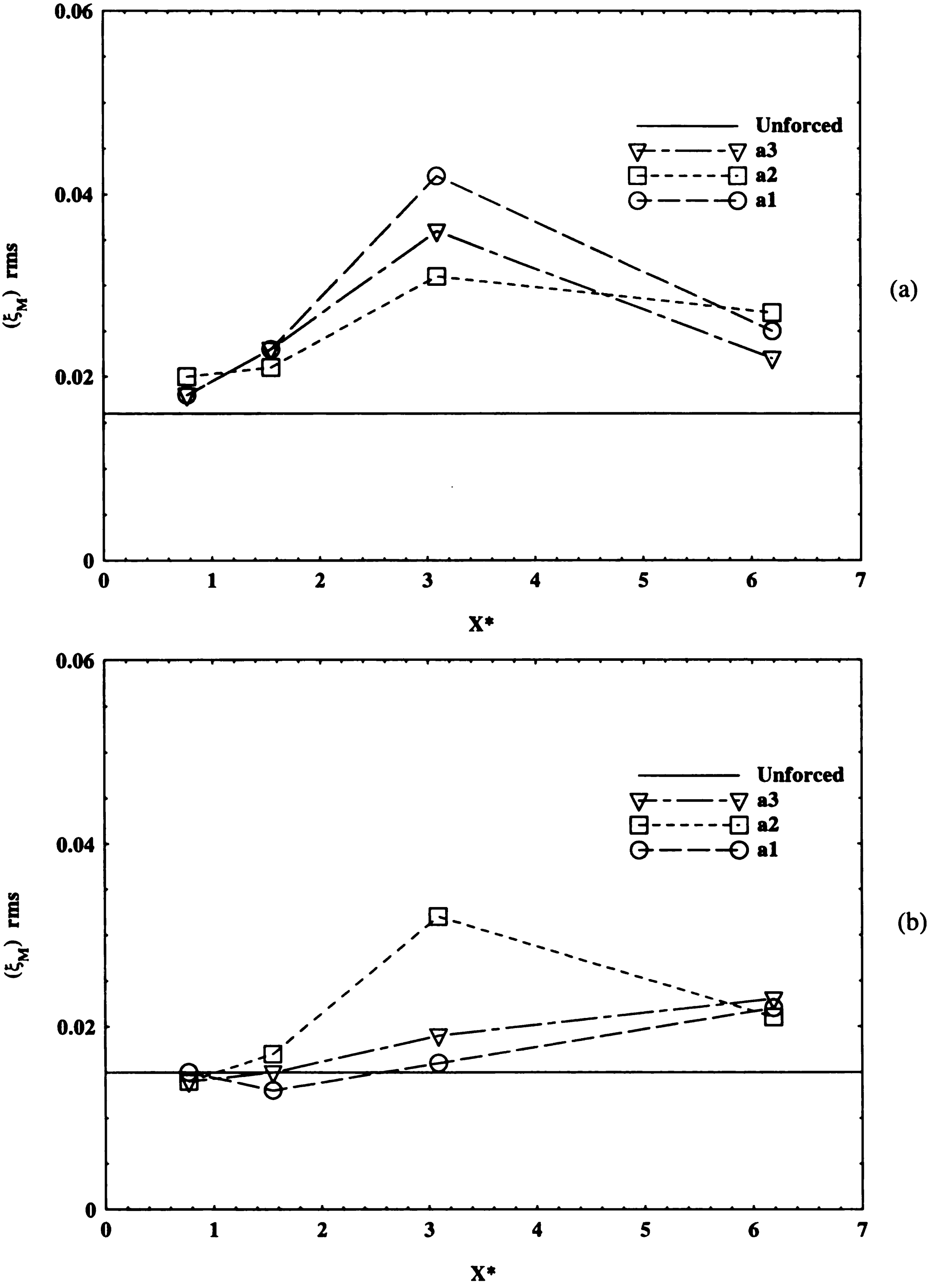

Figure 4.2.22. Spanwise rms of mean mixed-fluid concentration versus x^*; (a) 3-D(HS) forcing, (b) 3-D(LS) forcing.

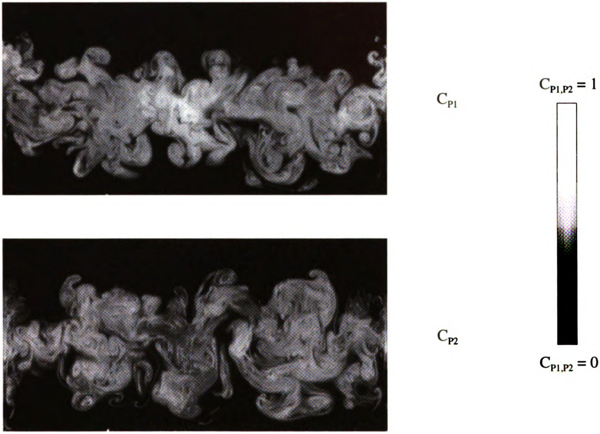

Figure 4.2.23. Spanwise flow structure and product concentration field with 2-D / 3-D(HS) forcing; *f* = 16 Hz, $x^* = 3.1$, highest amplitude.

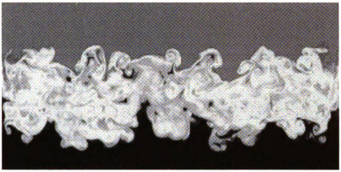

$f = 4$ Hz; $x^* = 0.77$

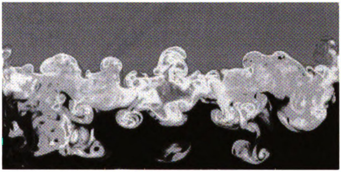

$f = 16$ Hz; $x^* = 3.1$

Figure 4.2.24. Spanwise flow structure and passive scalar concentration field with 2-D/3-D (LS) forcing.

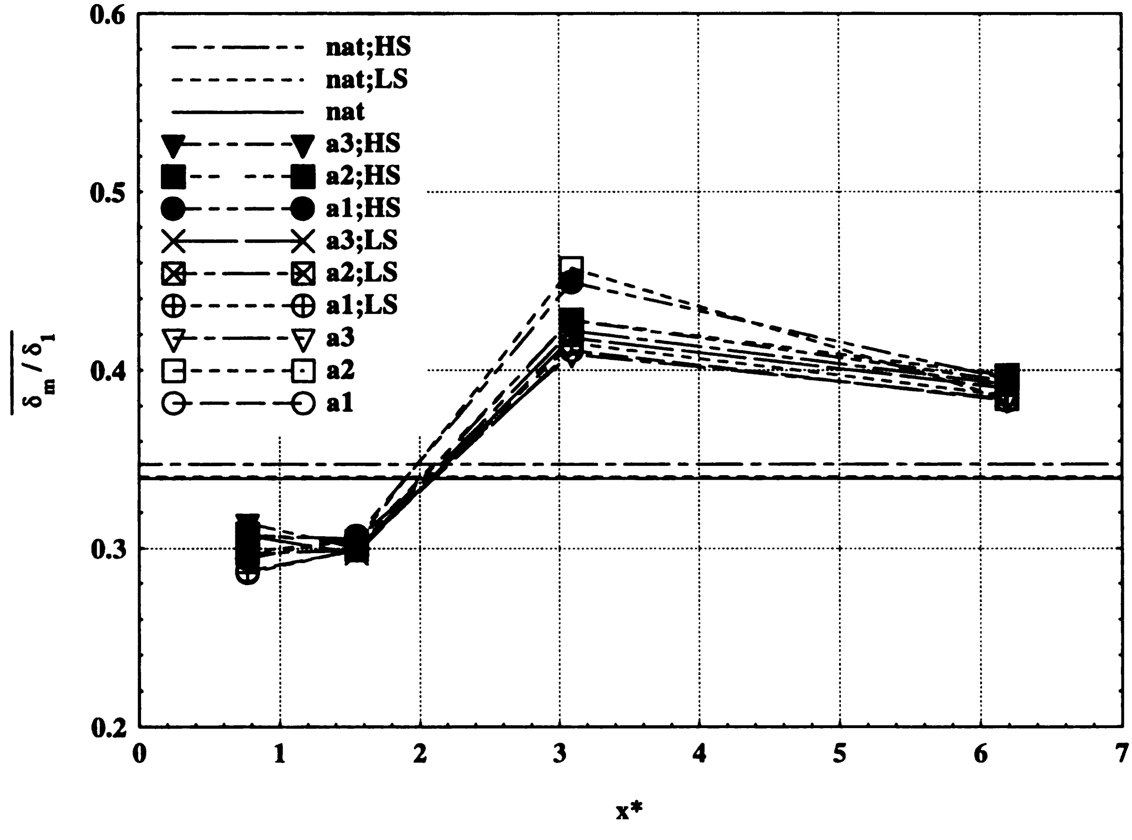

Figure 4.2.25. Mixed-fluid fraction versus x^* for all cases.

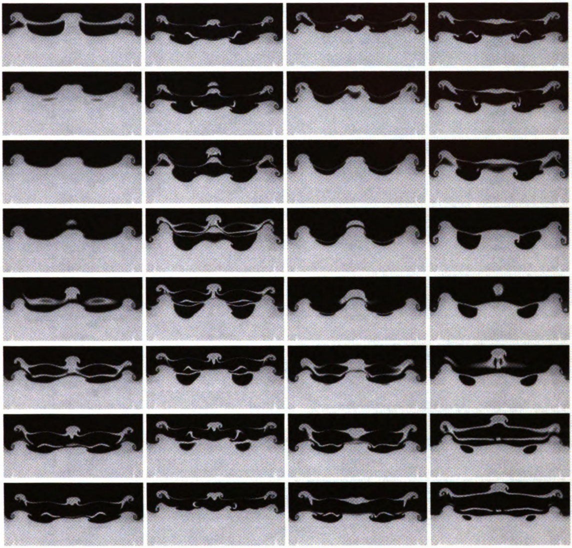

Figure 4.3.1. Spanwise passive scalar structure and concentration field in a *low speed* shear layer with 3-D(LS) forcing and no 2-D forcing.

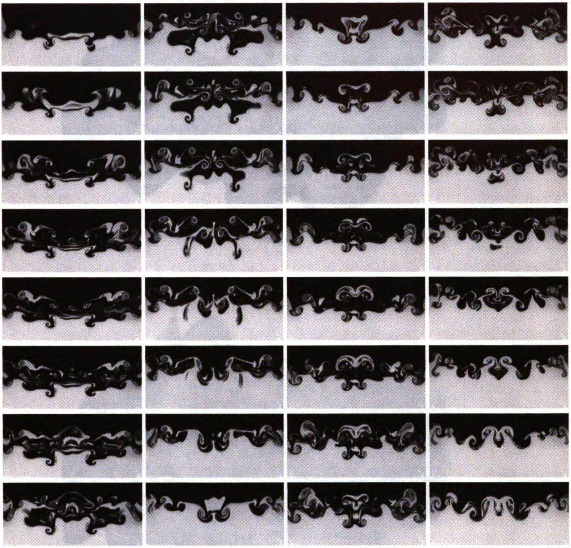

Figure 4.3.2. Spanwise passive scalar structure and concentration field in a *low speed* shear layer with 3-D(LS) forcing and 2-D forcing at $f = 8$ Hz.

Figure 4.
with 3-D

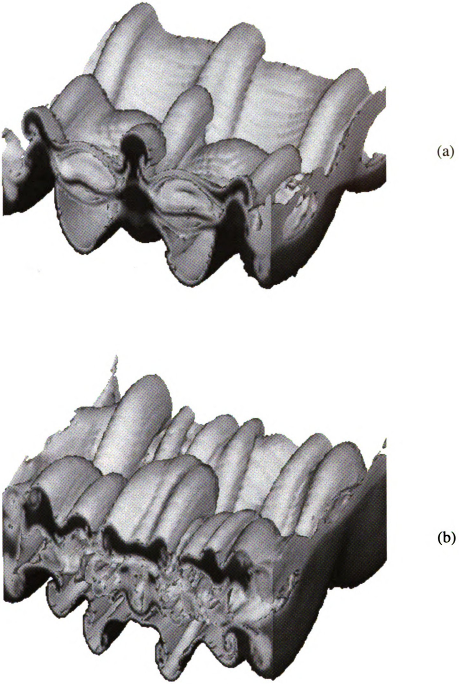

Figure 4.3.3. Volumetric rendering of iso-concentration surfaces in the low speed shear layer with 3-D(LS) forcing along with (a) no 2-D forcing and (b) $f = 8$ Hz.

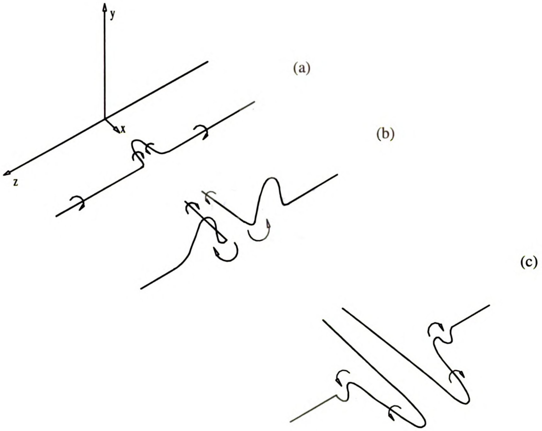

Figure 4.3.4. Mechanism for axial vorticity generation.

LIF Image

MTV Image Pair

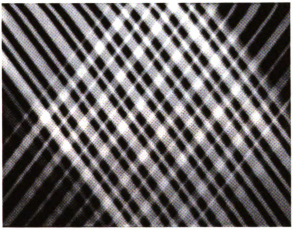

MTV: Image of tagged regions at $t = t_o$.

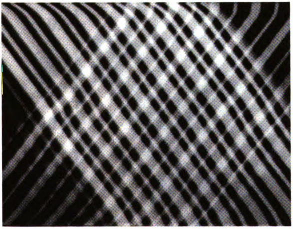

MTV: Image of **tagged regions** at $t = t_o + \Delta t$.

Figure 5.2.5. Sample images for simultaneous concentration/velocity measurements.

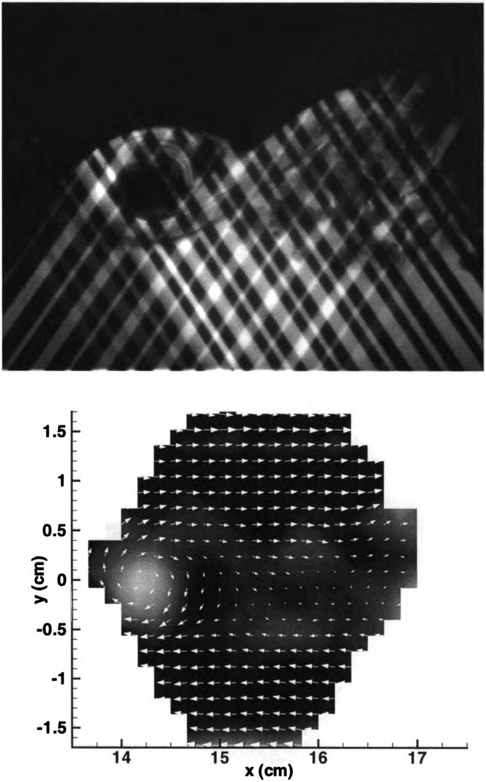

Figure 5.3.1. Simultaneous concentration field from LIF (top) and velocity/vorticity field from MTV (bottom); no 2-D forcing

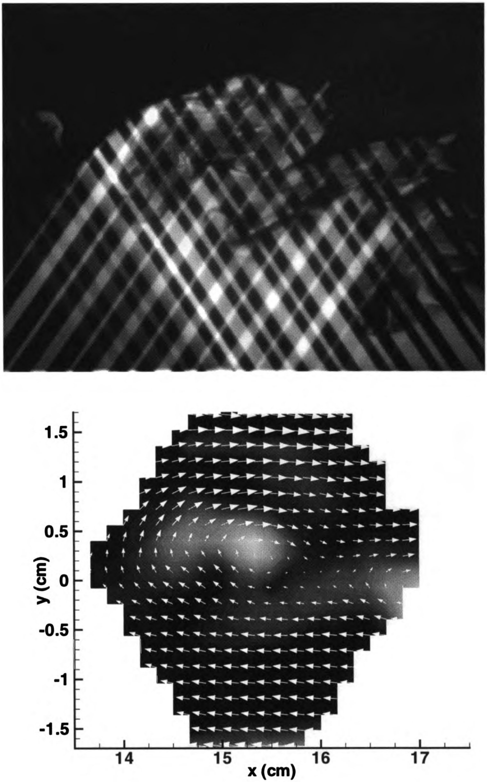

Figure 5.3.2. Simultaneous concentration field from LIF (top) and velocity/vorticity field from MTV (bottom); $f = 4$ Hz.

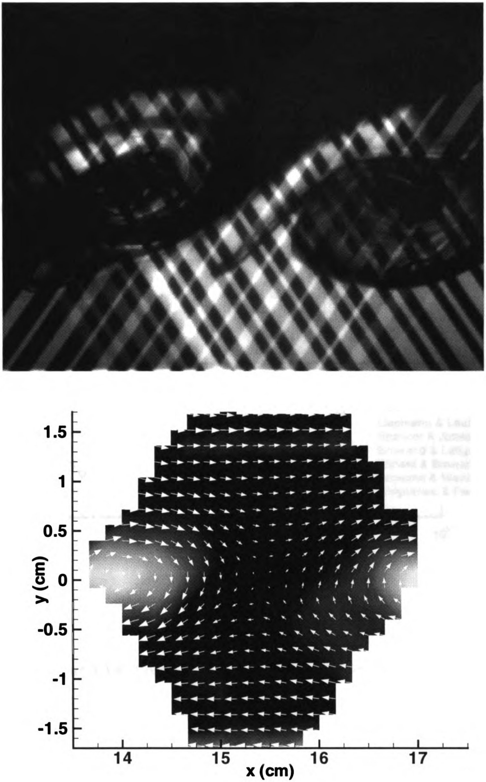

Figure 5.3.3. Simultaneous concentration field from LIF (top) and velocity/vorticity field from MTV (bottom); *f* = 8 Hz.

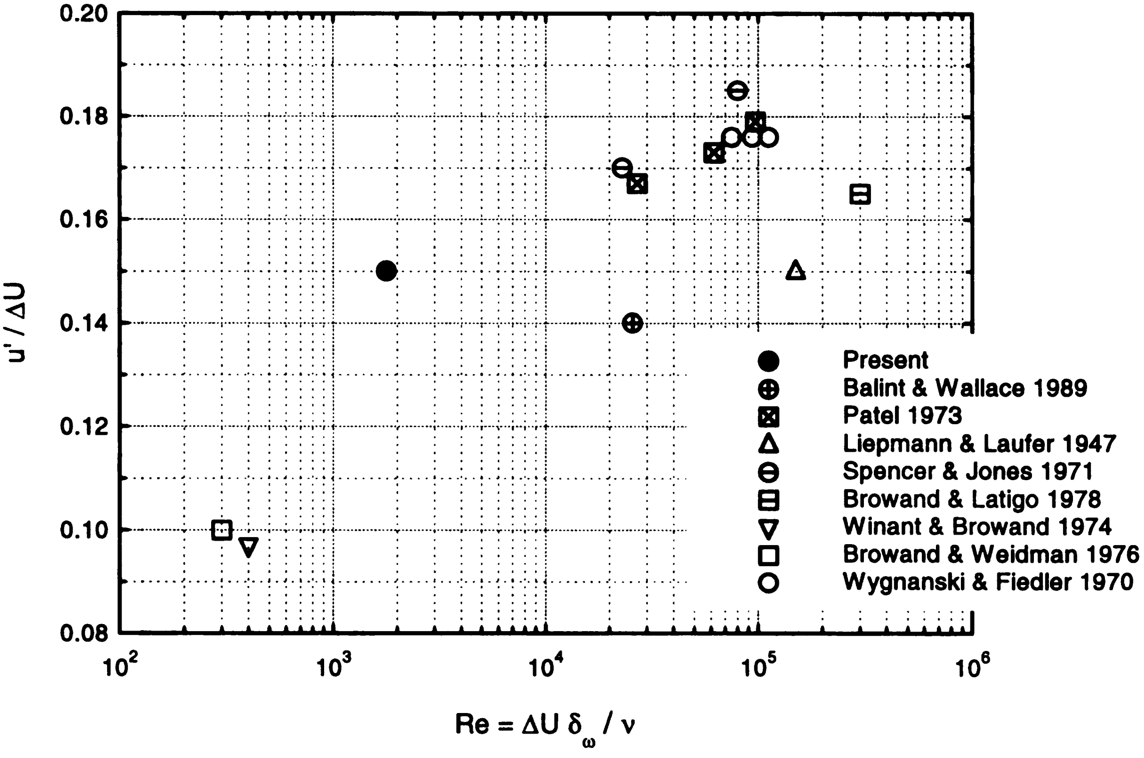

Figure 5.3.4. Compilation of u_{rms} data in the plane shear layer.

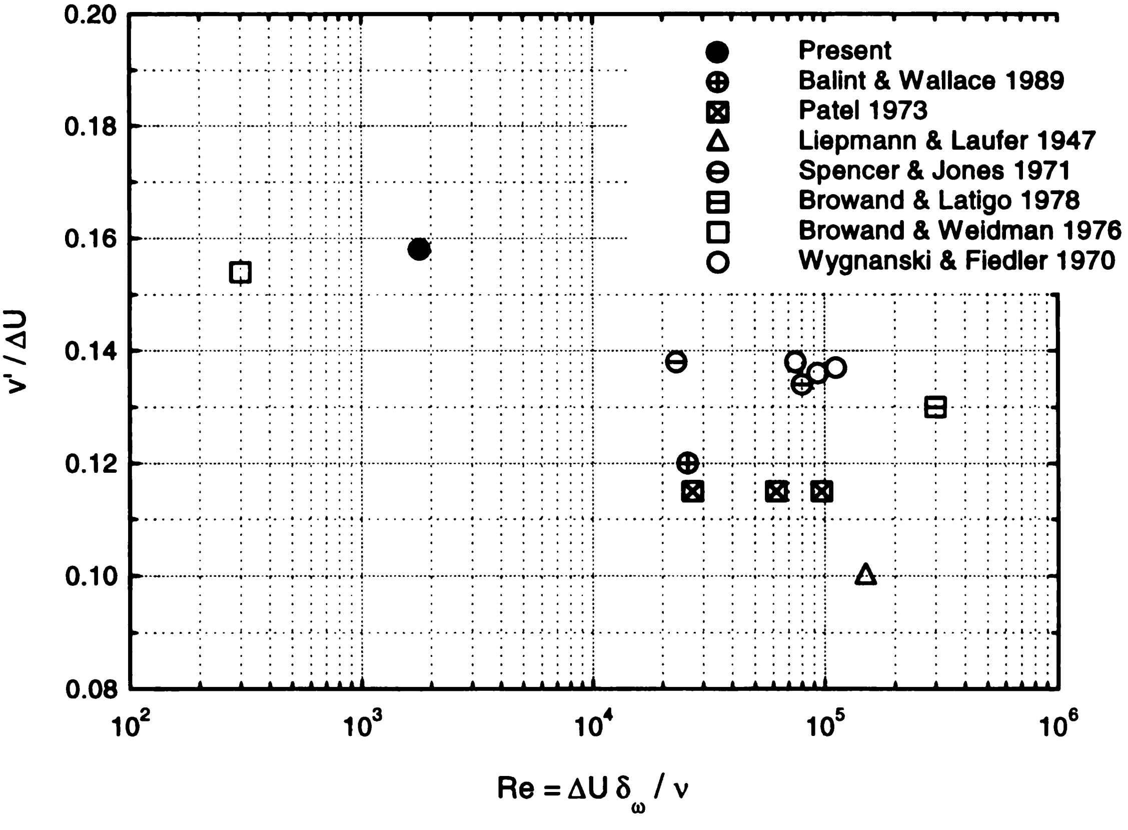

Figure 5.3.5. Compilation of v_{rms} data in the plane shear layer.

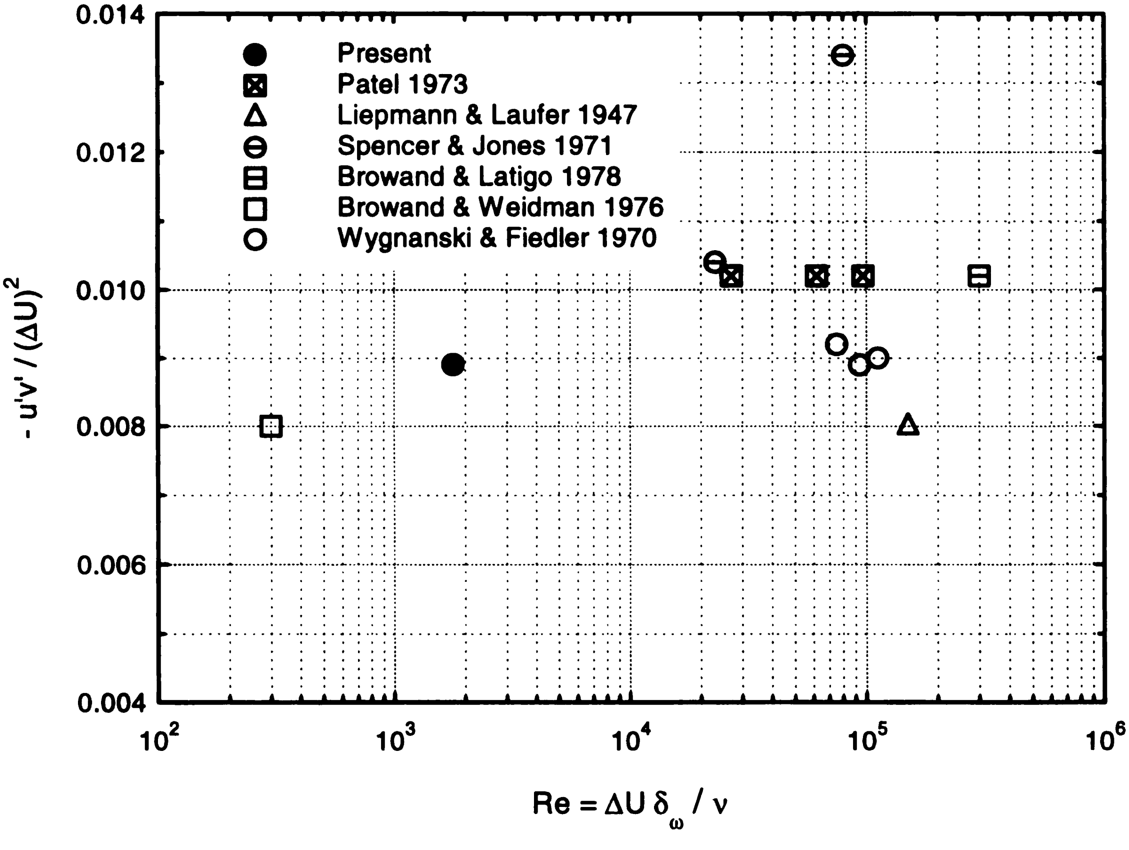

Figure 5.3.6. Compilation of Reynolds stress data in the plane shear layer.

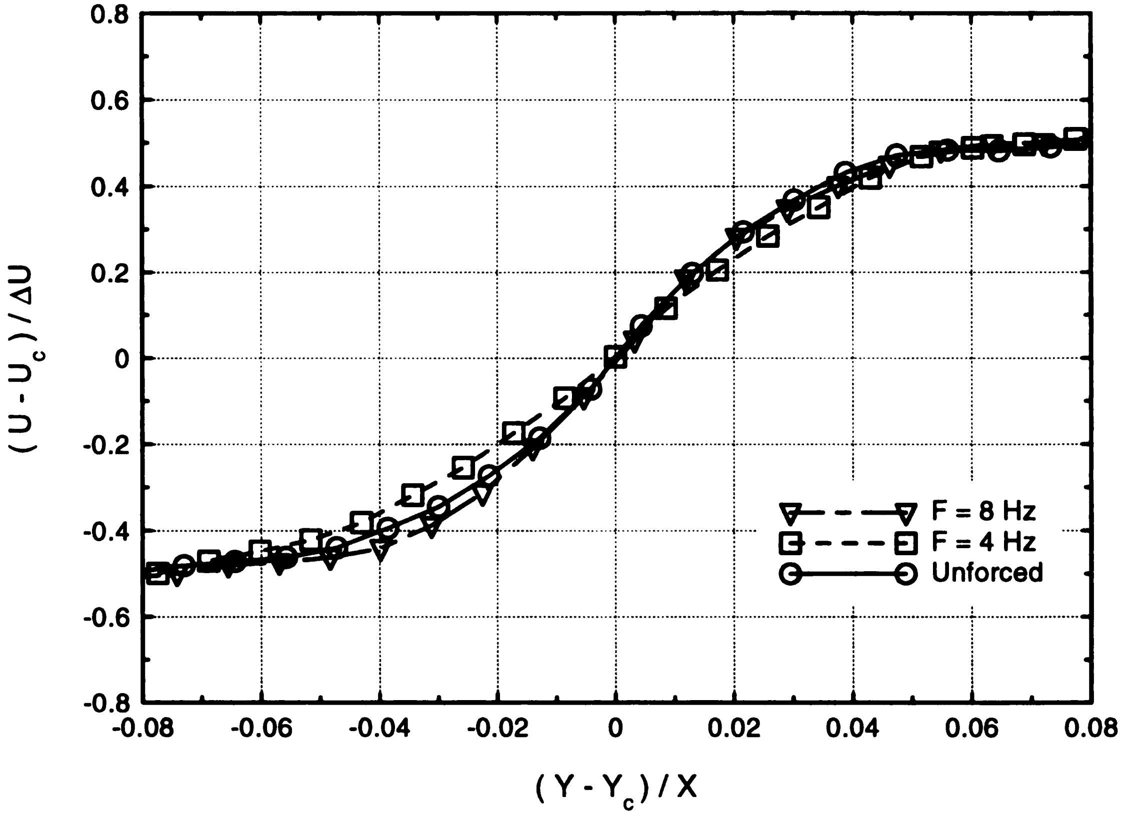

Figure 5.3.7. Normalized profiles of mean velocity.

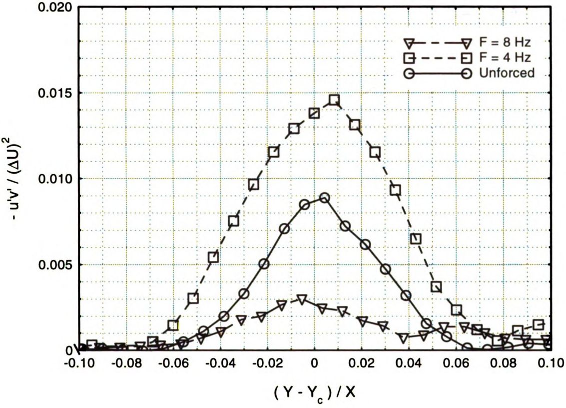

Figure 5.3.8. Normalized profiles of Reynolds stress.

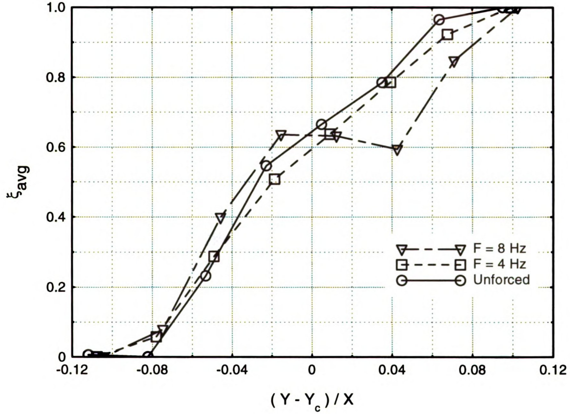

Figure 5.3.9. Normalized profiles of average concentration.

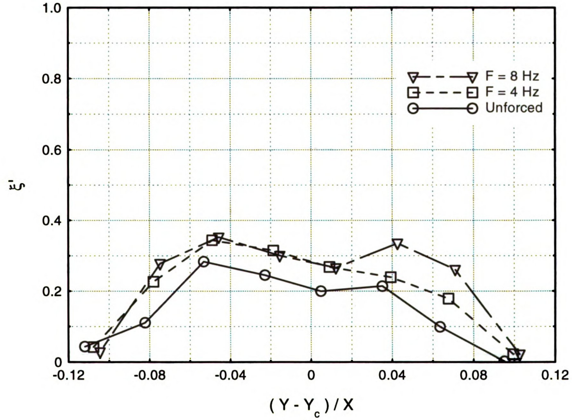

Figure 5.3.10. Normalized profiles of ξ_{rms}.

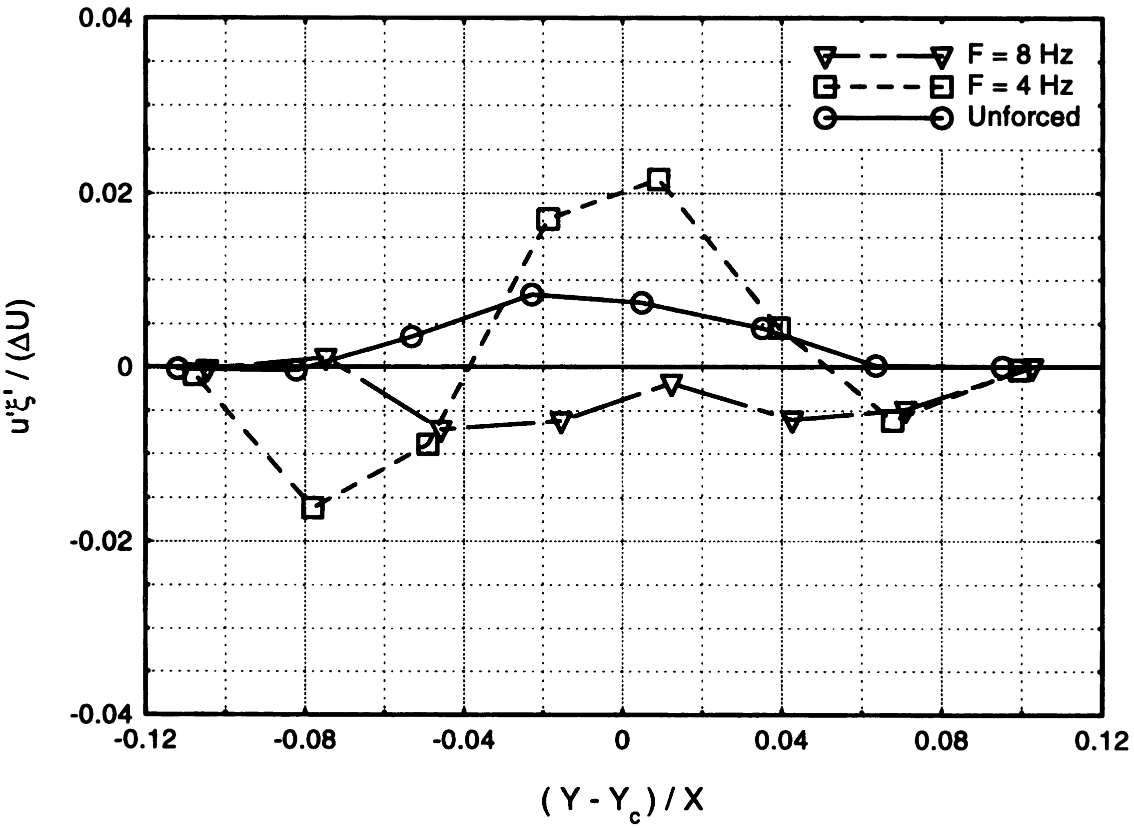

Figure 5.3.11. Normalized profiles of $\overline{u'\xi'}$.

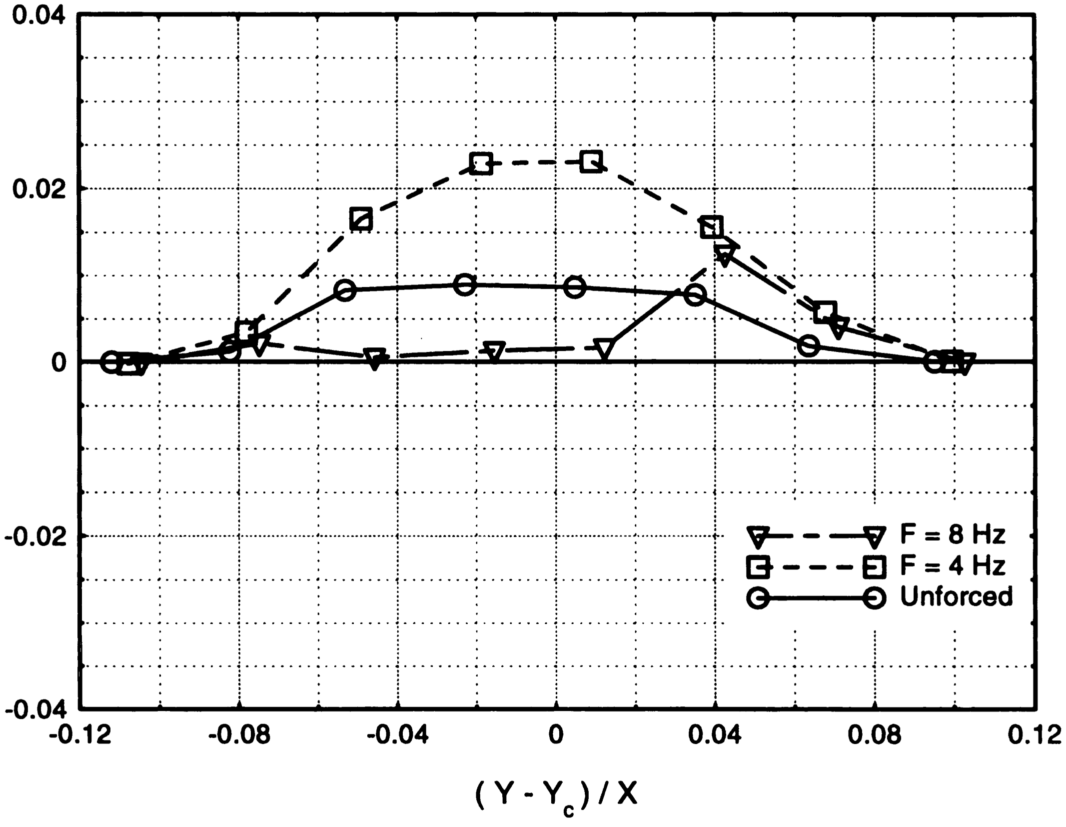

Figure 5.3.12. Normalized profiles of $\overline{v'\xi'}$.